

Conjugated Polymer Actuators for Articulating Neural Probes and Electrode Interfaces

by

Eugene Dariush Daneshvar

A dissertation submitted in partial fulfillment
of the requirements for the degree of
Doctor of Philosophy
(Biomedical Engineering)
in the University of Michigan

2014

Doctoral Committee

Professor Ronald Larson, Co-Chair
Professor Elisabeth Smela, University of Maryland, Co-Chair
Assistant Professor Mohamed El Sayed
Assistant Professor Parag Patil
Professor Michael Thouless

© Eugene Dariush Daneshvar 2014

Dedication

For my family: Past, Present, and Future

For kids wondering why they are different.

Acknowledgements

My father Dr. Yousef Daneshvar has and always will be my number one role model as an gentleman; an honest and decent human being. He has taught me the priceless value of character; the difference between being wealthy and rich. His pristine ethics and morals have inspired my own. Cardiologist by day and Biomedical Engineer by night, he has shown me what it means to be passionate about your work and not let anything stop you from moving forward.

My mother Mahin Daneshvar taught me what love means. Love is dedicated, selfless, and genuine. These are essential attributes to have while completing doctoral research. I am also thankful for her dedication in always getting me to school on time, as well as for slipping some cash in my pocket so I could enjoy a treat at lunch time. She always believed in me and knew I'd achieve my goals eventually, even if I needed a longer runway.

Professor Elisabeth Smela is the epitome of a scientist and mentor. Her dedication to academic integrity and command of the English language are aspirations I can only attempt to mimic. She is solely responsible for the accuracy and professional quality of the work presented here. I was a student that wasn't in her lab or even at her University; however, she gave me just as much time (if not more) to develop my skills as if I were one of her students. Whenever I asked how I could compensate, she simply said to "pay it forward."

Professor Ronald Larson is a selfless and compassionate catalyst. In the midst of chaos and without knowing me personally, he took on the responsibility to chair my committee

and enable the completion of my dissertation. Not similarly, Professor Khalil Najafi witnessed the most uncomfortable set of facts related to my graduate experience, and yet he took on the enormous responsibility to shelter and stabilize me. He is another example of the epitome of a selfless mentor. There could be no greater example of disparity as between his humbleness and faculties.

My introduction to the field of Neural Engineering was through Professor Dave Anderson. His genuine passion for the field was inspirational and compelled me to pursue research with his student, Daryl Kipke. Daryl's excitement was contagious and motivated me to break boundaries and pursue my novel ideas. Apparently, I had the same effect on him.

Dr. Parag Patil always asked me the most relevant and yet somehow unobvious questions. Despite the relentless demand for his attention, he always found time for meeting me. Professor Mohamed El-Sayed helped ground me and keep me focused on the essentials needed to be done. He also became a friend. Professor Michael Thouless had an amazing capacity to immediately understand the context and relevance of my work or challenge. His offer to help overcome administrative issues was brave and sincerely appreciated.

Mohammad Reza Abidian introduced me to the field of conjugated polymers. Aside from being my close mentor, he was always a dear friend when I need one. John Seymour, Dave Pellinen, and Razi Haque shared valuable microfabrication experience that enabled me to build what I wanted. Tim Faley was tremendous help in showing me

the big picture and guiding me to discover where I fit in. Aileen Huang-Saad lent me her reputation and introduced me to the subtleties of entrepreneurship.

My sister Catherine taught me the value of leading a balanced life. My brother Kambiz taught me to be kind and trust others, but always be prepared for a surprise. My brother Gerald (Farrokh) taught me how to use the “chip on my shoulder” to propel me forward. His belief in my capabilities was almost irrational and yet it inspired me to test and demonstrate them. My sister Caroline taught me how to follow through with goals, even if you’re the only one that believes in them. My sister Katy never stopped believing in me. She was my chief supporter and motivator and helped me define happiness correctly. My cat Buzzoon was a tremendous emotional support when I needed it (Bina too).

There are too many members of my extended family to name; however, our monthly “sandwich” parties were a great source of support and love that I hope always continue. The Raoof family (Amoo Ameer, Khala Samar, Saja, Khalid, Sarah, Harith, Omer, Ali, Wafia, and Simsim) accepted me as one of their own. Many wonderful memories are lovingly kept.

The contribution of supportive friends couldn’t be understated. Mahdi Sadeghi, Hasan Sidiqi, Farhan Haq, Mohammad Reza Abidian, Ali Besharatian, Razi Haque, Mike McKervey, James Godre, Aria Moazzen, Alireza T., Ed Tang, John Janik, Sarah H, Sumbal, Mina, Niosha, Niloufar, Wasim & Alisa, Mir & Huma, IGSA community, MSGA community, Leaf’s Hockey team. Last but not least the “Axis of EECS”: Hashem Alwazzan, Khalid Arabo, Steven Koski, Ian Kountains, Erik Shomburg, and Kristen Tebo.

My lab members each played a role in influencing my research career. Neural Engineering Lab: Kip Ludwig, Jey Subbaroyan, Matt Gibson, Nick Langhals, HIRAK Parikh, Erin Purcell, Matt Johnson, Greg Gage, Tim Marzullo, “TK” Yoshida, Pratik Rohatgi, Taegyun Moon, Dave Turer, Mike Joseph, Azadeh Yazdan, Rachel Miriani, Colin, Paras, Dave Pellinen, Payam Lahiji, Suraj. Smela Lab: Bavani Balakrishnan, Mark Kujawski, Deepa Sritharan, and Jason West. Najafi Lab: Becky Peterson, Robert Gordecker, Behrouz Shiari, and Trasa Berkhardt.

The officemates in 2001 EECS helped creating a positive working atmosphere. The LNF Staff were always helpful in training me on equipment. The BME administrative staff were huge catalysts. Special thanks to Vera Williams, Tonya Brown, Maria Steele, Chuck Nichols, Jane Mackie, and Matt O’Donnell. A special thanks to Professor Alec Gallimore, Darlene Ray Johnson, and Dean David Munson in performing miracles.

Last but not least, I need to acknowledge my best friend, Duna. She is a rare jewel. Graduate school is a unique experience that can make you one dimensional. Duna helped remind me that pragmatism is just as important as idealism. She affectionately would admit that I always ended up being right, but that it was also always my fault. When I was with her my glass was over pouring.

Table of Contents

Dedication.....	ii
Acknowledgements.....	iii
List of Tables.....	xi
List of Figures.....	xii
List of Appendices.....	xix
Abstract.....	xx
CHAPTER 1 Motivation and Introduction.....	1
1.1 Outline.....	1
1.2 Background.....	2
1.2.1 Motivation: Micro-actuation in neural interface devices.....	2
1.2.2 Conjugated polymer actuators.....	9
1.2.3 Actuation performance measurands.....	16
1.2.4 Actuation performance testing methods.....	19
1.2.5 Residual stress in bilayer actuators.....	23
1.2.6 Macro vs. Micro-scale measurements.....	26
1.3 Research objectives.....	28
1.4 Summary of contributions.....	28
1.5 References.....	30
CHAPTER 2 Characterization of conjugated polymer actuation under cerebral physiological conditions.....	40
Abstract.....	40
2.1 Introduction.....	41
2.1.1 Conjugated polymer actuators.....	44
2.1.2 Actuation in cerebral physiological ion concentrations and temperature.....	47
2.2 Methods.....	48
2.2.1 Bilayer beam actuator fabrication.....	48
2.2.2 Actuator cycling.....	49
2.2.3 Beam tip deflection, curvature, and actuation strain.....	49
2.2.4 Electrochemical break-in.....	51
2.2.5 Scanning electron microscopy and elemental analysis.....	52

2.3 Results and Discussion.....	52
2.3.1 Deflection during cyclic voltammetry in NaDBS at room temperature.....	52
2.3.2 Cyclic voltammograms under four conditions	54
2.3.3 Actuation strains during CVs	57
2.3.4 Maximum deflection during CVs.....	60
2.3.5 Elemental analysis	62
2.4 Conclusions.....	65
2.5 Acknowledgments.....	66
2.6 Supporting Information.....	66
2.6.1 Variation among samples	67
2.6.2 Deflection of all twelve bilayers under all four conditions	68
2.6.3 Cyclic voltammetry of bilayers under the four conditions.....	70
2.6.4 Deflection upon voltage stepping.....	77
2.6.5 Transient effects upon voltage stepping.....	79
2.6.6 Ramping voltage to attenuate initial transient effects	82
2.6.7 Calculation of curvature and actuation strain from deflection measurements .	84
2.6.8 Calculation of effective substrate modulus	85
2.6.9 Cross-sectional images of devices showing delamination	89
2.7 References	90
 CHAPTER 3 MEMS device for measuring conjugated polymer actuator force and residual stress in bilayers	 97
Abstract	97
3.1 Introduction	98
3.2 Mechanical theory.....	99
3.2.1 Combination of forces and moments.....	99
3.2.2 Effective substrate Young's moduli	101
3.2.3 Composite beam stiffness.....	103
3.2.4 Solving for ϵ_{act}	104
3.2.5 Design parameters	104
3.2.6 Residual stress	109
3.3 Materials and Methods.....	111
3.3.1 Fabrication	111
3.3.2 Experimental setup.....	115

3.4 Results	116
3.4.1 Residual stress is sufficient to bend beams and lift weights.....	116
3.4.2 Cycling in NaDBS and aCSF	118
3.4.3 Calculation of PPy actuation strain	120
3.4.4 Calculation of residual stress	121
3.5 Conclusions	121
3.6 Supplemental Information.....	122
3.6.1 Novel method to measure conjugated polymer Young's modulus and actuation strain	122
3.6.2 Excluded devices	124
3.6.3 Stiffness ratios from referenced bilayer papers	126
3.7 References	127
CHAPTER 4 Navigating conjugated polymer actuated neural probes in a brain phantom	130
Abstract	130
4.1 Introduction	131
4.2 Methods.....	134
4.2.1 Stiffness to overcome insertion force	134
4.2.2 Device design and fabrication	135
4.2.3 Actuator polymerization	137
4.2.4 Insertion and actuation method.....	137
4.3 Results	139
4.3.1 Acceptable designs to prevent buckling	139
4.3.2 Images of fabricated devices	140
4.3.3 Electrode site impedances	141
4.3.4 Articulated projections	142
4.3.5 Insertion and actuation into brain phantom	143
4.4 Discussion and conclusions.....	145
4.5 References	148
CHAPTER 5 Conclusions, contributions, and future directions	151
5.1 Conclusions	151
5.2 List of contributions	151

5.2.1 Characterization of PPy(DBS) actuation performance under cerebral physiological conditions	151
5.2.2 Development of a MEMS tip-weighted conjugated polymer bilayer actuator test device	152
5.2.3 Proof of concept of functional articulating neural probes and electrodes demonstrated.....	153
5.2.4 Journal papers	153
5.2.5 Conference papers	154
5.2.6 Oral presentations	154
5.2.7 Conference posters	155
5.3 Future directions.....	156
5.3.1 Further characterization of actuation performance.....	156
5.3.2 Alternate device designs for measuring actuation performance.....	156
5.3.3 Application specific design of movable neural interfaces.....	159
5.3.4 Projections with variable thickness and segmented joints.....	159
5.3.5 Alternate projection geometries.....	160
5.3.6 Other uses of movable projections	161
5.4 Final thoughts.....	162
5.5 References	163
Appendices.....	164
A1. Hybrid Conducting Polymer–Hydrogel Conduits for Axonal Growth and Neural Tissue Engineering.....	164
A2. Lab notebook excerpts recording the movable probe and electrode concepts	165

List of Tables

Table 1-1. Ionic components of artificial cerebrospinal fluid [81].	15
Table 2-1. Ionic components of artificial cerebrospinal fluid [48].	47
Table 2-2. Values of average actuation strain α , exchanged charge density, and strain-to-charge density in the 9 th scan in NaDBS (12 samples) and average ratios of the 19 th to the 9 th scans under different cycling conditions (n = 3 unless otherwise noted).	56
Table 3-1. Average deflections from three scans of a set of devices and weight mass with (*) indicating bending greater than 90° and (-) indicating no bending observed. Mass force was corrected for buoyancy.	119
Table 3-2. Summary of device dimensions and calculated values	120
Table 3-3. Beam deflections with (*) indicating bending greater than 90° and (-) indicating no bending observed, and calculation of σ_{PPy} .	121
Table 4-1. Projection tip aspect ratios	146
Sup. Table 2-1. Peak to peak deflections for the samples in Figure 2-5 of the main text.	69
Sup. Table 2-2. Average actuation strain α , exchanged charge density, and strain-to-charge density (during reduction and oxidation and their sum) in the 9 th and 19 th scans under different cycling conditions, as well as the ratios of the 19 th and 9 th scan (n = 3).	88
Sup. Table 3-1 PPy oxidized Young's modulus and actuation strain calculated from sample combinations cycled in NaDBS at RT.	123
Sup. Table 3-2 Excluded devices having variable width	124
Sup. Table 3-3 Excluded devices having variable length	125
Sup. Table 3-4. Values used to determine stiffness ratios in referenced bilayer papers.	126

List of Figures

Figure 1-1. Examples of microelectrodes used for neural recordings. a) hand-assembled microwires (image source sfn.org), b) microfabricated 2D “Michigan” style probes, and c) microfabricated 3D “Utah Arrays” inserted into brain tissue.	3
Figure 1-2. The longevity of the quality of neural recordings sensed by cortical neural electrodes is thought to be related to the tissue response to the electrode. a) Insertion of the probe disrupts the tissue [7]. b) The insertion trauma activates an immune response, which changes the cell types at the probe interface [9]. c) Cross-sectional images showing the chronic response to tissue with a device inserted and removed (top), and encapsulation of the device by non-neuronal cells (bottom) [9]. d) Electrical “shadowing” may occur across the “Michigan” style probe, reducing the quality of recording from electrode sites along its length [10].	4
Figure 1-3. a) Clinical data for stimulation threshold vs. tissue-electrode distance for a) retinal electrodes [18] and b) cochlear electrodes [19].	5
Figure 1-4. (a) Electrothermal based moveable probe [23]; (b) Motorized microdrive for moving neural probes [6]; (c) Fabricated parylene balloon actuator [24].	7
Figure 1-5. Spring-loaded electrode projections being developed [25].	8
Figure 1-6. Structures of some conjugated polymers in their neutral states: (a) polyacetylene, (b) polypyrrole (PPy), (c) polyaniline, and (d) poly(3,4-ethylenedioxythiophene) (PEDOT). The conjugation path is indicated in blue. (Image from [35]).	9
Figure 1-7. Typical current vs. voltage profile from a cyclic voltammetry cycle for PPy(DBS) cycled in 0.1 M NaDBS. Current peaks are associated with ion ingress and egress from the polymer matrix.	11
Figure 1-8. EDX spectra of a PPy(DBS) sample cycled in NaDBS at 22 °C.	16
Figure 1-9. (Left) Diagram identifying the relationship of CP intrinsic properties and actuation performance. (Right) Diagram indicating that the electrical, chemical, and mechanical properties are inextricably linked.	17
Figure 1-10. Two methods used for testing free films. (Left) Tensile test machine (Shimadzu), (Right) Aurora Scientific Inc. Dual Lever Arm system. Images from [104].	20
Figure 1-11. Graphics to help compare the loading of free films and bending actuators: (Left) axially-loaded free film by a dead weight, (Middle) axially-loaded free film against a spring, (Right) bilayer actuator bending a substrate.	22
Figure 1-12. Relative thickness ratios of bilayer actuators used in prior work: a) $r = 121$ [86], b) $r = 213$ [111], c) $r = 4,170$ & d) $112,597$ [55].	23

Figure 1-13. (Top) Identifying the stages of CP polymerization and conditioning. (Bottom) Graphic distinguishing deflection δ due to static residual stress and active actuation strain. 24

Figure 1-14. Work-per-cycle modeled as a function of stiffness ratio between the substrate and conjugated polymer, with Young's moduli as Y in the active state and Y' at rest. The curve for $Y >$ the case with the highest peak is for the cation-exchanging polymers (figure from [100]). 26

Figure 1-15. (Left) Experimental setup with glass weights used for actuation force measurement by [113]. (Right) Image of the tungsten needle being positioned on the beam tip (unpublished – courtesy of copyright holder E. Smela). 27

Figure 2-1. a) An array of 5 probe devices in air having lengths of 1 mm and widths between 50 μm and 250 μm , deflected out of plane with uniform curvature after fabrication, with no applied voltage. b) A similar set of probes with lengths of 800 μm actuated during penetration into a gel brain tissue phantom. The Parylene probe beams included an insulated electrode trace with an exposed Au electrode site at the tip and an overlying PPy/Au actuator. c) A segmented beam with actuators at three joints, electrochemically reduced to be straight (top) and oxidized to be bent (bottom) in NaDBS solution. 43

Figure 2-2. Three superimposed images of beam deflection upon reduction, oxidation, and transitioning midway (overhead view with the face of the beam perpendicular to the page). The ruler scale is in cm. The center position illustrates the zero curvature reference point that was used to determine tip deflections, and the arrows drawn over the image indicate the magnitude of the tip deflection. 50

Figure 2-3. Deflection vs. time (lower red curve) during the first 6 cycles (numbered) of a bilayer in NaDBS at room temperature. The voltage was scanned at 10 mV/sec between +0.4 and -1.0 V vs Ag/AgCl, as illustrated at the top (black curve). Positive deflection indicates PPy expansion (bending PPy-side out), and negative deflection indicates PPy contraction (PPy-side in). 53

Figure 2-4. Current (black line) and displacement (thicker red line) as a function of potential during the 19th CV scan at 10 mV/s under four conditions. The direction of the scan for the displacement curves is indicated by arrows; note that this axis has been reversed to facilitate comparison with the current. The deflection axis is shifted in (b) and (d) relative to (a) and (c), but has the same amplitude (16 mm). The dashed lines in (c) show results from a second sample. 55

Figure 2-5. a) Maximum deflection of representative bilayers during oxidation and reduction during cyclic voltammetry as a function of cycle number. Black symbols: actuation in NaDBS at room temperature (all samples during cycles 1-10). Filled symbols: actuation in aCSF during cycles 11-20; open symbols: actuation in NaDBS; red triangle symbols, actuation at 37 °C during cycles 11-20; blue circle symbols, actuation at room temperature. 61

Figure 2-6. EDX spectra of samples cycled in NaDBS at 22 °C and in aCSF at 37 °C, normalized to the S peak.....	62
Figure 3-1. (Left) Perspective view of a single weighted bilayer beam. (Right) Diagram showing the counteracting moment and force due to the actuation strain and the weight.	98
Figure 3-2. Stress distribution in the substrate (a) after polymerization but before priming, (b) after priming, (c) stress due to the weight.	99
Figure 3-3. Beam cross-sections showing the effective layers (Left) and the layers considered as the composite vs. substrate (Right).	100
Figure 3-4. Beam cross-sections illustrating the transformed section method for a 2-layer beam. (Figure credit E. Smela.)	101
Figure 3-5. Bilayer curvature modeled as a function of E_{sub} (2 MPa – 160 GPa) with $h_{PPy} = 21 \mu\text{m}$. The arrows indicate the approximate Young's moduli for three types of materials used in neural interfaces. (Code provided by E. Smela, written by A. Nacev)	106
Figure 3-6. Bilayer curvature modeled as a function of h_{PPy} , assuming Parylene as the substrate. The maximum curvature was at $h_{PPy} = 27.3 \mu\text{m}$, resulting in $h_{PPy}/h_{sub} = \sim 1.3$. (Code provided by E. Smela written by A. Nacev)	107
Figure 3-7. Positive bilayer tip deflection modeled as a function of h_{PPy} (1 - 100 μm), with beam length = 10 mm, beam width = 1000 μm , and varied opposing point force at the tip = 0, 10, 100, 1000 μN . Devices are assumed to be supported on a substrate, therefore, deflection less than 0 mm is excluded.....	108
Figure 3-8. Positive bilayer tip deflection modeled as a function of h_{PPy} (1 - 100 μm) and beam length = 10 mm, beam widths 200 - 1000 μm , with opposing 50 μN point force at the tip.	109
Figure 3-9. Fabrication process overview.....	111
Figure 3-10. Electroplating waveform used in electroplating the nickel weights.	113
Figure 3-11. (Left) Fabricated weighted bilayer device with thickness of 21 μm Parylene, 100/1000 Å Cr/Au, lengths of 10 mm, and widths of 1000, 800, 600, 400, and 200 μm . (Right) Device from the left polymerized with PPy(DBS).....	115
Figure 3-12. Image of a device in air (PPy was fully dried) with full curvature that was excluded.....	116
Figure 3-13. Images of weighted bilayer beams after the initial actuation cycle residual stress builds up. a) Horizontal view showing the devices laying flat when reduced (-1.0	

V). b) Horizontal, c) top, and d) side views of the devices lifting when oxidized (0 V).
 117

Figure 3-14. Actuated devices in NaDBS at 22 °C (a,c,e) and in aCSF at 37 °C (b,d,f).
 (Top) overhead view; (Middle) inline side view; (Bottom) parallel side view. 118

Figure 3-15. Model prediction (lines) of bilayer actuation force as a function of thickness ratio m for $\alpha_{PPy} = 0.03$, $h_{sub} = 21 \mu\text{m}$, $n = 0.14$, $L = 10 \text{ mm}$, and $w = 200, 400, 600, 800,$ and $1000 \mu\text{m}$. Actuation forces calculated from the data in Table 3-1 (blue points, NaDBS, red points, aCSF). Experimental uncertainty in the thickness was $5 \mu\text{m}$, shown by the error bar. 119

Figure 4-1. Side view of (a) a standard neural probe and (b) a neural probe with an electrode projection. Damaged tissue surrounds the larger probe in both designs, but smaller projections are expected to cause less damage [3, 9]. 133

Figure 4-2. Overview of the fabrication of electrode projections on the probe. (a) Electrode sites and traces patterned with mask 1, (b) actuator areas and traces defined by mask 2, (c) etch-stop pattern for the projections using mask 3, and (d) device shape defined by mask 4. (e) PPy was polymerized post release. For clarity, only one of the five projections is shown. 137

Figure 4-3. Electrodes were clamped to the end of the microdrive. The clip also acted as an electrical connection to the actuators. Artificial cerebrospinal fluid was used as the electrolyte to actuate the projections to lie flat prior to insertion. 139

Figure 4-4. Calculated tip deflection and force vs. device length (for $20 \mu\text{m}$ thick PPy(DBS), $20 \mu\text{m}$ parylene). Force decreases with projection length, while deflection increases. Dotted red line: force required to insert the probe, which increases with insertion depth. Dotted blue line: $50 \mu\text{m}$ deflection needed to exit the encapsulation zone. Acceptable designs require both enough force and enough deflection. 140

Figure 4-5. Images of devices with varying lengths (200-1000 μm) and widths (50-250 μm) prior to polymerization of PPy(DBS). Image (f) is zoomed in on a single projection in between two fixed electrode sites. 141

Figure 4-6. Impedance values of electrode sites as shown in a Bode magnitude plot (left), Nyquist plot (center), and Bode phase angle plot (right). Impedances of electrode sites fixed to the substrate and on the projections have similar values. 142

Figure 4-7. (a-b) Still images of devices in aCSF of an array of electrode projections of varying widths with sites (a) in plane, (b) actuated out of plane, showing light reflection off of the articulated electrode site. (c) Electrode projections removed from solution and deflected out of plane with no voltage applied. 143

Figure 4-8. Screenshots of devices with five electrode projections of varying widths (50, 100, 150, 200, and 250 μm) and lengths (top row 1000 μm , bottom row 800 μm) penetrating a brain tissue phantom made of 0.6% agarose and 0.1 M NaDBS. Images in

the top row show devices (a) outside the phantom, (b) inserted in a reduced state (straight), and (c) inserted in an oxidized state (bent). Images in the bottom row show actuation during insertion (d-f). The estimated (compensated for viewing angle) tip deflections out of plane for the 800 μm long beams with widths of 50 μm and 100 μm were $\sim 772 \mu\text{m}$ and $\sim 474 \mu\text{m}$, respectively. 145

Figure 4-9. Electrode grid proof of concept shown as an array of uncoated electrode projections..... 147

Figure 5-1. (Left) Fabricated bilayer beam with embedded strain sensor and Wheatstone bridge. (Middle) Beam prior to displacement. (Right) Beam after manual displacement by a needle and computer-controlled linear actuator..... 157

Figure 5-2. Change in resistance vs time from manually displacing bilayer beam with integrated thin film metal strain sensor..... 157

Figure 5-3. Top view of the composite beam either as a control (Left), with a wider substrate (Middle), or tethered to a bridge acting as a mechanical spring (Right). 158

Figure 5-4. (Left) Comsol rendering of a bilayer beam with a wider substrate. (Right) Comsol rendering showing T-Bridge tip displacement vs actuation strain for a bridge length of 5000 μm 158

Figure 5-5. Variable segmented devices: (a-b,-c-d) effect of differing thickness ratios for the joints and (e) a device with variable number of segmented joints along the projection. 160

Figure 5-6. Alternate projection geometries: (Left) tip shape, (Right) projection shape. 160

Figure 5-7. Proof of concept for the grid array applications as well as the electronic velcro idea. Array of 5x6 projections 100 μm wide, 200 μm long, PPy(DBS) $\sim 20 \mu\text{m}$, Parylene $\sim 10 \mu\text{m}$ for the projections, and $\sim 35 \mu\text{m}$ for the substrate..... 161

Sup. Figure 2-1. Maximum deflection during oxidation and reduction in NaDBS at 22 $^{\circ}\text{C}$ as a function of cycle number. a) Six bilayers on which the PPy(DBS) was polymerized separately (one bilayer at a time). b) Six bilayers on which the PPy(DBS) was polymerized simultaneously. 67

Sup. Figure 2-2. The maximum deflections during cyclic voltammetry of all twelve samples, cycled in NaDBS at 22 $^{\circ}\text{C}$ for the first 10 cycles, then in the medium and at the temperature indicated. (For correlation with Sup. Figure 2-3-Sup. Figure 2-6, circles = sample 1, up-pointing triangles = sample 2, and down-pointing triangles = sample 3.).. 70

Sup. Figure 2-3. Cyclic voltammograms of three samples cycled in NaDBS at 22 $^{\circ}\text{C}$ for (left) the first 10 scans and then (right) the second 10 scans. To facilitate comparison,

since the scales on the left and the right differ, scan 10 is repeated. Sample 3 was used in the main text..... 72

Sup. Figure 2-4. Cyclic voltammograms of three samples cycled in NaDBS at (left) 22 °C for the first 10 scans and then (right) at 37 °C for the second 10 scans. Sample 2 was used in the main text. 73

Sup. Figure 2-5. Cyclic voltammograms of three samples cycled (left) in NaDBS at 22 °C for the first 10 scans and then (right) in aCSF at 22 °C for the second 10 scans. Sample 3 was used in the main text. 74

Sup. Figure 2-6. Cyclic voltammograms of three samples cycled (left) in NaDBS at 22 °C for the first 10 scans and then (right) in aCSF at 37 °C for the second 10 scans. Note that the vertical scale for (b) is almost twice that for (d) and (f). Sample 2 was used in the main text..... 75

Sup. Figure 2-7. Typical cyclic voltammograms in the four solutions..... 77

Sup. Figure 2-8. Preliminary data for 3 samples (one per group). Deflection during the 10th step between 0.4 V and -1.0 V either in NaDBS at RT or in aCSF at 37 °C after prior electrochemical cycling in one of these two solutions at RT. NaDBS-NaDBS indicates priming in NaDBS followed by stepping in NaDBS..... 78

Sup. Figure 2-9. Preliminary data for 3 samples. Step responses of ten consecutive oxidation and reduction cycles, overlaid, in either NaDBS at RT or aCSF at 37 °C. Samples “NaDBS-aCSF” and “aCSF-aCSF” were stepped in 37 °C aCSF after priming in NaDBS at RT or aCSF at RT, respectively..... 80

Sup. Figure 2-10. Preliminary data for 3 samples. Transient deflection peaks during reduction for scans 2-10 relative to scan 1 for the sample primed in NaDBS at RT and cycled in aCSF at 37 °C (NaDBS-aCSF, Sup. Figure 2-9c). Deflection overshoot is the difference of each scan relative to the steady state value of scan 1 (at 100 s). The peak deflection overshoots for scans 2-10 are plotted in the inset..... 81

Sup. Figure 2-11. Deflection as a function of time in response to the voltage profiles shown at the top: samples were held at +0.4 V (oxidized) for 100 seconds, ramped to -1.0 V (reduced) at varying scan rates (5, 50, and 500 mV/s), and then held at -1.0 V for 240 seconds. Priming and ramping electrolytes were either NaDBS at RT or aCSF at 37 °C. 83

Sup. Figure 2-12. Trigonometry of beam bending used to obtain curvature. 84

Sup. Figure 2-13. Beam cross-sections illustrating the transformed section method for a 2-layer beam..... 85

Sup. Figure 2-14. SEM images of bilayer cross sections of devices after being cut mid-length with some samples showing (a) no delamination and (b) delamination of the PPy layer. The delamination may have occurred during actuation or due to cutting..... 89

Sup. Figure 3-1 Excluded devices with variable widths (a ₁ -a ₃) NG1 D1-5, (b ₁ -b ₃) NG3 D1-5, (c ₁ -c ₃) NG3 D6-10.....	124
Sup. Figure 3-2 Excluded devices with variable lengths (a ₁ -a ₃) NG2 C1-5, (b ₁ -b ₃) NG2 C6-10, (c ₁ -c ₃) NG3 C1-5.....	125

List of Appendices

A1. Hybrid Conducting Polymer–Hydrogel Conduits for Axonal Growth and Neural Tissue Engineering.....	164
A2. Lab notebook excerpts recording the movable probe and electrode concepts.....	165

Abstract

This thesis investigated the potential use of polypyrrole (PPy) doped with dodecylbenzenesulfonate (DBS) to controllably articulate (bend or guide) flexible neural probes and electrodes. PPy(DBS) actuation performance was characterized in the ionic mixture and temperature found in the brain. Nearly all the ions in aCSF were exchanged into the PPy – the cations Na^+ , K^+ , Mg^{2+} , Ca^{2+} , as well as the anion PO_4^{3-} ; Cl^- was not present. Nevertheless, deflections in aCSF were comparable to those in NaDBS and they were monotonic with oxidation level: strain increased upon reduction, with no reversal of motion despite the mixture of ionic charges and valences being exchanged. Actuation depended on temperature. Upon warming, the cyclic voltammograms showed additional peaks and an increase of 70% in the consumed charge. Actuation strain was monotonic under these conditions, demonstrating that conducting polymer actuators can indeed be used for neural interface and neural probe applications.

In addition, a novel microelectro-mechanical system (MEMS) was developed to measure previously disregarded residual stress in a bilayer actuator. Residual stresses are a major concern for MEMS devices as that they can dramatically influence their yield and functionality. This device introduced a new technique to measure micro-scaled actuation forces that may be useful for characterization of other MEMS actuators.

Finally, a functional movable parylene-based neural electrode prototype was developed. Employing PPy(DBS) actuators, electrode projections were successfully controlled to either remain flat or actuate out-of-plane and into a brain phantom during insertion. An electrode projection 800 μm long and 50 μm wide was able to deflect almost 800 μm

away from the probe substrate. Applications that do not require insertion into tissue may also benefit from the electrode projections described here.

Implantable neural interface devices are a critical component to a broad class of emerging neuroprosthetic and neurostimulation systems aimed to restore functionality, or abate symptoms related to physical impairments, loss of sensory abilities, and neurological disorders. The therapeutic outcome and performance of these systems hinge to a large degree on the proximity, size, and placement of the device or interface with respect to the targeted neurons or tissue.

CHAPTER 1 Motivation and Introduction

1.1 Outline

Chapter 1 introduces the motivation of micro-actuation of neural interfaces and relevant background information on conjugated polymer actuators. The significance of identifying residual stress in bilayer actuators and its relevance to potential applications is discussed. Actuation performance testing methods are reviewed. Lastly, difficulty with prior work on micro-scale measurements is discussed.

Chapter 2 discusses how conjugated polymer actuator performance depends not only on the synthesis medium, but also on the medium in which it is employed. The behavior of bilayer actuators is characterized by studying the actuation of PPy(DBS) at body temperature (37 °C) in artificial cerebrospinal fluid (aCSF), which contains a mixture of ions. Results show that under physiological conditions, the performance is substantially the same, demonstrating that these actuators may be used at elevated temperatures and in mixed ionic aqueous environments such as cerebrospinal fluid.

Chapter 3 discusses the importance of distinguishing residual stress from actuation strain in bilayer actuators, as well as the need to need for a device to measure actuation forces on the micro-scale. A MEMS weighted bilayer actuator and model was introduced and developed to measure residual stress due to priming bilayer actuators and quantify actuation force. The results demonstrate that this new technique is useful for studying electroactive polymer properties and actuation performance for bilayer actuators.

Chapter 4 introduces the concept of adjusting the position of electrode sites on neural interfaces, which may be beneficial for several reasons. In this work, the capability of conjugated polymer PPy(DBS) to controllably actuate neural electrode projections out-of-plane was investigated. Functional articulating neural electrode prototypes were designed, fabricated, and tested. The electrode projections were successfully controlled to either remain flat or to actuate out-of-plane.

Chapter 5 states the conclusions, thesis contributions, future work, and concluding remarks.

1.2 Background

1.2.1 Motivation: Micro-actuation in neural interface devices

The application motivating the work presented here is to augment implantable neural interface devices with controllable articulating elements. Examples of neural interface devices include cortical neural electrodes implanted in or on the brain for brain-machine interfaces [1], deep brain recording and stimulation devices for treatment of neurological disorders, retinal electrodes for restoring a perception of sight [2], cochlear electrodes for restoring hearing [3], spinal electrodes [4], and a variety of peripheral electrodes for interfacing with the nervous system [5]. Modulating the position of electrode sites within neural tissue to change electrode proximity to particular neurons may be beneficial for different reasons.

For neural recording devices, the longevity and stability of sensing neural activity is highly variable on the size and proximity of the electrode to the neurons of interest [6].

Three main technologies at the current forefront of cortical neural electrodes for

recording are shown in Figure 1-1. The microwire in Figure 1-1a is manually assembled and is essentially an insulated conductor that is exposed at the tip. Microfabrication is used for creating the planar “Michigan” style probes as shown in Figure 1-1b and 3D “Utah Array” style in Figure 1-1c.

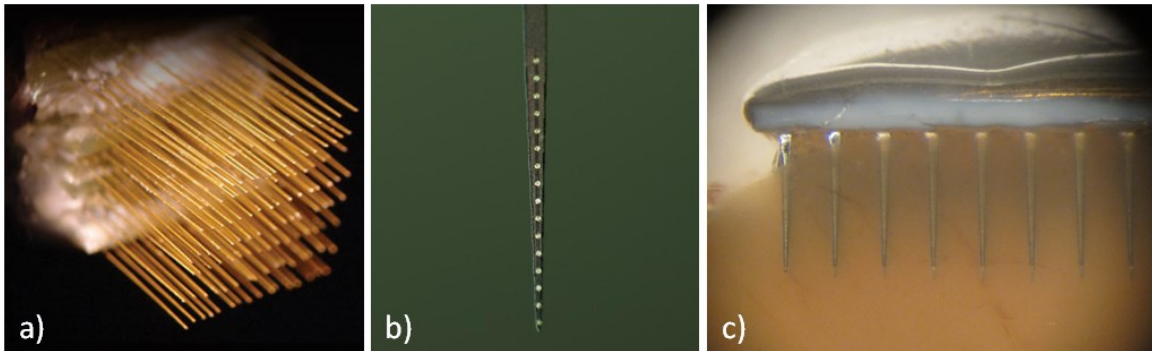


Figure 1-1. Examples of microelectrodes used for neural recordings. a) hand-assembled microwires (image source sfm.org), b) microfabricated 2D “Michigan” style probes, and c) microfabricated 3D “Utah Arrays” inserted into brain tissue.

Microelectrodes are designed to sense the physiology and functional activity of neurons that are connected in a dense dendritic network. Insertion of a “Michigan” style electrode disrupts this network and causes mechanical stress to the tissue [7], as can be seen in Figure 1-2d. Once implanted, the brain tissue senses the cortical neural probe as a foreign object and evokes an immune response to break down or protect the surrounding tissue [8, 9]. This foreign body response results in a $\sim 50\text{-}100\ \mu\text{m}$ sheath of non-neuronal cells that surrounds the device (Figure 1-2b-c) and decreases the recording signal to noise ratio.

The microwire and “Utah Array” style devices have only one electrode site located at their end, while the “Michigan” style probe has multiple electrode sites along its length. This is an important distinction for two reasons. First, the location of the electrode site, with respect to the condition of the surrounding tissue (e.g. neuronal population and

dendritic network), may affect the quality and longevity of the recordings. Secondly, electrode sites at the tip of a probe are more exposed to intact tissue than the additional electrodes sites along the length of the “Michigan” style probe. Figure 1-2d shows a theoretical scenario where the neural probe substrate dissipates transmission of a neural action potential in the tissue. This is referred to as a “shadowing” effect [10].

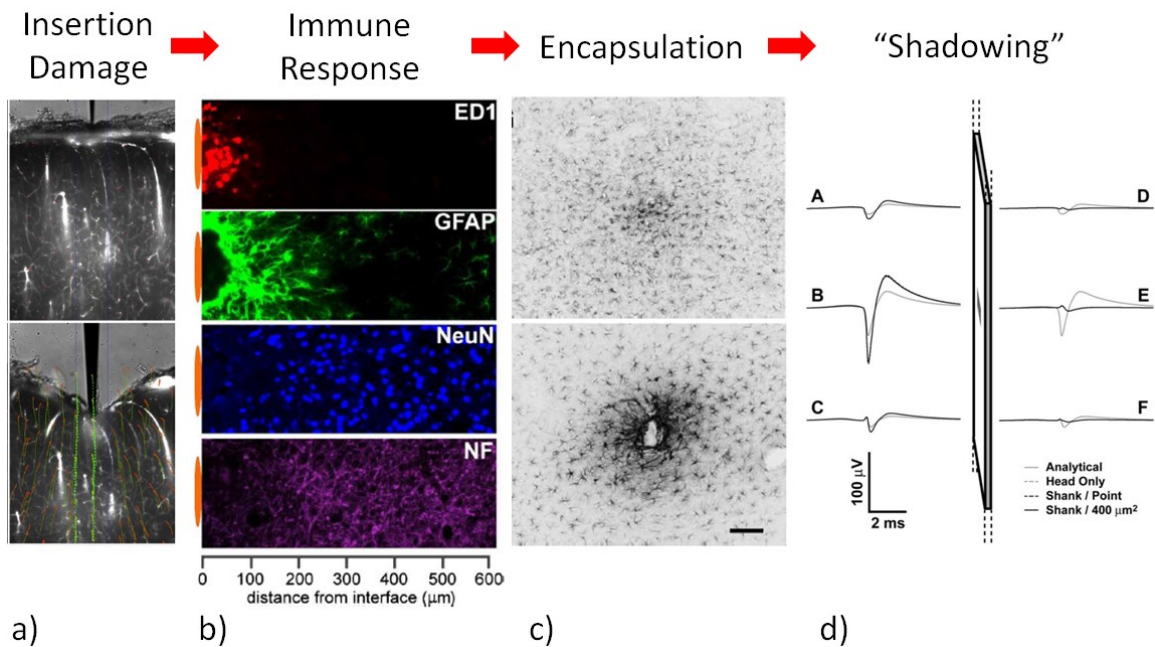


Figure 1-2. The longevity of the quality of neural recordings sensed by cortical neural electrodes is thought to be related to the tissue response to the electrode. a) Insertion of the probe disrupts the tissue [7]. b) The insertion trauma activates an immune response, which changes the cell types at the probe interface [9]. c) Cross-sectional images showing the chronic response to tissue with a device inserted and removed (top), and encapsulation of the device by non-neuronal cells (bottom) [9]. d) Electrical “shadowing” may occur across the “Michigan” style probe, reducing the quality of recording from electrode sites along its length [10].

Recently, the further miniaturization of the size of the probe has been shown to reduce the amount of tissue immune response and device encapsulation [11, 12]. The ability to place electrode sites outside of the expected damaged region (~50-100 μm) may result in increased recording signal to noise ratio and quality [13-15].

For neural stimulating devices, the selectivity and safe amount of charge injection required for therapeutic outcomes is directly related to all spatial and size factors [16]. More precise electrode placement may increase the treatment efficacy and lower the charge injection required for stimulation therapies [3, 17]. Two-dimensional electrode arrays are used for stimulation of retinal ganglion cells on the back of the eye to evoke perceptions of light. The efficacy of this therapy is limited due to gaps of 100-1000 μm that result from non-conformal attachment between the electrode array and the irregular conformation of the eye [18]. Figure 1-3a shows clinical data relating the stimulation threshold and tissue-electrode distance. Ideally this gap would be between 5-7 μm for optimum spatial density [17]. Similarly, cochlear electrode arrays are used for stimulating nerve bundles on the inner wall of the cochlea. However, the cochlea's spiral structure has variable and decreasing curvature, resulting tissue-electrode gaps of 600-1400 μm , where ideally gaps of 300 μm would provide sufficient spatial density [19]. Figure 1-3b shows clinical data comparing the current threshold for stimulation vs. the location of electrode sites with respect to the inner cochlea wall for two devices.

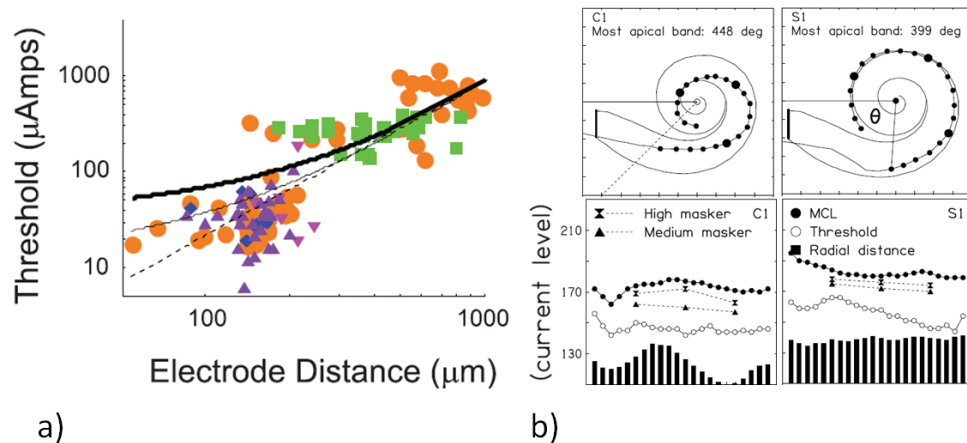


Figure 1-3. a) Clinical data for stimulation threshold vs. tissue-electrode distance for a) retinal electrodes [18] and b) cochlear electrodes [19].

Neurological disorders being investigated and treated with deep brain stimulation therapy are continually being explored. Targets for stimulation require sub-millimeter precision [20]. There is an increasing interest to steer or guide the insertion of electrode leads/probes, resulting in non-linear trajectories, to better target deep brain structures [21, 22].

MEMS technology is increasingly being used for miniaturization of implantable medical devices for diagnostic and therapeutic applications. Microfabricated systems of greater complexity have lower process yields and are at risk of increased modes of failure. Therefore, there is a constant effort to design robust devices, increase efficacy, and reduce power requirements, extending the usefulness and lifetime of the device.

Prior work on moveable neural devices

There have been several attempts to make movable probes, however, none have been proven successfully to meet all the requirements for safe, reliable, and effective long term chronic use to our knowledge. Muthuswamy et al. demonstrated the use of electrothermal and capacitive actuators for silicon probes fabricated and embedded in the brain cap to move neural probes vertically in vivo [23]. They recorded from their probes for 12 weeks with good signals. Cham et al., have also developed microwire probes that move vertically in the brain, by manually adjusting a screw on the head cap of the animal [6]. Pang et al. developed an electrolysis-based parylene balloon actuator in order to move neural probes [24]. The basis of their actuation was electrolysis induced bubbling, which inflated an electrolyte-filled parylene balloon around a serpentine shaped silicon probe. No in vivo studies have been conducted to our knowledge using these probes.

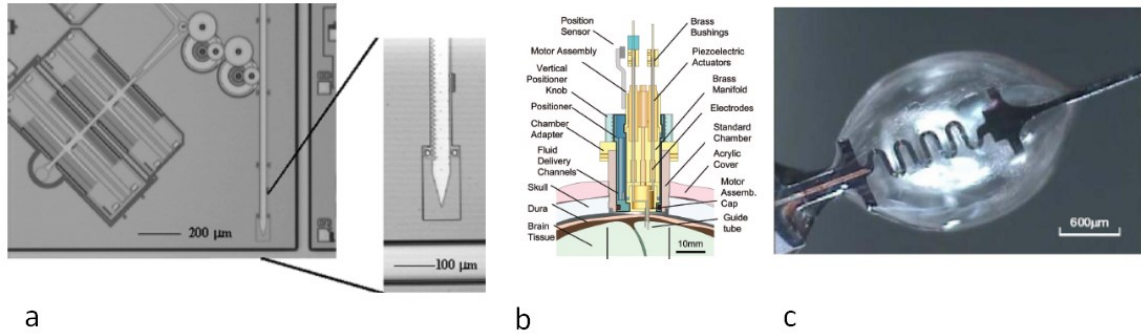


Figure 1-4. (a) Electrothermal based moveable probe [23]; (b) Motorized microdrive for moving neural probes [6]; (c) Fabricated parylene balloon actuator [24].

Actuation methods can either be incorporated into the microfabrication of neural interfaces or can be integrated in post-processing at the individual device level. Capacitive, electrostatic, electrothermal, shape memory alloys, and piezoelectric actuation methods are usually incorporated at the wafer level. While wafer level processing is usually preferred for standardization of MEMS devices, integrated processing combines restrictions for the neural probe and actuation technology, which typically reduces the yield. An actuation method that could be incorporated post-processing may allow for fabrication flexibility and customization. In addition, actuation methods should be considered for their biocompatibility and safe use, considering their power consumption, heat dissipation, voltage requirements, and overall size.

Passive moveable neural electrodes for chronic cortical recording are also being developed [25]. These microelectrodes are made from silicon and have extended electrode projections on horizontal springs that are retracted using starch, which shrinks upon dehydration. After insertion, the starch absorbs water, expands and releases the springs. While this approach is promising to deploy electrode sites horizontally, control of the starch swelling and shrinking needs to be demonstrated to prevent damage to the

surrounding tissue or device. A method to retract the electrode is not incorporated, so additional tissue damage may occur.

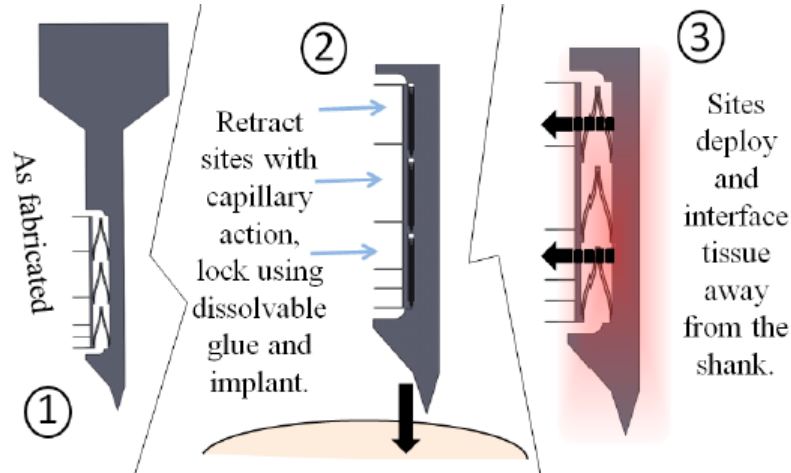


Figure 1-5. Spring-loaded electrode projections being developed [25].

Mechanisms of producing actuation at the micro-scale are limited and usually require incorporation during the fabrication processes. An actuation technology that can be incorporated post-release in standard microfabrication would have advantage over others that require process integration.

Conjugated polymer actuators for moving neural electrodes

Conjugated (aka electroactive or conducting) polymer actuators are one such technology within a class of smart materials that can be electrically polymerized on sections of interest and whose power requirements are promising for micro-sized medical applications. Conjugated polymer coatings have already been used for neural electrode site coatings to improve recording, increase the charge carrying capacity for stimulation, and for localized drug delivery [26-32].

1.2.2 Conjugated polymer actuators

Conjugated polymers (CP) are electronically conducting organic polymers within a class of intelligent electroactive polymer (EAP) materials that respond to their environment. These polymers are characterized by having alternating single and double bonds between the carbon atoms along the polymer backbone [33, 34].

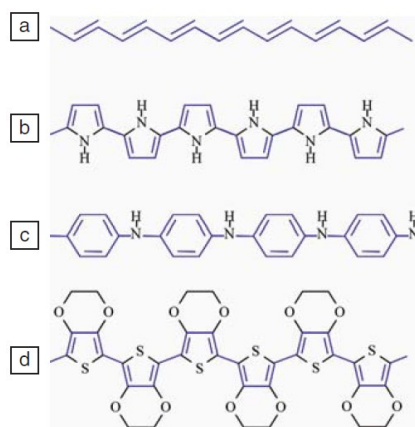


Figure 1-6. Structures of some conjugated polymers in their neutral states: (a) polyacetylene, (b) polypyrrole (PPy), (c) polyaniline, and (d) poly(3,4-ethylenedioxythiophene) (PEDOT). The conjugation path is indicated in blue. (Image from [35])

Polymerization

Oxidation of the monomer produces a radical cation, which then combines with another monomer to form a trimer. Subsequent oxidation leads to a progressive increase in chain length to create a polymerized structure. CPs are electrically polymerized in the oxidized (“doped”) state; therefore, to maintain overall charge neutrality, negatively charged anions are incorporated into the matrix during deposition. Polymerization can be achieved by chemical polymerization, photochemical polymerization, enzyme-catalyzed polymerization, and electrochemical polymerization, which is the main method used for actuators [36]. Electrochemical polymerization can be done potentiostatically (constant potential) or galvanostatically (constant current). A three-electrode configuration is used,

in which a working electrode, connected to the sample, a counter electrode, and reference electrode are electrochemically connected through an electrolytic solution. The counter electrode should be made from a chemically inert metal and larger than the working electrode. The reference electrode is typically a Ag-Ag/Cl electrode.

Oxidation and reduction

Mobile positive charges are produced when electrons are removed from the charge-neutral polymer (i.e., when the polymer is oxidized), making the material electrically conducting. Change in polymer conductivity is based on its oxidation state and ionic composition [37, 38]. Oxidation can be achieved electrochemically, and it is reversible. Their oxidation state can be changed electrochemically by adding or removing charge from the polymer backbone, resulting in a flux of ions to balance the charge. Applying a sufficiently negative potential returns the electrons to the polymer, reducing it. Ion flux induced by the electrostatic effect is referred to as migration. Ion flux may also occur due to entropic forces as a result of concentration gradients. This movement is called diffusion and can be predicted by Fick's laws. Which type of flux is dominant depends on the magnitude of the applied potential [39].

Cyclic voltammetry

Reducing and oxidizing the polymer can be done by either applying a potential to the polymer with respect to the electrolyte or by directly inducing a current. For characterization, a triangle wave of potential is applied and current is measured. This method is called cyclic voltammetry (CV) and the scan rate of the sweep can be varied to observe electron flow, some of which is indicative of ion flux [40, 41]. The magnitude of the voltage potential applied should be sufficient to drive the oxidation and reduction

processes. Consideration of the voltage on the electrolyte is also important. Voltage potential greater than 0.8 V or less than -1 V will cause electrolysis of water. Larger potentials (± 5 V) can be applied when cycling in organic solvents (e.g. propylene carbonate), however, damage to the polymer then becomes limiting. The oxidation and reduction potentials can be estimated from the peak positions, as shown in Figure 1-7, and the peak areas reflect the amount of charge passed. However, not all of the charge exchanged has been accounted for [42].

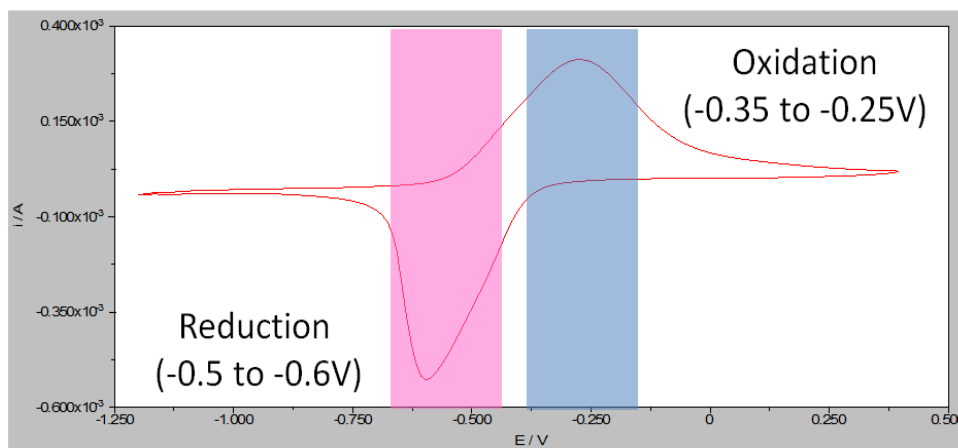


Figure 1-7. Typical current vs. voltage profile from a cyclic voltammetry cycle for PPy(DBS) cycled in 0.1 M NaDBS. Current peaks are associated with ion ingress and egress from the polymer matrix.

Ion exchange and actuation

To maintain charge neutrality in the case of anion-exchanging polymers, the negative charge added to the polymer drives the dopant anions out into the surrounding electrolyte. Alternatively, if the anions that were incorporated during polymerization are too large to exit and are thus entrapped in the polymer, cations are pulled in by the electrostatic forces. These are called cation-exchanging polymers.

Ions in the electrolyte are surrounded by a shell of solvent; water in biomedical applications. The water molecules inserted can be divided into two types: those tightly bound to the cations (corresponding approximately to the inner solvation shell), and those driven into the film by a slower process depending on the osmotic pressure difference between the film and the electrolyte solution [41].

Influx and efflux of hydrated ions cause a change in polymer volume that can be harnessed to perform mechanical work. Thus, CP actuators induce an actuation strain directly as a result of ion transport [43-45]. Consequently, the solvated polymer results in a change of its Young's moduli as function of oxidation state [46, 47].

Comparing alkali ions (Li, Na, K, Rb, Cs), lithium has the smallest atomic volume and highest charge density. Therefore, in aqueous electrolytes it will have the largest hydration shell and effective size [48]. Both the velocity and actuation strain were found to decrease with the atomic mass of the alkali cations [45].

Small anions, such as Cl^- , may also participate in charge balance in PPy(DBS), becoming incorporated during oxidation and ejected during reduction [49-52]. These typically have a different mobility in the polymer than the cations and a different potential window in which they are exchanged. The simultaneous transport of anions and cations in opposite directions at different speeds can result in a reversal in the strain direction [43, 53, 54]. Non-monotonic motion is problematic for control over actuator position.

The actuation strain (change in length divided by original length, $\Delta L/L$) is positive upon ion and solvent influx, and its magnitude depends on the number of solvent molecules accompanying the ion in its solvation shell. In cation-exchanging materials, lower atomic

weight cations, which have a higher charge density and are thus surrounded by larger hydration shells, produce greater force [55] and displacement [40, 41, 55].

Divalent cations interact more strongly with the polymer than monovalent cations, and they have a lower mobility [56]. Divalent cations require a stronger driving force for insertion into the polymer [57] and result in less swelling during polymer reduction [50] than monovalent cations.

PPy(DBS)

Polypyrrole (PPy) doped with dodecylbenzenesulfonate (DBS) is one example of a cation-exchanging material, where a large number of anions are incorporated: one for every 3-4 pyrrole units [58]. The anions therefore strongly influence the structure of the material, and thus the mechanical and electrical properties. PPy(DBS) has been previously characterized in some depth upon cycling in aqueous NaCl and NaDBS. In aqueous solutions containing Na⁺, the actuation strain in the plane of the film (i.e. parallel to the surface) is approximately 3% in the bulk [41, 59]. (In films ~1 μm thick, the out of plane actuation strain is ten times larger [60].) The inplane actuation strain is what leads to bending in bilayer actuators. A small number of anions, such as chlorine, may also participate in charge balance in PPy(DBS), reducing the net strain [52, 61]. Initial tests of actuators operating with elevated temperatures resulted in greater curvature in bilayer actuators [62, 63].

There have been several demonstrations of the use of CP actuators in biomedical applications in vitro and in vivo [64-68]. Several factors make these actuators promising. CPs have been shown to be biocompatible [69-71], and their low actuation voltages (< 1

V) are considered benign for interactions with biological tissues [65, 71, 72]. The immunoreactivity of PPy(DBS) has previously been shown by histological testing to be favorable [65, 71, 72]. Although they are gradually degraded by operation in aqueous electrolytes [73], they are stable for short-term use (up to several thousand cycles). These actuators can exert substantial forces [74, 75] because of their high Young's moduli (0.1 – 100 GPa) [33, 76]. In addition, they can be readily integrated with standard microfabrication processes [77].

Multivariable conditions

The prior demonstrations of biomedical applications [64-68] did not characterize actuation strain or deflection in those media. PPy(DBS) actuation has, however, been tested in several ionic solutions and temperature ranges. The majority of these studies have been done by systematically cycling one cation at a time [45, 62, 78] or by cycling in a solution with a single anion and cation, such as NaCl [79, 80]. PPy(DBS) has not yet been characterized in the ionic mixture and temperature found in the brain. For the long-term goal of producing movable neural interfaces, performance in cerebrospinal fluid (CSF) at body temperature needs to be determined.

Ionic components in CSF are listed in Table 1-1. The primary constituents are Na⁺ and Cl⁻. CSF also contains glucose, proteins (430 mg/L), and lymphocytes (< 4 μm³), and it is maintained at a pH of 7.31 [81, 82]. Artificial cerebrospinal fluid (aCSF) is used in lab settings to match the electrolyte concentrations of CSF, but it lacks the other components. Monovalent and divalent cations, as well as anions are found in CSF. In addition, body temperature 37 °C is elevated compared to room temperature, which the majority of prior characterization work was characterized. Prior work studying the effect of temperature

demonstrated that actuators operating at elevated temperatures have shown greater strain [62, 63] and accelerated creep [83].

Table 1-1. Ionic components of artificial cerebrospinal fluid [81].

CSF Ionic Component		Hydrated Radius (pm) [48]	Concentration (mM)
Sodium	Na ⁺	450	135-150
Chlorine	Cl ⁻	300	115-130
Potassium	K ⁺	300	2.6-3.0
Calcium	Ca ²⁺	600	1.0-1.4
Magnesium	Mg ²⁺	800	1.2-1.5
Phosphate	*PO ₄ ³⁻	400	0.4-0.6

* The charge depends on pH, going from PO₄³⁻ at high pH to H₃PO₄ at low pH.

CP actuator performance therefore depends not only on the synthesis medium, but also on the medium in which it is employed. Several reviews and prior work elaborate the multitude of factors that can affect CP actuation performance [78, 84-86]. While many of these factors are better understood than others, some are subtle and yet critical to the reliable performance of the actuators. For instance, polymerizing at higher currents than 1 mA/cm² has been shown to reduce actuation strain [86-88]. Because the roles of each factor or their combinations are not yet fully understood, new operation conditions must be characterized in terms of critical performance characteristics.

Elemental analysis

To help determine ionic species exchanged with the electrolyte, energy-dispersive x-ray spectroscopy (EDX) can be performed to reveal elements present in a polymer sample. An example of EDX spectra from a PPy(DBS) sample cycled in NaDBS at 22 °C is shown in Figure 1-8. EDX is not quantitative without comparison to a reference sample with a similar composition. Furthermore, the areas under EDX peaks for different

species cannot be used to obtain relative concentrations, so these spectra can only be used to compare relative amounts of the same element.

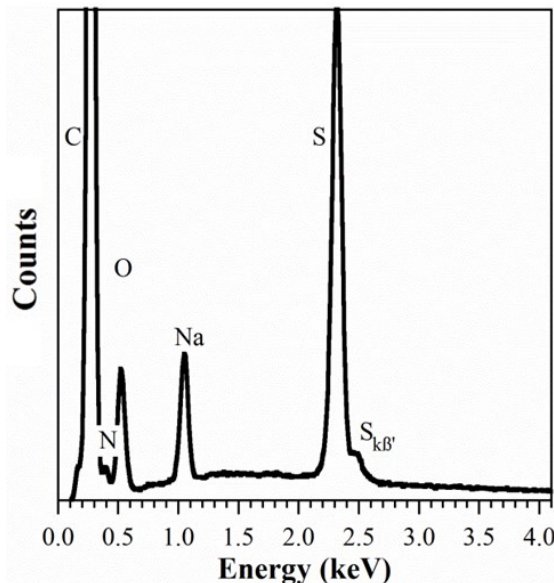


Figure 1-8. EDX spectra of a PPy(DBS) sample cycled in NaDBS at 22 °C.

1.2.3 Actuation performance measurands

CP actuator performance is subject to the polymer type, synthesis conditions, as well as the medium which it is employed [78, 84-86]. Intrinsic properties are independent of dimensions; however, since the physics of CP actuators is not completely known, lumped parameters of measuring CP material properties and actuation performance are used. The left diagram in Figure 1-9 indicates limiting scope of what can be identified in relation between the intrinsic properties of CP's and their actuation performance. The simple right diagram indicates that the chemical, electrical, and mechanical processes of CP actuators are inextricably linked.

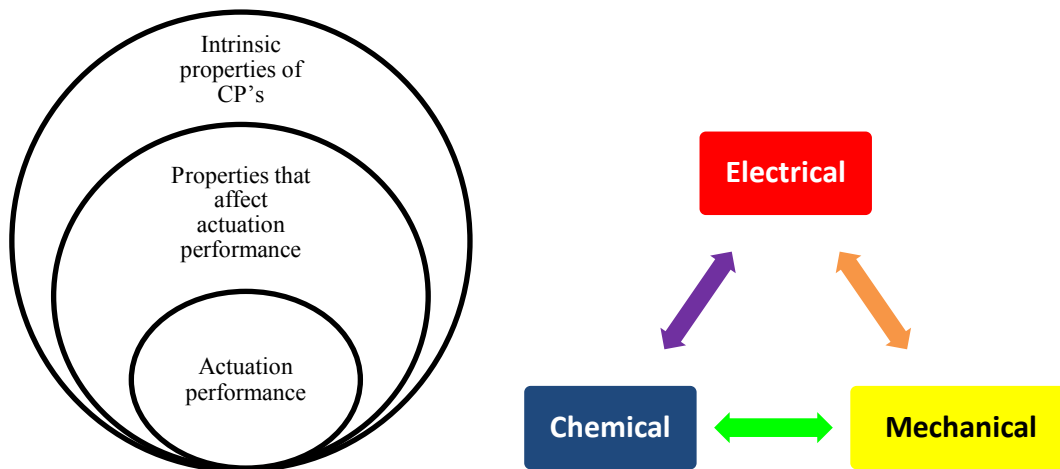


Figure 1-9. (Left) Diagram identifying the relationship of CP intrinsic properties and actuation performance. (Right) Diagram indicating that the electrical, chemical, and mechanical properties are inextricably linked.

Actuation strain

The essential CP actuation performance measurand is its actuation strain and range of elasticity under stress. Actuation strain refers to the inplane elongation or shrinking ($\Delta L/L$) done by the actuator and should not be confused with the bending strain of a composite bilayer. In a bilayer, it is what the polymer would achieve if it were not attached to the substrate. The reported actuation strain for PPy(DBS) has been on the order of ~3% [46, 49, 59] with some reports up to 5% [36]. Differences in actuation strain with cycling in different electrolytes have been shown previously [41, 56, 89]. The actuation bulk force, the amount where it no longer produces work, is the stress limit.

Polymer thickness

The thickness and density of the polymer matrix, as a result of the polymerization conditions, introduce multiple ion-exchange processes [90]. The polymer thickness can be estimated by the amount of charge passed during polymerization [77]. The speed of actuation is determined by the rate of ion exchange, which occurs either by diffusion,

movement of species down a concentration gradient, or migration (drift), movement under a force such as charged particle in an electric field [42]. The actuation speed is a function of ionic mobility (subject to ionic charge, temperature, electronegativity, and concentration gradient); therefore, it is an important measurand to consider since it can help differentiate competing electrochemical processes [40, 41, 90-93]. The transition of dominate ion-exchange processes may be used for classification between thin films and thicker films, which occurs between 3-5 μm [94, 95].

Actuation strain-to-charge ratio

CP actuation is an electrochemical process; therefore, the actuation strain-to-charge ratio per unit volume (or weight) may be used to compare its ability to convert electrical charge to mechanical strain [96, 97]. Polypyrrole polymerized with tetrabutylammonium hexafluorophosphate ($\text{TBA}\cdot\text{PF}_6$) had an actuation strain-to-charge ratio of $1.2\text{-}1.4\times 10^{-10}$ % / (C/m^3), cycled in propylene carbonate (PC) [96, 97] and PPy(sodium benzenesulfonate) (films purchased from BASF) was reported having 30×10^{-10} % / (C/m^3), cycled in acetonitrile [98, 99]. Due to the nature of how the CP's properties are subject to their environment, these intrinsic measurands are functions of multiple extrinsic variables and interlinked processes.

Young's moduli E_{PPy}

The Young's modulus of a material is taken as the slope of the linear portion of the stress-strain curve. To obtain this curve, a variable amount of stress is applied and the axial strain is measured. This is typically done using a tensile test machine (e.g. Instron or Shimadzu). The Young's modulus of a CP is known to change based on the redox state due to the influx and efflux of hydrated ionic species when cycled in water [47].

The PPy(DBS) Young's moduli work that is heavily cited reported E_{PPy} 200 ± 34 MPa when reduced and 450 ± 55 MPa when oxidized [91, 100]. In their work, PPy(DBS) was galvanostatically deposited on a stainless steel electrode, then peeled off and dried. The film (10 μm thick, 5 mm long, 3 mm wide) was mechanically attached to a force-displacement setup that maintained a constant force.

More thorough studies testing mechanical properties have been done with PPy(TBA·PF₆) in a solution of PC. PPy(TBA) Young's moduli has been shown to vary as a function of oxidation state, load, and frequency [47], actuation potential [101], as well as effect on work output in different oxidation states [100]. As a consequence, values of E_{PPy} used should account for the operation conditions. In this work, the values of E_{PPy} for PPy(DBS) in the oxidation and reduction state were used accordingly.

1.2.4 Actuation performance testing methods

Free films

Traditionally, the performance of CP actuating materials has been characterized by their steady state performance when unattached to a substrate [91, 96, 102, 103]. This method consists of polymerizing the CP on an initial substrate and then peeling it and slightly pre-straining it on a tensile tester. Figure 1-10 shows two setups used for free film characterization.

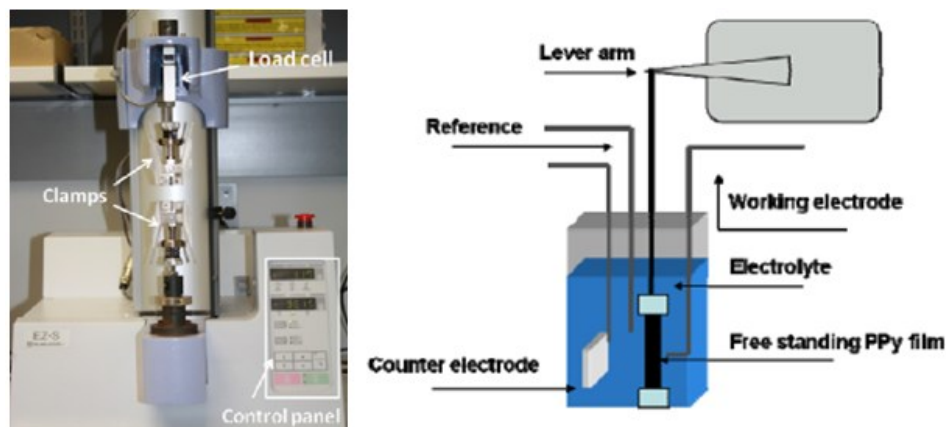


Figure 1-10. Two methods used for testing free films. (Left) Tensile test machine (Shimadzu), (Right) Aurora Scientific Inc. Dual Lever Arm system. Images from [104].

Bilayers

Observing the bending of a CP actuator attached to a substrate, resulting in a bilayer actuator is an alternative method used for characterization. The CP is typically electrically deposited on a thin metal film coated on a substrate layer [49, 55, 86, 105]; however, CP-Au bilayers have been also used [59, 106, 107]. In experimental setups using bilayer beams, one end is fixed and the deflection of the tip or curvature of the beam is measured. Knowing the material's Young's moduli and dimensions, the actuation strain can be determined using the Timoshenko equation [108], described in greater detail later.

Free films vs. bilayers

There are several important distinctions between free film and bilayer characterization methods that have implications on the applicability of their conclusions. Both the internal resistance of the polymer [75] and external ion transport barriers (e.g. bilayer substrate) [109] create rate-limiting steps to the electrochemical reactions. As an isolated thin-film, the internal resistance varies the conductivity along the strip length resulting in

the likelihood that the entire sample may not be fully contributing to active actuation. As a bilayer with a conductive interface, the electrical conductivity is consistent throughout the length, which has been shown to improve the force density six-fold [75].

In addition, unlike free-standing films where characterization can be done directly by applying a constant tensile force under isotonic conditions, the bilayer substrate acts as a restoring spring and changes the type of stress applied [100]. Therefore, applications where the use of CP actuators will resemble bilayers, the characterization under stresses generated from bilayer studies would be more applicable.

Induced strain actuators: Axial loading vs. bilayer stiffness

The volume change during CP actuation produces an induced strain in the polymer that can be harnessed for work. In the case of axial loading of a thin film, the inplane induced strain from the actuator generates an axial stress leading to contraction or elongation displacement. As shown in Figure 1-11, the actuator may work against a dead weight or a restoring spring. The optimal work output against a restoring spring occurs when the stiffness ratio of the external spring constant over the effective actuator spring constant is equal to one [110].

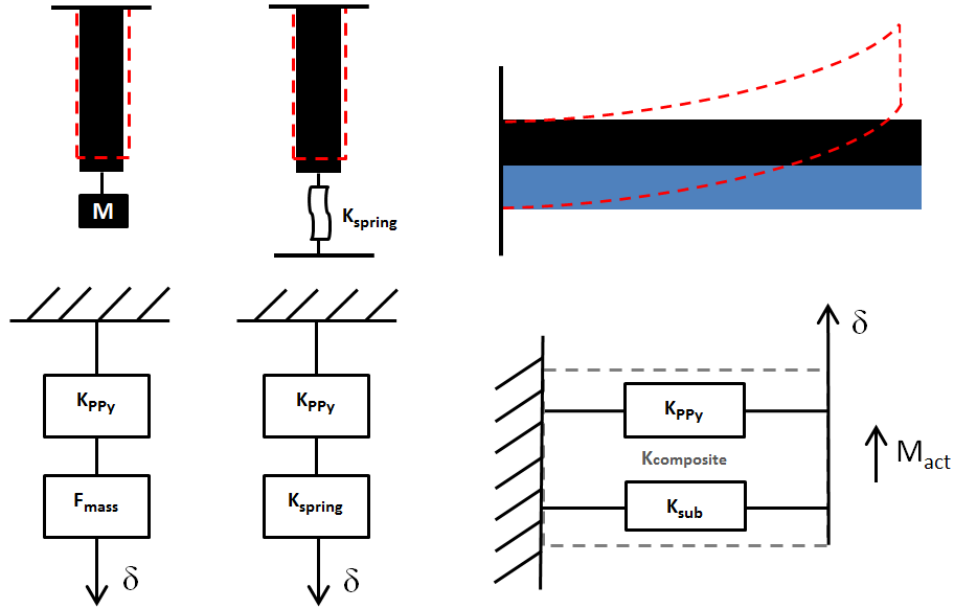


Figure 1-11. Graphics to help compare the loading of free films and bending actuators: (Left) axially-loaded free film by a dead weight, (Middle) axially-loaded free film against a spring, (Right) bilayer actuator bending a substrate.

In the case of an actuating bilayer cantilever, the inplane actuation strain generates an interfacial stress with the substrate resulting in a bending moment along the beam and an out-of-plane deflection, shown in Figure 1-11. Therefore, the out-of-plane stiffness is used. A cantilever beam of a single material has a spring constant of $k_{bending}$ given as:

$$(1) \quad k_{bending} = \frac{3 \cdot E \cdot I}{L^3} = \frac{E \cdot w \cdot t^3}{4 \cdot L^3}$$

A bilayer composite has a spring constant dependent on the effective beam stiffness, where the neutral axis could be in either layer.

$$(2) \quad k_{composite} = \frac{3 \cdot (E \cdot I)_{comp}}{L^3}$$

The ratio of the substrate layer stiffness k_{sub} to the CP layer stiffness k_{CP} is given as:

$$(3) \quad r = \frac{k_{sub}}{k_{CP}}$$

Based on reported dimensions and materials used, there have been a wide range of bilayer stiffness ratios for determining the performance of polymer actuators by bending (assuming E_{PPy} of 450 MPa) $r = 121$ [86], $r = 213$ [111], $r = 4,170$ & $112,597$ [55] (calculations detailed in the Supplemental Information). Figure 1-12 shows the relative thickness ratios for the PPy layer to the substrate used in the prior work referenced. All references used similar substrate materials, with varying amounts of metal deposited.



Figure 1-12. Relative thickness ratios of bilayer actuators used in prior work: a) $r = 121$ [86], b) $r = 213$ [111], c) $r = 4,170$ & d) $112,597$ [55].

As mentioned above, the actuation performance is subject to the type and magnitude of stress it is opposing, therefore, confusing these two may result in applying stresses outside the elastic limit and result in inaccuracies, dissimilar comparisons, or difficulty attributing changes to either the polymer Young's moduli or actuation strain [111].

1.2.5 Residual stress in bilayer actuators

The as-deposited PPy(DBS) is compact and it typically takes several cycles for the structure to open fully to accommodate ion ingress [52, 61], particularly for thick films. Upon the first-ever reduction of the film, the out-of-plane volume increases (approximately 60%) as cations and water are pulled into the polymer for the first time [42, 60, 112]. This initial polymer conformation change also creates an inplane strain.

In testing setups of isolated CP thin films, this initial expansion or contraction of the polymer is relieved by displacement adjustment to remove slack or relieve stress for

baseline measurements [50]. However, in bilayer films, this inplane strain results in a stress gradient with the underlying substrate. This work refers to this as a *residual stress*.

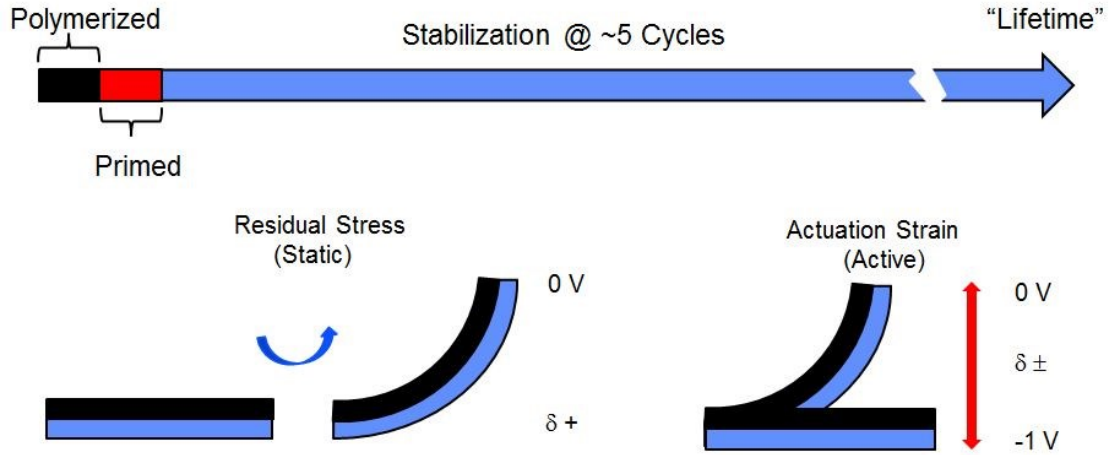


Figure 1-13. (Top) Identifying the stages of CP polymerization and conditioning. (Bottom) Graphic distinguishing deflection δ due to static residual stress and active actuation strain.

During reduction of PPy(DBS) in a solution containing only Na^+ , the hydrated Na^+ enters the polymer causing an expansion. The PPy induces a tensile stress, elongating the PPy, and thus bilayer bends with the PPy-side out. During oxidation the hydrated Na^+ leaves the polymer causing a contraction. The PPy induced a compressive stress, shrinking the PPy and bending the bilayer with the PPy-side in. From the perspective of the substrate, the polymer's tensile strain results in a compressive stress to the top of the substrate and similarly, the PPy's compressive strain results in a tensile stress to the top of the substrate.

Residual stresses are a major concern for MEMS devices as that they can dramatically influence the yield and functionality of a device. However, in some applications they may be designed for a specific purpose. Micro-sized medical applications have already

been discussed above. These applications may take advantage of designed residual stress in the ‘off’ state and released stress in the ‘on’ state [14].

Work done by residual stress

As a consequence of the change in modulus during CP cycling, the optimal stiffness ratio shifts and should be considered [100]. This shift is important to account for applications and will differ for anion vs. cation transporting actuators. Figure 1-14 shows the expected work-per-cycle as a function of the stiffness ratio of the substrate stiffness to conjugated polymer layer. The Young’s modulus when no voltage has been applied is given as Y and Y' after the voltage has been applied. Several scenarios are modeled accounting for the change in Young’s moduli. As mentioned above, in the case of cation-exchanging polymers such as PPy(DBS), the polymer modulus decreases significantly during reduction resulting in the scenario where $Y > Y'$. Consequently for bilayer actuators, the residual stress may be designed to perform mechanical work with no voltage applied. This scenario poses a unique opportunity to have devices with projections actuated out-of-plane without requiring a holding potential.

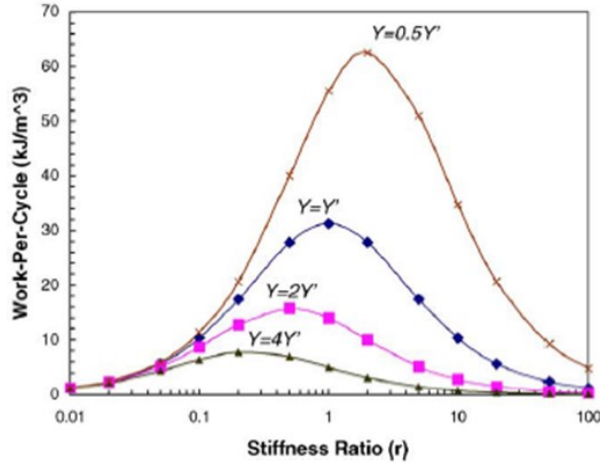


Figure 1-14. Work-per-cycle modeled as a function of stiffness ratio between the substrate and conjugated polymer, with Young's moduli as Y in the active state and Y' at rest. The curve for $Y >$ the case with the highest peak is for the cation-exchanging polymers (figure from [100]).

1.2.6 Macro vs. Micro-scale measurements

Forces due to inplane actuation strain under axial stress have been previously reported using a tensile testing machine with free films that were typically 15 μm thick, and cut to be 15–35 mm long and 1.5–2.5 mm wide. The peak load for which elastic deformation can be compensated is approximately 16 MPa [85], while forces greater than 20 MPa are impractical due to creep [83].

However, quantifying forces due to bending bilayer devices is not as straightforward. Bending of bilayer actuators is subject to their dimensions, substrate stiffness, and loading [100]. Therefore, the induced moment is more appropriate to report.

Challenges with micro-scale measurements

Previous actuation force measurements from bilayer devices have been attempted with difficulty. In one case, PPy(DBS) – KaptonTM bilayer devices (0.432 x 0.432 mm²) were loaded using a series of physical weights made from 0.1 mm thick glass cover slips, cut

with a diamond pen into $1 \times 1 \text{ mm}^2$ shapes with each weighing 0.52 mg, to gauge actuator output force [113]. Shown in Figure 1-15, the weights were stacked until the actuator could not lift any more, however, difficulty in placing them perfectly onto the center of the device resulted in inaccurate force measurements. This work was incomplete as a result. Another limitation was that the measurement resolution was bound by the size of the weights.

In this same work, the experimental setup was modified to use a force transducer (Aurora Scientific 406A, maximum force 0.5 mN, sensitivity $0.01 \mu\text{N}$). A tungsten needle was attached to the transducer arm and positioned at the tip of the beam, with aid of a microscope shown in Figure 1-15. They reported that this setup had significant difficulty as well due to three main sources of error: noise from external vibrations, sensor drift due to temperature changes, and error with sample positioning.

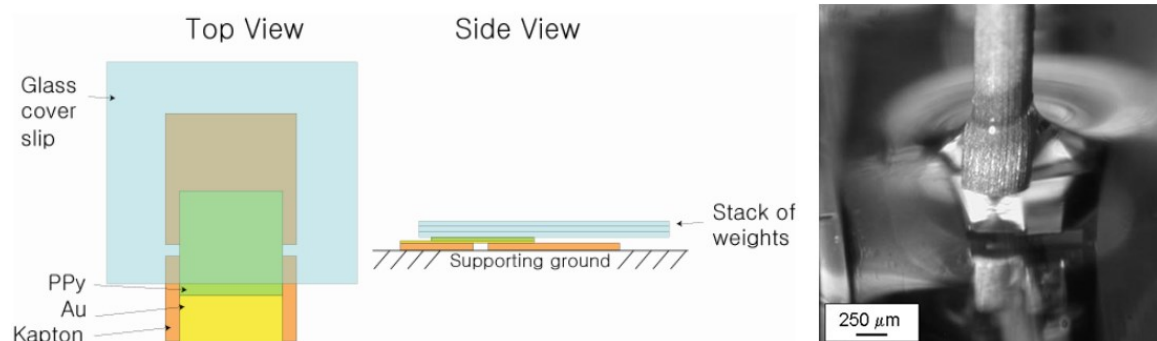


Figure 1-15. (Left) Experimental setup with glass weights used for actuation force measurement by [113]. (Right) Image of the tungsten needle being positioned on the beam tip (unpublished – courtesy of copyright holder E. Smela).

Previous MEMS devices for testing intrinsic material properties

MEMS technology has enabled techniques to calculate material properties using specially-designed structures and fundamental principles. These include the electrostatic

pull-in method [114], resonant frequency measurements of vibrating structures such as cantilevers or doubly supported bridges, and load-deflection approaches using composite structures and external equipment such as an AFM or surface profiler [115]. While some of these methods may be applicable for testing CPs, they either are too sensitive to environmental conditions, require the thin-film assumption that the added layer does not contribute to the substrate stiffness, or they rely on expensive external equipment. Both the electrostatic pull-in method and resonant frequency method are subject to damping, dielectric variations, electrolysis, anodization, or electrode polarization in ionic liquids [116].

1.3 Research objectives

Moveable neural electrodes are a new concept in the neural interfaces community. Conjugated polymer actuators present a unique opportunity to realize these devices. The objective of this research work is to investigate two critical aspects relating to the operation of these actuators for use in the motivating application. First, the actuation performance of PPy(DBS) under cerebral physiological conditions needs to be investigated. Second, the residual stress on the underlying substrate for bilayer actuators needs to be distinguished and quantified.

1.4 Summary of contributions

In summary, the objective of this research work was to investigate the potential use of conjugated polymer actuators for moving neural electrodes. The major contributions of this thesis were:

- Characterization of electroactive polymer PPy(DBS) actuation strain in artificial cerebrospinal fluid and at physiological temperature.

- Introduction of a MEMS tip-loaded conjugated polymer bilayer actuator test device for measuring micro-scaled actuation force and residual stress.
- Development and proof of concept of functional articulating neural electrodes.

1.5 References

- [1] W. M. Grill, S. E. Norman, and R. V. Bellamkonda, "Implanted neural interfaces: Biochallenges and engineered solutions," *Annu. Rev. Biomed. Eng.*, 11, 1-24, 2009.
- [2] J. D. Weiland, A. K. Cho, and M. S. Humayun, "Retinal prostheses: Current clinical results and future needs," *Ophthalmology*, 118, 2227-2237, 2011.
- [3] B. S. Wilson and M. F. Dorman, "Cochlear implants: A remarkable past and a brilliant future," *Hear. Res.*, 242, 3-21, 2008.
- [4] A. Compton, B. Shah, and S. Hayek, "Spinal cord stimulation: A review," *Curr. Pain. Headache. Rep.*, 16, 35-42, 2012.
- [5] B. Schlosshauer, L. Dreesmann, H. Schaller, and N. Sinis, "Synthetic nerve guide implants in humans: A comprehensive survey," *Neurosurgery*, 59, 740-747, 2006.
- [6] J. G. Cham, E. A. Branchaud, Z. Nenadic, B. Greger, R. A. Andersen, and J. W. Burdick, "Semi-chronic motorized microdrive and control algorithm for autonomously isolating and maintaining optimal extracellular action potentials," *J. Neurophysiol.*, 93, 570-579, 2005.
- [7] C. S. Bjornsson, S. J. Oh, Y. A. Al-Kofahi, Y. J. Lim, K. L. Smith, J. N. Turner, S. De, B. Roysam, W. Shain, and S. J. Kim, "Effects of insertion conditions on tissue strain and vascular damage during neuroprosthetic device insertion," *Journal of Neural Engineering*, 3, 196-207, 2006.
- [8] V. S. Polikov, P. A. Tresco, and W. M. Reichert, "Response of brain tissue to chronically implanted neural electrodes," *J. Neurosci. Methods*, 148, 1-18, 2005.
- [9] R. Biran, D. C. Martin, and P. A. Tresco, "Neuronal cell loss accompanies the brain tissue response to chronically implanted silicon microelectrode arrays," *Exp. Neurol.*, 195, 115-126, 2005.
- [10] M. A. Moffitt and C. C. McIntyre, "Model-based analysis of cortical recording with silicon microelectrodes," *Clinical Neurophysiology*, 116, 2240-2250, 2005.
- [11] J. P. Seymour and D. R. Kipke, "Neural probe design for reduced tissue encapsulation in CNS," *Biomaterials*, 28, 3594-3607, 2007.
- [12] J. P. Seymour and D. R. Kipke, "Fabrication of polymer neural probes with Sub-cellular features for reduced tissue encapsulation," *Conf. Proc. IEEE Eng. Med. Biol. Soc.*, New York, vol. 1, (August 30-September 3, 2006).

- [13] N. Jackson, A. Sridharan, S. Anand, M. Baker, M. Okandan, and J. Muthuswamy, "Long-term neural recordings using MEMS based movable microelectrodes in the brain." *Front. Neuroeng.*, 3, 1-13, 2010.
- [14] E. D. Daneshvar, E. Smela, and D. R. Kipke, "Mechanical characterization of conducting polymer actuated neural probes under physiological settings," *Proc. SPIE Smart Struct. Mater. (EAPAD)*, San Diego, vol. 7642, 1T.1-1T.10, edited by Y. Bar-Cohen (March 7-11, 2010).
- [15] E. D. Daneshvar, D. R. Kipke, and E. Smela, "Navigating conjugated polymer actuated neural probes in a brain phantom," *Proc. SPIE Smart Struct. Mater. (EAPAD)*, San Diego, vol. 8340, 09.1-09.12, edited by Y. Bar-Cohen (March 12-15, 2012).
- [16] S. F. Cogan, "Neural stimulation and recording electrodes," *Annu. Rev. Biomed. Eng.*, 10, 275-309, 2008.
- [17] D. Palanker, P. Huie, A. Vankov, A. Asher, and S. Baccus, "Towards high-resolution optoelectronic retinal prosthesis," *Ophth. Tech.*, 5688, 2005.
- [18] C. de Balthasar, S. Patel, A. Roy, R. Freda, S. Greenwald, A. Horsager, M. Mahadevappa, D. Yanai, M. J. McMahon, M. S. Humayun, R. J. Greenberg, J. D. Weiland, and I. Fine, "Factors affecting perceptual thresholds in epiretinal prostheses," *Invest. Ophthalmol. Vis. Sci.*, 49, 2303-2314, 2008.
- [19] L. T. Cohen, E. Saunders, M. R. Knight, and R. S. C. Cowan, "Psychophysical measures in patients fitted with Contour (TM) and straight Nucleus electrode arrays," *Hear. Res.*, 212, 160-175, 2006.
- [20] J. A. Saint-Cyr, T. Hoque, L. C. M. Pereira, J. O. Dostrovsky, W. D. Hutchison, D. J. Mikulis, A. Abosch, E. Sime, A. E. Lang, and A. M. Lozano, "Localization of clinically effective stimulating electrodes in the human subthalamic nucleus on magnetic resonance imaging," *J. Neurosurg.*, 97, 1152-1166, 2002.
- [21] D. J. Anderson, R. J. Vetter, J. F. Hetke and D. R. Kipke, "Neural interface system," US 08332046, December 11, 2012, 2012.
- [22] R. J. Vetter, D. R. Kipke and J. F. Hetke, "Three-dimensional system of electrode leads," US 08565894, OCT 22, 2013, 2013.
- [23] J. Muthuswamy, M. Okandan, A. Gilletti, M. S. Baker, and T. Jain, "An array of microactuated microelectrodes for monitoring single-neuronal activity in rodents," *IEEE Trans. Biomed. Eng.*, 52, 1470-1477, 2005.
- [24] C. Pang, Y. Tai, J. W. Burdick, and R. A. Andersen, "Electrolysis-based parylene balloon actuators for movable neural probes," *2nd IEEE International Conference on*

Nano/Micro Engineered and Molecular Systems, Bangkok, 913-916, edited by Anonymous (16-19 January 2007).

- [25] D. Egert and K. Najafi, "New class of chronic recording multichannel neural probes with post-implant self-deployed satellite recording sites," *IEEE Transducers*, Beijing, China, 958-961, edited by Anonymous (June 5-9, 2011).
- [26] X. Cui, J. F. Hetke, J. A. Wiler, D. J. Anderson, and D. C. Martin, "Electrochemical deposition and characterization of conducting polymer polypyrrole/PSS on multichannel neural probes," *Sensors and Actuators A: Physical*, 93, 8-18, 2001.
- [27] X. Y. Cui, J. Wiler, M. Dzaman, R. A. Altschuler, and D. C. Martin, "In vivo studies of polypyrrole/peptide coated neural probes," *Biomaterials*, 24, 777-787, 2003.
- [28] X. Y. Cui and D. C. Martin, "Electrochemical deposition and characterization of poly(3,4-ethylenedioxythiophene) on neural microelectrode arrays," *Sensors and Actuators B-Chemical*, 89, 92-102, 2003.
- [29] M. R. Abidian, D. H. Kim, and D. C. Martin, "Conducting-polymer nanotubes for controlled drug release," *Adv. Mater.*, 18, 405-+, 2006.
- [30] M. R. Abidian, L. G. Salas, A. Yazdan-Shahmorad, T. C. Marzullo, D. C. Martin, and D. R. Kipke, "In-vivo evaluation of chronically implanted neural microelectrode arrays modified with poly(3,4-ethylenedioxythiophene) nanotubes," *2007 3rd International IEEE/EMBS Conference on Neural Engineering, Vols 1 and 2*, 61-64, 2007.
- [31] K. A. Ludwig, J. D. Uram, J. Y. Yang, D. C. Martin, and D. R. Kipke, "Chronic neural recordings using silicon microelectrode arrays electrochemically deposited with a poly(3,4-ethylenedioxythiophene) (PEDOT) film," *Journal of Neural Engineering*, 3, 59-70, 2006.
- [32] K. A. Ludwig, N. B. Langhals, M. D. Joseph, S. M. Richardson-Burns, J. L. Hendricks, and D. R. Kipke, "Poly(3,4-ethylenedioxythiophene) (PEDOT) polymer coatings facilitate smaller neural recording electrodes," *Journal of Neural Engineering*, 8, 2011.
- [33] E. Smela, "Conjugated polymer actuators for biomedical applications," *Adv. Mater.*, 15, 481-494, 2003.
- [34] A. G. MacDiarmid, "Synthetic metals: a novel role for organic polymers," *Synth. Met.*, 125, 11-22, 2001.
- [35] E. Smela, "Conjugated polymer actuators," *MRS Bull.*, 33, 197-204, 2008.

- [36] G. Wallace, G. Spinks, L. Kane-Maguire and P. Teasdale, Conductive Electroactive Polymers
Intelligent Polymer Systems, 3rd ed. (CRC Press, Boca Raton, FL, 2009).
- [37] M. Yamaura, K. Sato, and T. Hagiwara, "Effect of Counter-Anion Exchange on Electrical-Conductivity of Polypyrrole Films," *Synth. Met.*, 39, 1990.
- [38] H. Zhao, W. E. Price, and G. G. Wallace, "Effect of the Counterion Employed during Synthesis on the Properties of Polypyrrole Membranes," *J. Membr. Sci.*, 87, 1994.
- [39] X. Z. Wang, B. Shapiro, and E. Smela, "Visualizing ion currents in conjugated polymers," *Adv. Mater.*, 16, 1605-1609, 2004.
- [40] M. A. Careem, Y. Velmurugu, S. Skaarup, and K. West, "A voltammetry study on the diffusion of counter ions in polypyrrole films," *J. Power Sources*, 159, 210-214, 2006.
- [41] M. J. M. Jafeen, M. A. Careem, and S. Skaarup, "Speed and strain of polypyrrole actuators: dependence on cation hydration number," *Ionics*, 16, 1-6, 2010.
- [42] X. Z. Wang and E. Smela, "Color and volume change in PPy(DBS)," *J. Phys. Chem. C*, 113, 359-368, 2009.
- [43] Q. B. Pei and O. Inganäs, "Electrochemical applications of the bending beam method; a novel way to study ion-transport in electroactive polymers," *Solid State Ionics*, 60, 161-166, 1993.
- [44] S. Shimoda and E. Smela, "The effect of pH on polymerization and volume change in PPy(DBS)," *Electrochim. Acta.*, 44, 219-238, 1998.
- [45] X. Z. Wang and E. Smela, "Cycling conjugated polymers with different cations," *Proc. SPIE Smart Struct. Mater. (EAPAD)*, San Diego, vol. 6168, (February 27-March 2, 2006).
- [46] L. Bay, N. Mogensen, S. Skaarup, P. Sommer-Larsen, M. Jorgensen, and K. West, "Polypyrrole doped with alkyl benzenesulfonates," *Macromolecules*, 35, 9345-9351, 2002.
- [47] T. Shoa, T. Mirfakhrai, and J. D. W. Madden, "Electro-stiffening in polypyrrole films: Dependence of Young's modulus on oxidation state, load and frequency," *Synth. Met.*, 160, 1280-1286, 2010.
- [48] J. Kielland, "Individual activity coefficients of ions in aqueous solutions," *J. Am. Chem. Soc.*, 59, 1675-1678, 1937.

- [49] Q. B. Pei and O. Inganäs, "Electrochemical applications of the bending beam method: 1. Mass-transport and volume changes in polypyrrole during redox," *J. Phys. Chem.*, 96, 10507-10514, 1992.
- [50] M. R. Gandhi, P. Murray, G. M. Spinks, and G. G. Wallace, "Mechanism of electromechanical actuation in polypyrrole," *Synth. Met.*, 73, 247-256, 1995.
- [51] S. Skaarup, K. West, L. M. W. K. Gunaratne, K. P. Vidanapathirana, and M. A. Careem, "Determination of ionic carriers in polypyrrole," *Solid State Ionics*, 136, 577-582, 2000.
- [52] H. Yang and J. Kwak, "Mass transport investigated with the electrochemical and electrogravimetric impedance techniques. 2. Anion and water transport in PMPy and PPy films," *J. Phys. Chem. B*, 101, 4656-4661, 1997.
- [53] B. Gaihre, S. Ashraf, G. M. Spinks, P. C. Innis, and G. G. Wallace, "Comparative displacement study of bilayer actuators comprising of conducting polymers, fabricated from polypyrrole, poly(3,4-ethylenedioxythiophene) or poly(3,4-propylenedioxythiophene)," *Sens. Act. A*, 193, 48-53, 2013.
- [54] N. Vandesteeg, P. G. Madden, J. D. Madden, P. A. Anquetil, and I. W. Hunter, "Synthesis and characterization of EDOT-based conducting polymer actuators," *Proc. SPIE Smart Struct. Mater. (EAPAD)*, San Diego, vol. 5051, 349-356, edited by Y. Bar-Cohen (March 2-6, 2003).
- [55] M. A. Careem, K. P. Vidanapathirana, S. Skaarup, and K. West, "Dependence of force produced by polypyrrole-based artificial muscles on ionic species involved," *Solid State Ionics*, 175, 725-728, 2004.
- [56] S. Skaarup, L. Bay, K. Vidanapathirana, S. Thybo, P. Tofte, and K. West, "Simultaneous anion and cation mobility in polypyrrole," *Solid State Ionics*, 159, 143-147, 2003.
- [57] R. John and G. G. Wallace, "Doping-dedoping of polypyrrole: a study using current-measuring and resistance-measuring techniques," *J. Electroanal. Chem.*, 354, 145-160, 1993.
- [58] A. F. Diaz and J. Bargon, "Electrochemical synthesis of conducting polymers " in Handbook of Conducting Polymers, T. A. Skotheim, Ed., (Dekker, New York, 1986).
- [59] M. Christophersen, B. Shapiro, and E. Smela, "Characterization and modeling of PPy bilayer microactuators - Part 1. Curvature," *Sens. Act. B*, 115, 596-609, 2006.
- [60] E. Smela and N. Gadegaard, "Surprising volume change in PPy(DBS): An atomic force microscopy study," *Adv. Mater.*, 11, 953-957, 1999.

- [61] H. Yang and J. Kwak, "Mass transport investigated with the electrochemical and electrogravimetric impedance techniques. 1. Water transport in PPy/CuPTS films," *J. Phys. Chem. B*, 101, 774-781, 1997.
- [62] M. Christophersen and E. Smela, "Polypyrrole/gold bilayer microactuators: Response time and temperature effects," *Proc. SPIE Smart Struct. Mater. (EAPAD)*, San Diego, vol. 6168, (February 27 - March 2, 2006).
- [63] S. Fanning, , "*Characterization of polypyrrole/gold bilayers for micro-valve design*," PhD. dissertation, University of Maryland, College Park, MD, 2005.
- [64] C. Immerstrand, K. Holmgren-Peterson, K. E. Magnusson, E. Jager, M. Krogh, M. Skoglund, A. Selbing, and O. Inganäs, "Conjugated-polymer micro- and milliaactuators for biological applications," *MRS Bull.*, 27, 461-464, 2002.
- [65] P. M. George, A. W. Lyckman, D. A. LaVan, A. Hegde, Y. Leung, R. Avasare, C. Testa, P. M. Alexander, R. Langer, and M. Sur, "Fabrication and biocompatibility of polypyrrole implants suitable for neural prosthetics," *Biomaterials*, 26, 3511-3519, 2005.
- [66] R. A. Green, N. H. Lovell, G. G. Wallace, and L. A. Poole-Warren, "Conducting polymers for neural interfaces: Challenges in developing an effective long-term implant," *Biomaterials*, 29, 3393-3399, 2008.
- [67] K. K. C. Lee, N. R. Munce, T. Shoa, L. G. Charron, G. A. Wright, J. D. Madden, and V. X. D. Yang, "Fabrication and characterization of laser-micromachined polypyrrole-based artificial muscle actuated catheters," *Sens. Act. A*, 153, 230-236, 2009.
- [68] E. W. H. Jager, E. Smela, and O. Inganäs, "Microfabricating conjugated polymer actuators," *Science*, 290, 1540-1545, 2000.
- [69] C. E. Schmidt, V. R. Shastri, J. P. Vacanti, and R. Langer, "Stimulation of neurite outgrowth using an electrically conducting polymer," *Proc. Natl. Acad. Sci.*, 94, 8948-8953, 1997.
- [70] R. L. Williams and P. J. Doherty, "A preliminary assessment of poly(pyrrole) in nerve guide studies," *J. Mater. Sci. Mater. Med.*, 5, 429-433, 1994.
- [71] X. D. Wang, X. S. Gu, C. W. Yuan, S. J. Chen, P. Y. Zhang, T. Y. Zhang, J. Yao, F. Chen, and G. Chen, "Evaluation of biocompatibility of polypyrrole in vitro and in vivo," *J. Biomed. Mater. Res. A*, 68A, 411-422, 2004.
- [72] D. D. Ateh, H. A. Navsaria, and P. Vadgama, "Polypyrrole-based conducting polymers and interactions with biological tissues," *J. R. Soc. Interface*, 3, 741-752, 2006.

- [73] Y. Liu, Q. Gan, S. Baig, and E. Smela, "Improving PPy adhesion by surface roughening," *J. Phys. Chem. C*, 111, 11329-11338, 2007.
- [74] B. Shapiro and E. Smela, "Bending actuators with maximum curvature and force and zero interfacial stress," *J. Intel. Mat. Syst. Str.*, 18, 181-186, 2007.
- [75] A. S. Hutchison, T. W. Lewis, S. E. Moulton, G. M. Spinks, and G. G. Wallace, "Development of polypyrrole-based electromechanical actuators," *Synth. Met.*, 113, 121-127, 2000.
- [76] L. Bay, K. West, and S. Skaarup, "Pentanol as co-surfactant in polypyrrole actuators," *Polymer*, 43, 3527-3532, 2002.
- [77] E. Smela, "Microfabrication of PPy microactuators and other conjugated polymer devices," *J. Micromech. Microeng.*, 9, 1-18, 1999.
- [78] S. Maw, E. Smela, K. Yoshida, and R. B. Stein, "Effects of monomer and electrolyte concentrations on actuation of PPy(DBS) bilayers," *Synthetic Metals*, 155, 18-26, 2005.
- [79] S. S. Pandey, W. Takashima, and K. Kaneto, "Conserved electrochemomechanical activities of polypyrrole film in complex buffer media," *Sens. Act. B*, 102, 142-147, 2004.
- [80] W. Takashima, S. S. Pandey, and K. Kaneto, "Cyclic voltammetric and electrochemomechanical characteristics of freestanding polypyrrole films in diluted media," *Thin Solid Films*, 438, 339-345, 2003.
- [81] E. C. McNay and R. S. Sherwin, "From artificial cerebro-spinal fluid (aCSF) to artificial extracellular fluid (aECF): microdialysis perfusate composition effects on in vivo brain ECF glucose measurements," *J. Neurosci. Methods*, 132, 35-43, 2004.
- [82] I. S. Kass, A. A. Bendo, A. E. Abramowicz, and J. E. Cottrell, "Methods for studying the effect of anesthetics on anoxic damage in the rat hippocampal slice," *J. Neurosci. Methods*, 28, 77-82, 1989.
- [83] J. D. Madden, D. Rinderknecht, P. A. Anquetil, and I. W. Hunter, "Creep and cycle life in polypyrrole actuators," *Sens. Act. A*, 133, 210-217, 2007.
- [84] P. G. A. Madden, J. D. W. Madden, P. A. Anquetil, N. A. Vandesteeg, and I. W. Hunter, "The relation of conducting polymer actuator material properties to performance," *IEEE J. Ocean. Eng.*, 29, 696-705, 2004.
- [85] J. D. W. Madden, P. G. A. Madden, and I. W. Hunter, "Conducting polymer actuators as engineering materials," *Proc. SPIE Smart Struct. Mater. (EAPAD)*, San Diego, CA, vol. 4695, (Mar 18-21, 2002).

- [86] S. Maw, E. Smela, K. Yoshida, P. Sommer-Larsen, and R. B. Stein, "The effects of varying deposition current density on bending behaviour in PPy(DBS)-actuated bending beams," *Sens. Act. A*, 89, 175-184, 2001.
- [87] S. Skaarup, K. West, B. Zachaustriensen, M. A. Careem, and G. K. R. Senadeera, "Electrolyte and ion memory effects in highly conjugated polypyrrole," *Solid State Ionics*, 72, 108-114, 1994.
- [88] K. West, T. Jacobsen, B. Zachaustriensen, M. A. Careem, and S. Skaarup, "Electrochemical synthesis of polypyrrole - Influence of current-density on structure," *Synth. Met.*, 55, 1412-1417, 1993.
- [89] S. Skaarup, M. J. M. Jafeen, and M. A. Careem, "Determination of membrane hydration numbers of alkali metal ions by insertion in a conducting polymer," *Solid State Ionics*, 181, 1245-1250, 2010.
- [90] T. F. Otero and J. M. Garcia de Otazo, "Polypyrrole oxidation: Kinetic coefficients, activation energy and conformational energy," *Synth. Met.*, 159, 681-688, 2009.
- [91] L. Bay, T. Jacobsen, S. Skaarup, and K. West, "Mechanism of actuation in conducting polymers: Osmotic expansion," *J. Phys. Chem. B*, 105, 8492-8497, 2001.
- [92] B. J. West, T. F. Otero, B. Shapiro, and E. Smela, "Chronoamperometric study of conformational relaxation in PPy(DBS)," *J. Phys. Chem. B*, 113, 1277-1293, 2009.
- [93] S. Skaarup, L. Bay, and K. West, "Polypyrrole actuators working at 2-30 Hz," *Synth. Met.*, 157, 323-326, 2007.
- [94] T. F. Otero and J. G. Martinez, "Activation energy for polypyrrole oxidation: film thickness influence," *Journal of Solid State Electrochemistry*, 15, 2011.
- [95] M. J. Higgins, S. T. McGovern, and G. G. Wallace, "Visualizing Dynamic Actuation of Ultrathin Polypyrrole Films," *Langmuir*, 25, 2009.
- [96] J. D. W. Madden, P. G. A. Madden, and I. W. Hunter, "Polypyrrole actuators: modeling and performance," *Proc. SPIE Smart Struct. Mater. (EAPAD)*, Newport Beach, vol. 4329, 72-83, edited by Y. Bar-Cohen (March 5-8, 2001).
- [97] P. A. Anquetil, D. Rinderknecht, N. A. Vandesteeg, J. D. Madden, and I. W. Hunter, "Large strain actuation in polypyrrole actuators," *Proc. SPIE Smart Struct. Mater. (EAPAD)*, San Diego, vol. 5385, 380-387, edited by Y. Bar-Cohen (March 15-18, 2004).
- [98] A. Della Santa, D. De Rossi, and A. Mazzoldi, "Characterization and modelling of a conducting polymer muscle-like linear actuator," *Smart Mater. Struct.*, 6, 23-34, 1997.

- [99] A. Della Santa, D. De Rossi, and A. Mazzoldi, "Performance and work capacity of a polypyrrole conducting polymer linear actuator," *Synth. Met.*, 90, 93-100, 1997.
- [100] G. M. Spinks and V. T. Truong, "Work-per-cycle analysis for electromechanical actuators," *Sensors and Actuators A-Physical*, 119, 2005.
- [101] G. M. Spinks, D. Z. Zhou, L. Liu, and G. G. Wallace, "The amounts per cycle of polypyrrole electromechanical actuators," *Smart Materials & Structures*, 12, PII S0964-1726(03)62089-6, 2003.
- [102] T. F. Otero, G. Vazquez Arenas, and J. J. Lopez Cascales, "Effect of the doping ion on the electrical response of a free-standing polypyrrole strip subjected to different preloads: Perspectives and limitations associated with the use of these devices as actuators," *Macromolecules*, 39, 2006.
- [103] K. Kaneto, H. Fujisue, M. Kunifusa, and W. Takashima, "Conducting polymer soft actuators based on polypyrrole films - energy conversion efficiency," *Smart Materials & Structures*, 16, 2007.
- [104] Wen Zheng. , "*Analysis of high performance polypyrrole actuators*," PhD, University of Wollongong, 2011.
- [105] Q. B. Pei and O. Inganäs, "Electrochemical applications of the bending beam method: 2. Electroshrinking and slow relaxation in polypyrrole," *J. Phys. Chem.*, 97, 6034-6041, 1993.
- [106] S. Fanning, Y. Liu, M. Christophersen, M. Duerkop, E. Smela, and B. Shapiro, "Polypyrrole/gold bilayer characterization," *Proc. SPIE Smart Struct. Mater. (EAPAD)*, San Diego, CA, vol. 5759, 292-301, edited by Y. B. Cohen (Mar 07-10, 2005).
- [107] Steven Fanning, Yingkai Liu, Marc Christophersen, Matthias Duerkop, Elisabeth Smela, Benjamin Shapiro, "Polypyrrole/gold bilayer characterization," *Proc. SPIE Smart Struct. Mater. (EAPAD)*, San Diego, CA, USA, vol. 5759, edited by Anonymous ().
- [108] S. P. Timoshenko, "Analysis of bi-metal thermostats," *J. Opt. Soc. Am.*, 11, 233-255, 1925.
- [109] X. Z. Wang and E. Smela, "Experimental studies of ion transport in PPy(DBS)," *J. Phys. Chem. C*, 113, 369-381, 2009.
- [110] V. Giurgiutiu, C. A. Rogers, and Z. Chaudhry, "Energy-based comparison of solid-state induced-strain actuators," *J. Intell. Mater. Syst. Struct.*, 7, 1996.

- [111] P. Du, X. Lin, and X. Zhang, "A multilayer bending model for conducting polymer actuators," *Sensors and Actuators A-Physical*, 163, 2010.
- [112] E. Smela and N. Gadegaard, "Volume change in polypyrrole studied by atomic force microscopy," *J. Phys. Chem. B*, 105, 9395-9405, 2001.
- [113] Lance Hyo Oh. , "*Development of micro-valves actuated by polypyrrole gold bilayers*," M.S., University of Maryland, College Park, 2003.
- [114] K. Najafi and K. Suzuki, "Measurement of fracture-stress, Young modulus, and intrinsic stress of heavily boron-doped silicon microstructures," *Thin Solid Films*, 181, 251-258, 1989.
- [115] S. D. Senturia, Microsystem Design(Springer, 2000).
- [116] V. Mukundan and B. L. Pruitt, "MEMS electrostatic actuation in conducting biological media," *J. Microelectromech. Syst.*, 18, 405-413, 2009.

CHAPTER 2 Characterization of conjugated polymer actuation under cerebral physiological conditions

This Chapter has been accepted for publication in *Advanced Healthcare Materials*. Co-author Professor Elisabeth Smela, University of Maryland, contributed significantly to the data analysis.

Abstract

Conjugated polymer actuators have potential use in implantable neural interface devices for modulating the position of electrode sites within brain tissue or guiding insertion of neural probes along curved trajectories. The actuation of polypyrrole (PPy) doped with dodecylbenzenesulfonate (DBS) was characterized to ascertain whether it could be employed in the cerebral environment. Microfabricated bilayer beams were electrochemically cycled at either 22 or 37 °C in aqueous NaDBS or in artificial cerebrospinal fluid (aCSF). Nearly all the ions in aCSF were exchanged into the PPy – the cations Na^+ , K^+ , Mg^{2+} , Ca^{2+} , as well as the anion PO_4^{3-} ; Cl^- was not present. Nevertheless, deflections in aCSF were comparable to those in NaDBS and they were monotonic with oxidation level: strain increased upon reduction, with no reversal of motion despite the mixture of ionic charges and valences being exchanged. Actuation depended on temperature. Upon warming, the cyclic voltammograms showed additional peaks and an increase of 70% in the consumed charge. Bending was, however, much less affected: strain increased somewhat (6-13%) but remained monotonic, and deflections

shifted (up to 20%). These results show how the actuation environment must be taken into account, and demonstrate proof of concept for actuated implantable neural interfaces.

2.1 Introduction

Conjugated polymers are a class of so-called “intelligent” materials because they respond to electrical stimuli and to their external environments. One response is a change in volume, which has led to their use as actuators. Several factors make such actuators promising for biomedical applications, as reviewed in [1], and there have been demonstrations of this, both in vitro and in vivo [2-6]. Conjugated polymers have been shown to be biocompatible [7-9], and their low actuation voltages (< 1 V) are considered benign for interactions with biological tissues [3, 9, 10]. These actuators can exert substantial forces [11, 12] because of their high elastic moduli (0.1 – 100 GPa) [1, 13]. In addition, they can be readily integrated with standard microfabrication processes [14].

For actuation, polypyrrole (PPy) is one of the most commonly used conjugated polymers. In this work, PPy doped with dodecylbenzenesulfonate, PPy(DBS) was used. The immunoreactivity of PPy(DBS) has previously been shown by histological testing to be favorable [3, 9, 10]. Although gradually degraded by operation in aqueous electrolytes, PPy(DBS) is stable for short-term use (up to several thousand cycles) [15].

Motivating the work presented here is the possibility of augmenting implantable neural interface devices with controllable bending elements. Adjusting the position of electrode sites within neural tissue to change electrode proximity to particular neurons may be beneficial for several reasons. For neural recording devices, the ability to move the electrode out of a damaged region may result in increased signal to noise ratios (SNR)

[16]. For neural stimulating devices, more accurate electrode placement may increase treatment efficacy and lower the charge injection required for stimulation [17, 18]. In addition, actuators may be used to guide the insertion of neural probe devices, allowing non-straight trajectories and active steering to target structures with precision, as needed for deep brain stimulation therapy [19]. Therefore, it is critical to understand the expected behavior of the actuator in the cerebral environment.

The feasibility of using PPy(DBS) to controllably bend neural electrodes within an agarose brain phantom during their insertion has been shown (Figure 2-1) [20]. Figure 2-1a shows an array of 5 probes immediately after fabrication; the beams are bent due to residual stress. The electrode beams in Figure 2-1b were actuated within the brain phantom (0.5% agarose and 0.1 M NaDBS), which has a stiffness similar to brain tissue. The PPy(DBS) produced sufficient force to move the electrodes out of plane during insertion into the gel, as required for cortical applications. Other applications, such as electrodes for the eye or ear, would operate in aqueous environments and encounter smaller opposing forces. Probes may also be bent at segments acting as joints (Figure 2-1c), rather than along the entire length. These results were promising for the potential use of conjugated polymers in neural interface devices.

In this Chapter, characterization of the behavior of the actuators, studying them at body temperature (37 °C) in artificial cerebrospinal fluid (aCSF), which contains a mixture of ions, is done. Actuation in NaDBS at room temperature (22 °C) is used as a comparison because extensive prior characterization has been performed in this electrolyte [21-23]. The performance is substantially the same, demonstrating that these actuators may be used under physiological conditions.

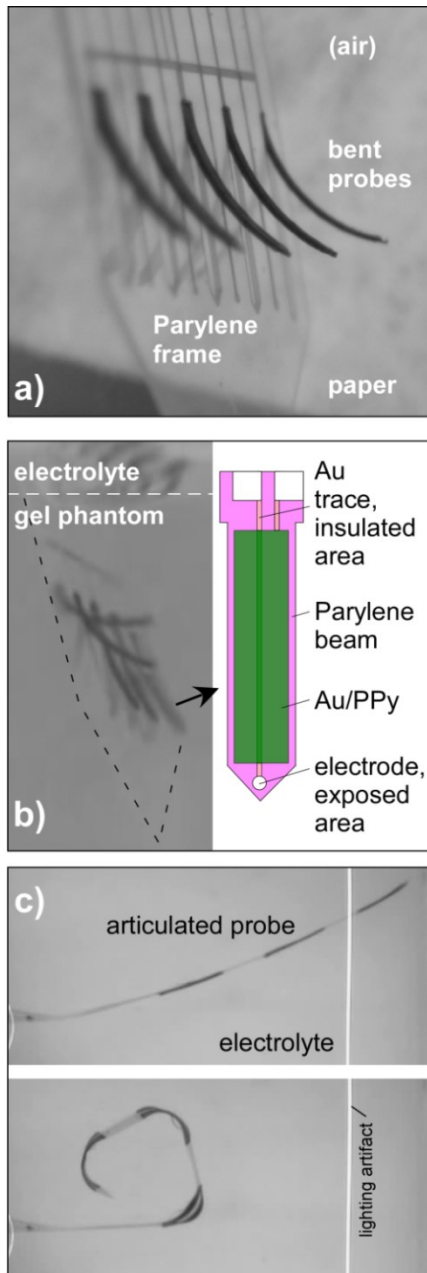


Figure 2-1. a) An array of 5 probe devices in air having lengths of 1 mm and widths between 50 μm and 250 μm , deflected out of plane with uniform curvature after fabrication, with no applied voltage. b) A similar set of probes with lengths of 800 μm actuated during penetration into a gel brain tissue phantom. The Parylene probe beams included an insulated electrode trace with an exposed Au electrode site at the tip and an overlying PPy/Au actuator. c) A segmented beam with actuators at three joints, electrochemically reduced to be straight (top) and oxidized to be bent (bottom) in NaDBS solution.

Actuation strain in aCSF was somewhat smaller than in NaDBS (by a factor of 0.89 at room temperature), and approximately the same charge density was exchanged (102%). Increasing the temperature to 37 °C resulted in a small increase in the actuation strain (by 13% in NaDBS and 6% in aCSF), but also a significant increase in the exchanged charge (by ~67% in both cases). Elemental analysis showed that in addition to Na, samples cycled in aCSF contained Mg, Ca, K, P and O (from PO_4^{3-} and its protonated forms), but no Cl. Despite the substantial amount of PO_4^{3-} , the actuation remained monotonic with voltage and did not reverse due to anion ingress and egress.

2.1.1 Conjugated polymer actuators

Conjugated polymers such as polypyrrole are characterized by alternating single and double bonds between the carbon atoms along the polymer backbone [1, 24]. Mobile positive charges are produced when electrons are removed from the charge-neutral polymer (i.e., when the polymer is oxidized), making the material electrically conducting. PPy is electro-polymerized in the oxidized (“doped”) state. Therefore, to maintain overall charge neutrality during film deposition, negatively charged anions are incorporated into the matrix. A large number of anions are incorporated: one for every 3-4 pyrrole units [25]. The anions therefore strongly influence the structure of the material, and thus the mechanical and electrical properties. It is thus necessary to specify the anion used during deposition when naming the polymer; PPy(DBS) and PPy(ClO_4) have quite different microstructures and behaviors.

Oxidation can be achieved electrochemically, and it is reversible: applying a sufficiently negative potential returns the electrons to the polymer, reducing it to the neutral state. To

maintain charge neutrality in the material, the dopant anions are expelled into the surrounding electrolyte, if the anions are small enough (such as ClO_4^-); these are anion-exchanging polymers. Alternatively, if the anions that were incorporated during polymerization are too large to exit (such as DBS^-) and are thus entrapped in the polymer, then during reduction cations are pulled in by the electrostatic forces (cation-exchanging polymers). The exit or influx of ions, each surrounded by a “shell” of solvent (which is water in biomedical applications), causes a change in polymer volume that can be harnessed to perform mechanical work. (It also results in a change in the elastic modulus as a function of oxidation level [23, 26].)

The actuation strain is the change in length divided by original length, $\Delta L/L$, that would occur in a free-standing film due to redox. It is positive upon ion and solvent influx, and its magnitude depends on the number of solvent molecules accompanying the ion in its solvation shell. In cation-exchanging materials, lower atomic weight cations, which have a higher charge density and are thus surrounded by larger hydration shells [27], produce greater force [28] and displacement [21, 28, 29].

Divalent cations interact more strongly with the polymer than monovalent cations, and they have a lower mobility [22]. In other systems, they have been shown to electrostatically crosslink ionic polymer chains [30]. Divalent cations may require a stronger driving force (electrochemical potential) for insertion into or expulsion from the conjugated polymer [31] and result in less expansion during polymer reduction [32].

PPy(DBS) is one example of a cation-exchanging material, and it has been previously characterized in some depth upon cycling in aqueous NaCl and NaDBS. In aqueous

solutions containing Na^+ , the actuation strain α in the plane of the film (inplane, i.e. parallel to the surface) is approximately 3% in the bulk [21, 33]. The inplane actuation strain is what leads to bending in bilayer actuators. (The out of plane actuation strain (perpendicular to the surface) in thin films can be ten times larger [34].)

Small anions, such as Cl^- , may also participate in charge balance in PPy(DBS), becoming incorporated during oxidation and ejected during reduction [32, 35-37]. These typically have a different mobility in the polymer than the cations and a different potential window in which they are exchanged. The simultaneous transport of anions and cations in opposite directions at different speeds can result in a reversal in the strain direction [38-40]. Non-monotonic motion is problematic for control over actuator position.

Temperature has also been found to play a role in actuation. Actuators operating at elevated temperatures showed greater strain [41, 42] and accelerated creep [43].

Conjugated polymer actuator performance therefore depends not only on the synthesis medium, but also on the medium in which it is employed. Because the roles of the electrolyte and the temperature are not yet fully understood, new operation conditions must be characterized in terms of critical performance characteristics such as actuation strain, actuation stress (or, in the case of bending bilayers, moment), and speed. In this chapter actuation strain is characterized. Some information on speed has been included in the Supporting Information.

2.1.2 Actuation in cerebral physiological ion concentrations and temperature

The prior demonstrations of biomedical applications [2-6] did not characterize actuation strain or deflection in those media. PPy(DBS) actuation has, however, been tested in several ionic solutions and temperature ranges. The majority of these studies have been done by systematically cycling one cation at a time [41, 44, 45] or by cycling in a solution with a single anion and cation, such as NaCl [46, 47]. PPy(DBS) has not yet been characterized in the ionic mixture and temperature found in the brain. For the long-term goal of producing movable neural interfaces, performance in cerebrospinal fluid (CSF) at body temperature needs to be determined. Ion concentrations in CSF are listed in Table 1-1. The primary constituents are Na^+ and Cl^- . CSF also contains glucose, proteins (430 mg/L), and lymphocytes ($< 4 \mu\text{m}^3$), and it is maintained at a pH of 7.31 [48, 49]. Artificial cerebrospinal fluid (aCSF) is used in lab settings to match the electrolyte concentrations of CSF, but it lacks the other components. This study examined the effects of the mixed ionic components of CSF on actuation, but future work will need to examine the effects of the other components, also.

Table 2-1. Ionic components of artificial cerebrospinal fluid [48].

CSF Ionic Component		Hydrated Radius (pm) [27]	Concentration (mM)
Sodium	Na^+	450	135-150
Chlorine	Cl^-	300	115-130
Potassium	K^+	300	2.6-3.0
Calcium	Ca^{2+}	600	1.0-1.4
Magnesium	Mg^{2+}	800	1.2-1.5
Phosphate	* PO_4^{3-}	400	0.4-0.6

* The charge depends on pH, going from PO_4^{3-} at high pH to H_3PO_4 at low pH.

2.2 Methods

2.2.1 Bilayer beam actuator fabrication

Devices were fabricated using standard photolithography techniques (Lurie Nanofabrication Facility, University of Michigan). They consisted of a PPy/Au bilayer on a Parylene substrate, with no probe electrode. Photoresist (Shipley 1813, AZ Electronic Materials) was spin-coated onto a 4" silicon wafer and baked at 95 °C for 90 minutes to serve as a final release layer. Parylene C was deposited over the resist ($12.9 \pm 0.8 \mu\text{m}$, PDS 2035, Specialty Coating Systems), and after an oxygen plasma clean (PlasmaTherm 790, 150 mT, 99 sccm O₂, 100 W, 30 sec), chromium (Cr, 150 Å) and gold (Au, 1500 Å) were evaporated (Enerjet Evaporator, 2×10^{-6} T, 10 Å/sec) onto the Parylene. A second layer of photoresist was deposited and patterned using a Cr/glass mask to define the (identical) metal and beam shapes. The metal layers were patterned by wet etching (Transene TFA Au etchant, CR-14 Cr etchant). The Parylene was dry etched using an oxygen plasma (conditions as above, 200 nm/min etch rate), employing the resist and the metal as a mask. The beams were released by soaking the wafers in acetone, thereby dissolving the first resist layer. They were $13.1 \pm 0.8 \mu\text{m}$ thick, 10 mm long, and 0.5 mm wide. The beams were rinsed in isopropanol and water and allowed to air dry before use.

PPy(DBS) was polymerized galvanostatically (at constant current) to a thickness of $11.3 \pm 0.8 \mu\text{m}$ onto the Au surface in a solution of 0.1 M pyrrole (Aldrich) and 0.1 M NaDBS (Aldrich) in deionized (DI) water using a galvanostat/potentiostat (Ecochemie Autolab PGStat 12). The deposition current density was 1 mA/cm². (Polymerizing at higher currents has been shown to reduce actuation strain [50-52].) A porous carbon counter

electrode and Ag/AgCl reference electrode (Bioanalytical Systems Inc.) were used during polymerization. Samples were rinsed in DI water and allowed to dry at ambient conditions for at least 24 hours. Parylene and PPy thicknesses were measured using scanning electron microscopy (SEM) images (Philips XL30ESEM, 5 kV) of beam cross-sections. Bilayer devices were stored in closed Petri dishes lined with cleanroom paper wipes.

2.2.2 Actuator cycling

Electrochemical cycling took place in four conditions: in 0.15 M NaDBS or in aCSF (see Table 1-1) at either 22 or 37 °C. The counter electrode was a 1x1” platinum foil and the reference electrode was a dedicated Ag/AgCl reference electrode used only for cycling. The counter and reference electrodes were rinsed in water between different solutions.

The positive charge density (C/m^3) consumed during oxidation was found by integrating the current over the time of the forward sweep from -1.0 V to +0.4 V and dividing by the measured PPy volume; the negative charge density during reduction was found analogously, and the total charge density was taken as the sum of the absolute values. (I.e., energy recovery was not considered.)

2.2.3 Beam tip deflection, curvature, and actuation strain

Digital video of bilayer actuation was recorded through a microscope (Leica, 10x zoom) at 30 frames per second (Pinnacle Dazzle DVC 100 digital video recorder). Image frames were extracted from the video and sampled every 10 frames, resulting in 3 frames

per second (Quicktime 7 Pro, Apple Inc.). Device dimensions were used for image size calibration. Positional resolution was 22 $\mu\text{m}/\text{pixel}$.

Three frames are shown overlaid in Figure 2-2 from a bilayer beam in the fully oxidized and reduced (neutral) states and in the intermediate straight position that was used as a reference. The beam appears to be thicker in the deflected states because it twisted slightly. (For clarification, “reduced” in this context means held at -1.0 V, determined experimentally to be sufficient to produce the maximum deflection during these cycles; the actual oxidation level is unknown. Likewise, “fully oxidized” means an applied voltage of +0.4 V.)

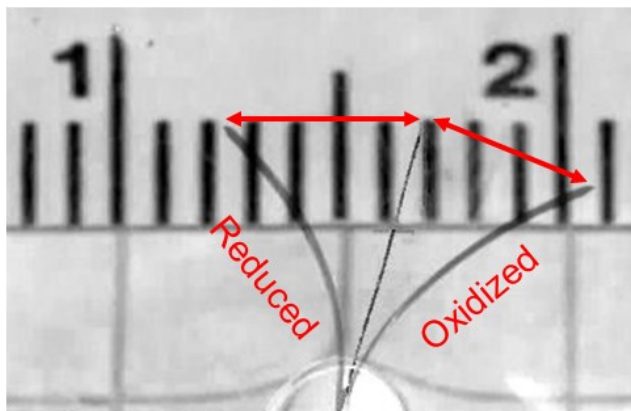


Figure 2-2. Three superimposed images of beam deflection upon reduction, oxidation, and transitioning midway (overhead view with the face of the beam perpendicular to the page). The ruler scale is in cm. The center position illustrates the zero curvature reference point that was used to determine tip deflections, and the arrows drawn over the image indicate the magnitude of the tip deflection.

Image processing was performed on still frames from the video to isolate the beam from the background (ImageJ software, NIH). An edge-detection algorithm written for this application (Matlab, Mathworks) was used to track the deflection δ of the tip of the beam. The recorded times from the video and the galvanostat were used to synchronize the cyclic voltammetry (CV) cycles with the deflection. The zero-curvature inflection points

were obtained from the frames with the straightest beams. Beam curvature κ was calculated from measured tip deflections without assuming small deflections, as described in the Supporting Information.

$$(4) \quad \kappa = \frac{2\Delta x}{(L - \Delta y)^2 + \Delta x^2}$$

The actuation strain α_{PPy} was calculated from the curvature κ [33, 53, 54]:

$$(5) \quad \kappa = \frac{\alpha_{PPy}}{h_{sub}} \frac{6mn(1+m)}{1 + 4mn + 6m^2n + 4m^3n + m^4n^2}$$

where h_{sub} is the substrate thickness, m is the PPy to substrate thickness ratio (h_{PPy} / h_{sub}), and n is the ratio of the Young's moduli (E_{PPy} / E_{sub}). An effective E_{sub} was calculated from the combined substrate layers (see the Supporting Information). The Young's modulus of PPy(DBS) has been shown to change from 200 MPa in the reduced state to 450 MPa in the oxidized state [23]. Therefore, the oxidized state E_{PPy} was used to find the strain from the curved state (PPy side in) and the reduced state E_{PPy} was used to find the strain from the backwards-bending curvature. The two strains were summed to determine the effective actuation strain between the oxidized and reduced states.

2.2.4 Electrochemical break-in

The as-deposited PPy(DBS) is compact, and it typically takes several cycles for the structure to open fully to accommodate ion ingress [37, 55], particularly for thick films. Therefore, the bilayer beams were "primed" by performing ten cyclic voltammograms (CV cycles), ramping the voltage between +0.4 V and -1.0 V at 10 mV/s at room temperature (RT, ~22 °C) in 0.15 M NaDBS. The scan rate of 10 mV/s was chosen to

enable observation of the shapes and positions of the oxidation and reduction peaks in the CV [29], and to compare the results to prior work.

2.2.5 Scanning electron microscopy and elemental analysis

After cycling, the polymer was taken to 0 V (oxidized) before switching off the voltage. Samples were rinsed in DI water and allowed to dry in air at room temperature for at least 24 hours. The final 5 mm section at the tip of the bilayer was cut off using a razor blade and adhered to a sample holder with double-sided copper/nickel adhesive tape. SEM images were obtained (Philips XL30ESEM, 5 kV) and the ions in the PPy were identified using energy dispersive x-ray analysis (Phoenix XEDS EDX, EDAX Inc.) with a 20 kV accelerating voltage. The spectra were normalized by the maximum intensity sulfur peak, and the resulting profiles were compared (Spectrum View v4.0, EDAX Inc.).

2.3 Results and Discussion

2.3.1 Deflection during cyclic voltammetry in NaDBS at room temperature

The cycling behavior of PPy(DBS) in aqueous NaDBS at room temperature was used as a baseline because this polymer has previously been characterized in this electrolyte [23, 56]. Since the DBS⁻ is not exchanged, only the Na⁺ contributes to the volume change [36, 57], causing an expansion (and thus bilayer bending PPy-side out) during reduction as the hydrated Na⁺ enters the polymer and a contraction (bending PPy-side in) during oxidation as the hydrated Na⁺ leaves the polymer. (OH⁻ in the solution also enters and exits the polymer, but it does not contribute to actuation [58].)

Twelve bilayer devices were initially cycled ten times (cycles 1-10) in NaDBS at RT from +0.4 V to -1.0 V vs Ag/AgCl at 10 mV/s to bring them all to the same starting

condition. (The samples were “primed”.) The NaDBS concentration was 0.15 M, matching the cation concentration in CSF. Sample-to-sample variation in the bending of these nominally identical samples is shown in the Supporting Information.

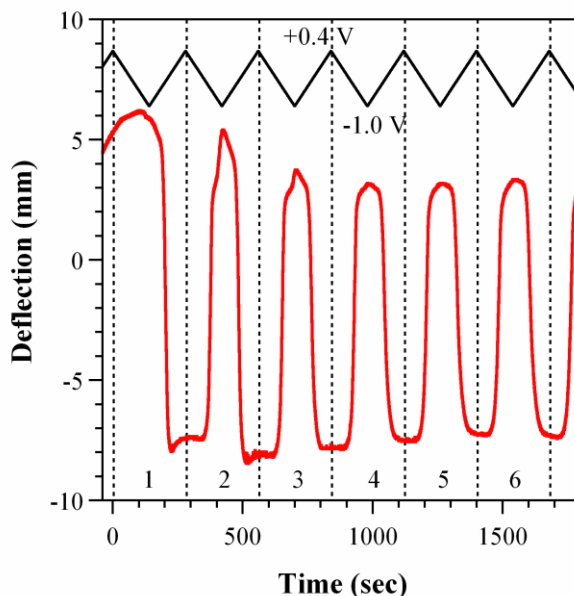


Figure 2-3. Deflection vs. time (lower red curve) during the first 6 cycles (numbered) of a bilayer in NaDBS at room temperature. The voltage was scanned at 10 mV/sec between +0.4 and -1.0 V vs Ag/AgCl, as illustrated at the top (black curve). Positive deflection indicates PPy expansion (bending PPy-side out), and negative deflection indicates PPy contraction (PPy-side in).

Figure 2-3 shows the deflection versus time of one of the bilayers during the initial cycling in NaDBS at RT. The samples began (at $t = -40$ sec) curved with the PPy side out (bending “backwards”). This curvature is not seen in thinner films of $1 \mu\text{m}$ [59], but is consistently observed in bilayers with thicker PPy films. During the initial increase in potential from 0 to +0.4 V (to the left of the first dashed vertical line), the deflection increased somewhat, indicating a small expansion of the PPy. The gradual increase in deflection continued upon scan reversal to the reduced state at -1.0 V ($t = 150$ sec). Such a lack of significant bilayer movement during the first reduction scan, despite the influx

of Na^+ , is typical of PPy(DBS) [58, 60], which expands out-of-plane at this time [61]. Upon re-oxidation (going from -1.0 to +0.4 V), the PPy contracted strongly inplane as the Na^+ was expelled, reversing the direction of bending so that the PPy faced in (shown by negative numbers on the axis), passing through a point at which the bilayer was flat. Thereafter, the second reduction led to an expansion back to nearly the original position. The deflection versus time curves stabilized after the third or fourth cycle. This behavior is consistent with prior work, in terms of general behavior and the number of cycles required for “break in” (or priming or conditioning).

2.3.2 Cyclic voltammograms under four conditions

Immediately after the priming step, the samples were split into four groups of three samples each and cycled ten times (cycles 11-20) as before but in either (1) NaDBS at room temperature (NaDBS at RT), (2) NaDBS at body temperature (NaDBS at 37 °C), (3) the physiological electrolyte at room temperature (aCSF at RT), or (4) the physiological electrolyte at body temperature (aCSF at 37 °C). The cyclic voltammograms (CVs) and the associated deflections during scan 19 in the four solutions are shown for representative samples in Figure 2-4. (Scan 20 concluded at 0 V, so to compare the deflection and charge consumed with scans ending at full oxidation (0.4 V), scans 9 and 19 were taken as representative of the steady state. The CVs for all 20 scans of all 12 samples are shown in the Supporting Information.)

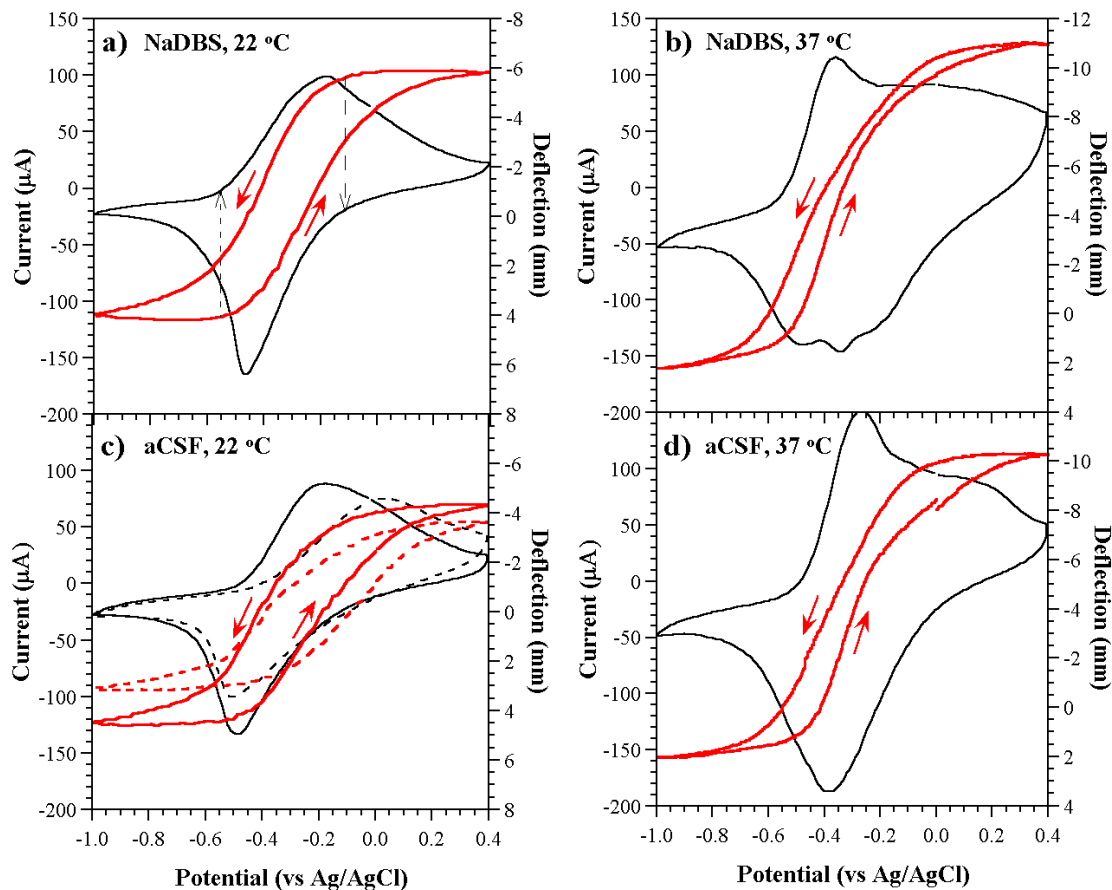


Figure 2-4. Current (black line) and displacement (thicker red line) as a function of potential during the 19th CV scan at 10 mV/s under four conditions. The direction of the scan for the displacement curves is indicated by arrows; note that this axis has been reversed to facilitate comparison with the current. The deflection axis is shifted in (b) and (d) relative to (a) and (c), but has the same amplitude (16 mm). The dashed lines in (c) show results from a second sample.

The CV for NaDBS at RT (Figure 2-4a, the control) was as expected from prior work [29], with a reduction peak near -0.45 V and an oxidation peak at -0.15 V with a shoulder visible near -0.35 V. Table 2-2 shows average values for the three samples in each group of the exchanged charge in both the priming step and, as ratios, in the subsequent cycling under the four conditions. (Values for all groups of samples during scans 9 and 19 are included in the Supporting Information.) Comparing the average charge densities consumed by these samples during cycle 19 compared to cycle 9 (Table 2-2, data line 6),

there was a 9% increase. Variations between samples were of similar magnitude, so this is not considered to be significant.

Table 2-2. Values of average actuation strain α , exchanged charge density, and strain-to-charge density in the 9th scan in NaDBS (12 samples) and average ratios of the 19th to the 9th scans under different cycling conditions (n = 3 unless otherwise noted).

Measurements	Values in NaDBS, Scan 9		Ratio of Scans 19/9							
			NaDBS				aCSF			
			RT		37C		RT		37C	
α Reduction	0.37		1.09 ± 0.43	0.58 ± 0.09	0.86 ± 0.33	0.40 ± 0.28				
α Oxidation	-0.36	%	0.93 ± 0.42	1.53 ± 0.18	0.93 ± 0.31	1.28 ± 0.22				
α Total	0.73		1.02 ± 0.40	1.13 ± 0.09	0.89 ± 0.32	0.94 ± 0.19				
Re Charge Density	-98±14*10 ⁶	C/m ³	1.11 ± 0.18	1.78 ± 0.42	1.02 ± 0.20	1.68 *				
Ox Charge Density	79±11*10 ⁶		1.06 ± 0.21	1.56 ± 0.26	1.01 ± 0.19	1.71 *				
Total Charge Density	178±24*10 ⁶		1.09 ± 0.18	1.66 ± 0.30	1.02 ± 0.23	1.70 *				
Re α / Charge Density	38 ± 14 * 10 ⁻¹²	%/ (C/m ³)	0.99 ± 0.42	0.33 ± 0.09	0.84 ± 0.36	0.24 ± 0.17				
Ox α / Charge Density	45 ± 14 * 10 ⁻¹²		0.87 ± 0.43	0.98 ± 0.20	0.92 ± 0.35	0.75 ± 0.13				
Tot α / Charge Density	41 ± 14 * 10 ⁻¹²		0.94 ± 0.40	0.68 ± 0.13	0.87 ± 0.37	0.55 ± 0.11				

(*) Denotes data from one sample.

At 37 °C, the CVs of the devices cycled in NaDBS changed significantly (Figure 2-4b). There was now a large oxidation peak at -0.35 V (the position at which the shoulder had been at RT), and a second broad oxidation peak appeared that was centered around +0.1 V; there was no clear peak at -0.15 V. In addition, two more reduction peaks appeared to the right of the peak at -0.45 V, at -0.35 V and -0.25 V. The area bounded by the CV was significantly larger: the exchanged charge density was 66% greater when cycling at 37 °C than at RT.

The CVs in aCSF at RT (Figure 2-4c) varied in their oxidation peak positions among the three samples, so two examples are shown. In general, the CVs were similar to those in NaDBS at RT, but the reduction peak was shifted slightly (30 mV) cathodically (i.e., to

the left), and the oxidation peak was shifted anodically (to the right) in two cases but not the third. The total exchanged charge density was virtually the same as in NaDBS at RT.

Upon increasing the temperature in aCSF (Figure 2-4d), the changes in the oxidation current mirrored those in NaDBS at 37 °C (Figure 2-4b), and again the position of the large peak was shifted anodically relative to the one in NaDBS at 37 °C. The two satellite peaks during reduction were not present, however. (The CVs are overlaid for ease of comparison in the Supporting Information.) The total exchanged charge density again increased compared to aCSF at RT, by a similar factor (70%) as seen in NaDBS.

2.3.3 Actuation strains during CVs

Given the significant changes in the CVs, the important question was whether there were similar significant changes in actuation strain. In PPy(ClO₄) more exchanged charge is associated with greater strain, until a degradation point [62, 63], but in PPy(DBS) currents can flow that are not associated with volume change [64]. Returning again to Figure 2-4a but this time examining the associated deflection, the contraction of the PPy (note the reversed right axis) began simultaneously with the onset of the oxidation current (shown by the dotted black arrow on the left), slowing down after the peak as the current dropped but continuing to +0.4 V. Expansion was also concurrent with the flow of charge during reduction (dashed black arrow) and continued all the way to -1.0 V.

As shown in Table 2-2 (data line 3, column 1), the average net strain (found using equation (4) from the displacements) in NaDBS at RT was only 0.7%, substantially less than the previously reported ~3% [23, 33, 35]. The reasons for this are unclear. The maximum voltages experienced during deposition were below +0.55 V vs. Ag/AgCl, so

the PPy films were not over-oxidized. Samples were examined by SEM at cross-sections midway through the beams, and beams demonstrating delamination were excluded from the analysis. However, partial delamination cannot be ruled out; this would have reduced the curvature since only part of the PPy film would have contributed to actuation. PPy films in contact with a conductor along their entire area have been shown to produce a force density six-fold greater than isolated films [12]. There is some evidence for delamination in the CVs shown in the Supporting Information, in which the currents steadily decrease in each cycle and the peak positions shift.

The ratio of the strain to the charge density was on the order of $0.4 \cdot 10^{-10} \% / (C/m^3)$. Previous values (at RT) were 3x as high for PPy(tetraethylammonium hexafluorophosphate) at $1.2-1.4 \cdot 10^{-10} \% / (C/m^3)$ (electro-polymerized, cycled in propylene carbonate) [65, 66] and two orders of magnitude higher for PPy(sodium benzenesulfonate) at $30 \cdot 10^{-10} \% / (C/m^3)$ (films purchased from BASF, cycled in acetonitrile) [67, 68].

As it should have, the average net strain remained effectively unchanged from cycle 9 to cycle 19 in NaDBS at RT (2% increase - Table 2-2, line 3, column 2), although there was a small shift in the position; this is discussed in more detail below. The average consumed charge increased by 9%, leading to a somewhat smaller strain to charge ratio (6% decrease). These variations provide context for interpreting the magnitude of changes under the other cycling conditions, since nominally the conditions were unchanged here from the priming conditions: variations of this size should not be considered meaningful, but due to experimental variations.

The overall actuation behavior in aCSF at RT (Figure 2-4c) could be described in the same way as in NaDBS. The actuation strain decreased somewhat (-11% relative to scan 9 for this group of devices in NaDBS) while the current density was unchanged, resulting in a correspondingly smaller strain to charge ratio. Most importantly, there was no reversal in the direction of movement despite the anions in this solution, and no significant loss of strain over time due to the divalent cations.

Despite the substantial changes in the CVs when the temperature was raised to 37 °C in NaDBS, the actuation strain varied relatively little from that at RT, increasing by a factor of 1.13 on average. (The particular sample in Figure 2-4b increased much more; the other two pairs of curves are shown in the Supporting Information.) Because of the large increase in the consumed charge (66%), the strain to charge ratio dropped to 0.68 of the value at RT. At elevated temperatures, the actuators were thus less efficient in converting electrical energy to mechanical energy. There was also a large shift of several mm in the positions of the deflections (equilibrium bending angle), as seen by comparing the values of the deflection axis limits in Figure 2-4a and c. This behavior is further discussed below and needs to be taken into account in designing actuators for use at body temperature. The new oxidation peak at +0.1/0.2 V did not contribute significantly to the volume change, and again there was no reversal in the direction of movement even though the oxidation process corresponding to that peak has previously been correlated with anion ingress [22]. It is not clear why there is a new oxidation peak unassociated with bilayer motion at 37 °C, and this should be the topic of future investigation.

In aCSF, although 67% more charge was exchanged at 37 °C than at 22 °C, the net strain only increased by 6% on average, reducing the strain to charge density. These results mirrored those in heated NaDBS. Again, there was a shift in the average bending angle.

These experiments show that these actuators behave substantially the same under physiological settings as in NaDBS, with the movement monotonically increasing/decreasing with voltage at these scan rates. Monotonic behavior is important for actuator control, and was a welcome surprise because the presence of Cl⁻ anions has previously been reported to result in tip deflection in one direction as the cations exit followed shortly thereafter by deflection in the opposite direction as anions enter [22, 69].

2.3.4 Maximum deflection during CVs

As mentioned previously, there were shifts in the average bending angle for the four experimental groups relative to the baseline primed condition. Figure 2-5 shows the maximum deflections during oxidation and reduction of one representative bilayer in each group of three under each of the four conditions over all twenty CV cycles. (The behavior of the three beams in each set was similar, as demonstrated in the Supporting Information.)

As discussed for Figure 2-3, during the first several cycles the magnitude of the deflection in both directions decreased, but then it then stabilized. The curves for bilayers that continued cycling in NaDBS at RT (open blue circles) leveled out to show no further change over time. Those cycled in aCSF at RT (filled blue circles) experienced an immediate small decrease in total peak-to-peak deflection (8% on

average), and thereafter the deflections remained constant (leveling off at a 10% average decrease).

The changes with temperature were larger, as also reflected in Figure 2-4. Samples cycled at 37 °C (red triangular points) in both aCSF (filled symbols) and NaDBS (open symbols), showed a contraction of the PPy, with both positive and negative deflections shifting relative to the previous cycles; this likely reflects a structural change in the polymer. Deflection during oxidation was more strongly shifted, resulting in an overall *net increase* in the range of motion by ~2.5 mm. These results are consistent with previously observed increased strain at higher temperatures [41, 42].

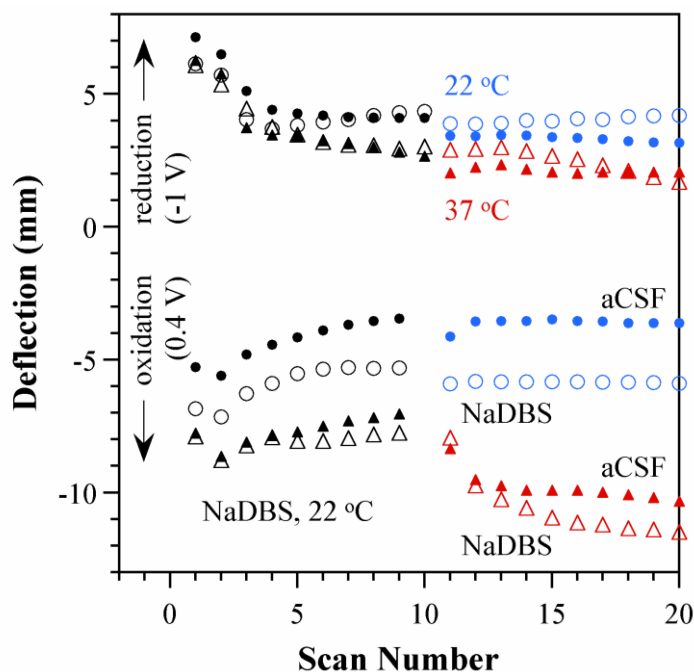


Figure 2-5. a) Maximum deflection of representative bilayers during oxidation and reduction during cyclic voltammetry as a function of cycle number. **Black symbols:** actuation in NaDBS at room temperature (all samples during cycles 1-10). **Filled symbols:** actuation in aCSF during cycles 11-20; **open symbols:** actuation in NaDBS; **red triangle symbols,** actuation at 37 °C during cycles 11-20; **blue circle symbols,** actuation at room temperature.

2.3.5 Elemental analysis

To shed light on the actuation changes noted above, energy-dispersive x-ray spectroscopy (EDX) was performed. There were small variations among the three samples under each condition, so the spectra were averaged. Figure 2-6 shows the average EDX spectra from the samples that had been cycled in NaDBS at RT and from those cycled in aCSF at 37 °C. The spectra were normalized to the sulfur (S) peak; results were virtually identical using the carbon (C) peak. A nickel peak (at 8.26 keV, not shown) indicated that the beam penetrated the entire thickness of the sample.

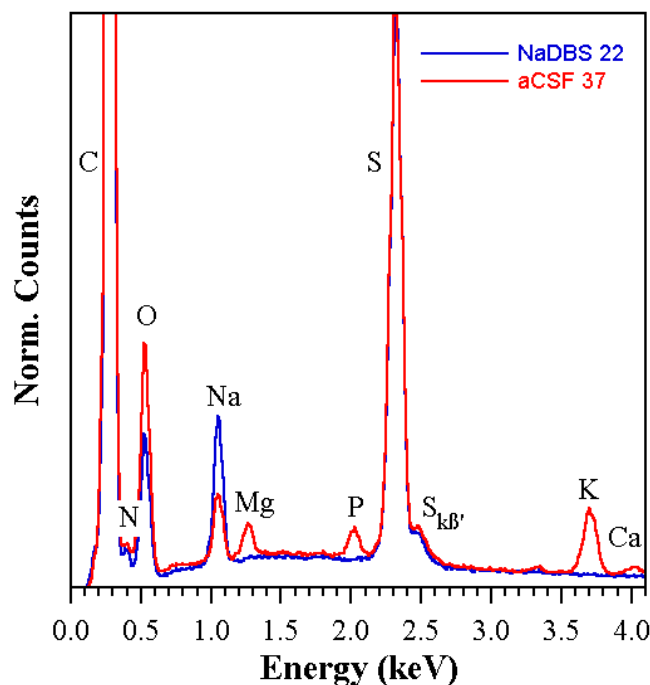


Figure 2-6. EDX spectra of samples cycled in NaDBS at 22 °C and in aCSF at 37 °C, normalized to the S peak.

The sample cycled in NaDBS contained carbon (C) from the PPy and the DBS, nitrogen (N) from the PPy, and oxygen (O) and sulfur (S) from the DBS. It also contained sodium (Na) from the electrolyte. Recall that the sample was taken to the oxidized state before removing it from the electrochemical cell, so this reflects Na⁺ that is deeply trapped in the

film (presumably with the associated water). A small $S_{k\beta'}$ shift peak, an indication of the S oxidation state, is also visible to the right of the S peak [70]. The sample cycled in aCSF contained the same species, but it also showed magnesium (Mg), calcium (Ca), potassium (K), phosphorous (P), and additional oxygen (O) (the latter two from the PO_4) incorporated into the polymer during cycling. There was no Cl in these samples (k_α 2.622, k_β 2.815 eV) (although trace amounts in two samples were found in a previous study [71]).

EDX is not quantitative without comparison to a reference sample with a similar composition. Furthermore, the areas under EDX peaks for *different* species cannot be used to obtain relative concentrations, so these spectra can only be used to compare relative amounts of the same element. The area under the Na peak for the sample cycled in aCSF was 68% of the size for the sample cycled in NaDBS (72% if normalizing to the C peak instead of the S peak), so one can hypothesize that a third less Na^+ was exchanged during cycling in aCSF. (This conclusion assumes that if there was any loss of Na^+ during sample rinsing and drying, it occurred in the same proportion in both solutions.)

The difference in compensating charge was made up by the other cations. Given their low concentration in aCSF (Table 1-1), one can conclude that the PPy affinity for K^+ , Ca^{2+} , and Mg^{2+} is higher than for Na^+ . Previously it has been shown that K^+ produces smaller strains than Na^+ [44] (K^+ has a smaller hydration shell), so the decrease in deflection in aCSF may be partly due to its exchange. As mentioned above, divalent cations interact more strongly with the PPy chains and thus have greater difficulty exiting

the polymer, resulting in less polymer expansion, so one might speculate that the decrease in deflection in aCSF may also be related to that.

In addition, it has been shown that in solutions containing small anions, that they are also exchanged during cycling, despite the presence of the immobile DBS⁻ [22, 69]. Interestingly, essentially no Cl⁻ was found in the sample, despite a concentration in aCSF nearly as high as that of Na⁺. Instead, the oxygen peak in the aCSF samples was 60% larger (75% larger if normalizing to the C peak), and with each PO₄ carrying 4 oxygens and each DBS carrying three, one can tentatively conclude that one PO₄ is entering for each two DBSs. This is a surprisingly large amount, given its minute concentration in aCSF (~0.5% that of Cl⁻). Differences in the affinity of PPy(DBS) to different cations is not uncommon, but this difference to the two anions is particularly large. Prior work with PPy(PPS) tested in sodium phosphate buffer showed an anodic peak [46], but in these CVs there were no observable peaks associated with this exchange (compare Figure 2-4a and c). (It is not the peak at +0.1 V, since that also appeared in NaDBS.) The PO₄ molecule is in the form of PO₄³⁻ at high pH, but becomes increasingly protonated as the pH is lowered until it becomes H₃PO₄ in acidic media. (In CSF, which has a pH of 7.3, the proportions would be expected to be 61% HPO₄²⁻ and 39% H₂PO₄⁻.) The local pH at the surface of the polymer is unknown, but the local pH is known to be affected by cycling [58, 72]. Nevertheless, the molecule is an anion, rather than a cation. Again, half a PO₄ per DBS is an enormous amount, and one might have expected that to cause a noticeable reversal in the deflection (Figure 2-4), particularly given that its reported hydrated radius is nearly as large as that of Na⁺ (Table 1-1), but it did not. The prior study with PPy(PPS) in sodium phosphate buffer also showed no volume change [46]. It

is possible that much slower scans may show actuation strain, or that PO_4 has such a small hydration shell in the PPy that it is mechanically “invisible.” Further studies would be required to understand this.

2.4 Conclusions

The bending of bilayer bending beams actuated using PPy(DBS) was characterized under physiological conditions similar to those found in the brain. These conditions were simulated by employing aCSF at 37 °C, which contains a mixture of cations, including two divalent cations, as well as a couple of small anions. The roles of both temperature and of the mix of ions were ascertained by making use of a control solution containing only a single type of cation and no mobile anions (NaDBS) and by comparing bending at 22 °C and 37 °C. As discussed above, divalent ions have been shown to ionically crosslink charged polymers, resulting in difficulties in exchanging these ions and producing smaller strains, posing the concern that device performance would degrade in the aCSF. Another concern arose from the presence of the small anions, which in prior work had been shown to produce a reversal of motion, complicating positional control over devices (as well as reducing net strain).

The actuation strain in aCSF at 22 °C was almost 90% of that in NaDBS, and furthermore it remained monotonic. The exchanged charge was also virtually the same. Thus, neither the divalent cations nor the small anions had a significant negative impact, even though elemental analysis revealed that all the cationic components of aCSF were present in substantial amounts in the PPy after cycling, in addition to a large amount of HPO_4^{2-} and/or H_2PO_4^- (one per 2 DBSs). Interestingly, the ion content in the film did not reflect the solution composition, which had at least 200 times more chlorine than phosphate and

25 times more sodium than all the other cations combined. Temperature exerted a more significant change in behavior. The net strain increased somewhat at 37 °C in both solutions, and the average bending angle shifted noticeably. These effects will need to be taken into account when designing devices for use in the body. The cyclic voltammograms acquired additional peaks and substantially more charge was exchanged, resulting in a lower efficiency in converting electrical to mechanical work. Nevertheless, it is clear that PPy(DBS) can indeed be used for neural interface and neural probe applications.

2.5 Acknowledgments

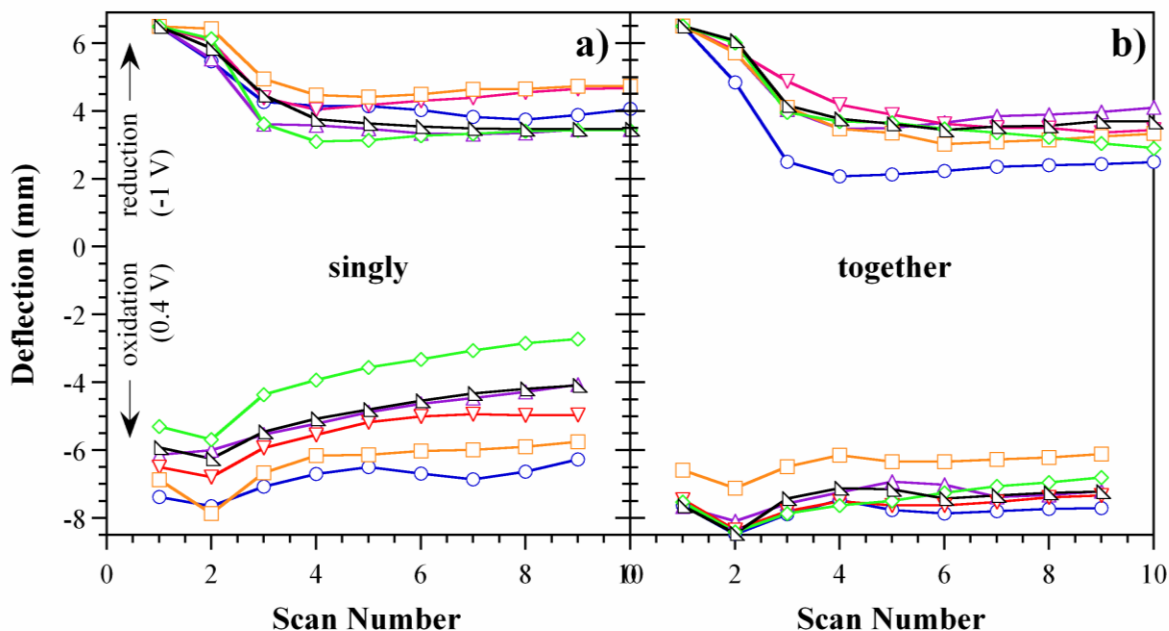
This work was supported by the Center for Neural Communication Technology is a P41 Resource Center funded by the National Institute of Biomedical Imaging and Bioengineering (NIBIB, P41 EB002030) and supported by the National Institutes of Health (NIH).

2.6 Supporting Information

Supporting information includes cyclic voltammetry and deflection of all twelve bilayers under all four conditions, peak to peak deflections for the samples, variation among samples, deflection upon voltage stepping, transient effects upon voltage stepping, ramping voltage to attenuate initial transient effects, calculation of curvature and actuation strain from deflection measurements, and cross-sectional images showing delamination in some devices.

2.6.1 Variation among samples

In order to explore the extent of sample-to-sample variation under nominally identical electrodeposition and cycling conditions, six samples (the ones in Section 2.3.1 that were subsequently cycled at room temperature) that had been polymerized one at a time on the same day were compared with six samples (the ones in Section 2.3.1 that were later cycled at 37 °C) that had been polymerized simultaneously on another day. The same current density was used in all cases (1 mA/cm²).



Sup. Figure 2-1. Maximum deflection during oxidation and reduction in NaDBS at 22 °C as a function of cycle number. a) Six bilayers on which the PPy(DBS) was polymerized separately (one bilayer at a time). b) Six bilayers on which the PPy(DBS) was polymerized simultaneously.

Sup. Figure 2-1 shows the variation in maximum deflections for both sets of samples during the first 10 cycles in room temperature NaDBS. The initial deflections in the reduced state varied, with an average of 6.5 mm and a standard deviation of 0.6 mm. In

order to facilitate comparison, all the deflection data in Sup. Figure 2-1 were shifted so that the starting reduction position was the same, 6.5 mm.

The (shifted) average deflection during reduction in scan 10 was $4.0 \text{ mm} \pm 0.6 \text{ mm}$ for the films deposited separately and $3.3 \text{ mm} \pm 0.6 \text{ mm}$ for the PPy deposited simultaneously. The second set drifted somewhat further from the starting position, on average. The *variation* in the final reduced positions was the same $\pm 0.6 \text{ mm}$ for all twelve beams, however.

During oxidation the bilayers made together deflected more than those made individually and showed less variation in the oxidized-state starting positions: in scan 1 the average was $-6.3 \text{ mm} \pm 0.7 \text{ mm}$, compared with $-7.4 \text{ mm} \pm 0.4 \text{ mm}$ for the bilayers made together. The variation among bilayer tip positions increased by cycling: at scan 9, the average was $-4.6 \text{ mm} \pm 1.3 \text{ mm}$ for the individually-polymerized beams and for the beams polymerized together it was $-7.1 \text{ mm} \pm 0.6 \text{ mm}$.

These data indicate that there are differences among beams made on the same day, even if they are all made together, and that there is even greater variation if they are made one at a time. Nevertheless, the behavior was broadly similar for all the bilayers, showing a decrease in deflection within the first 4 cycles in both the PPy-side-out and PPy-side-in directions but stabilizing thereafter.

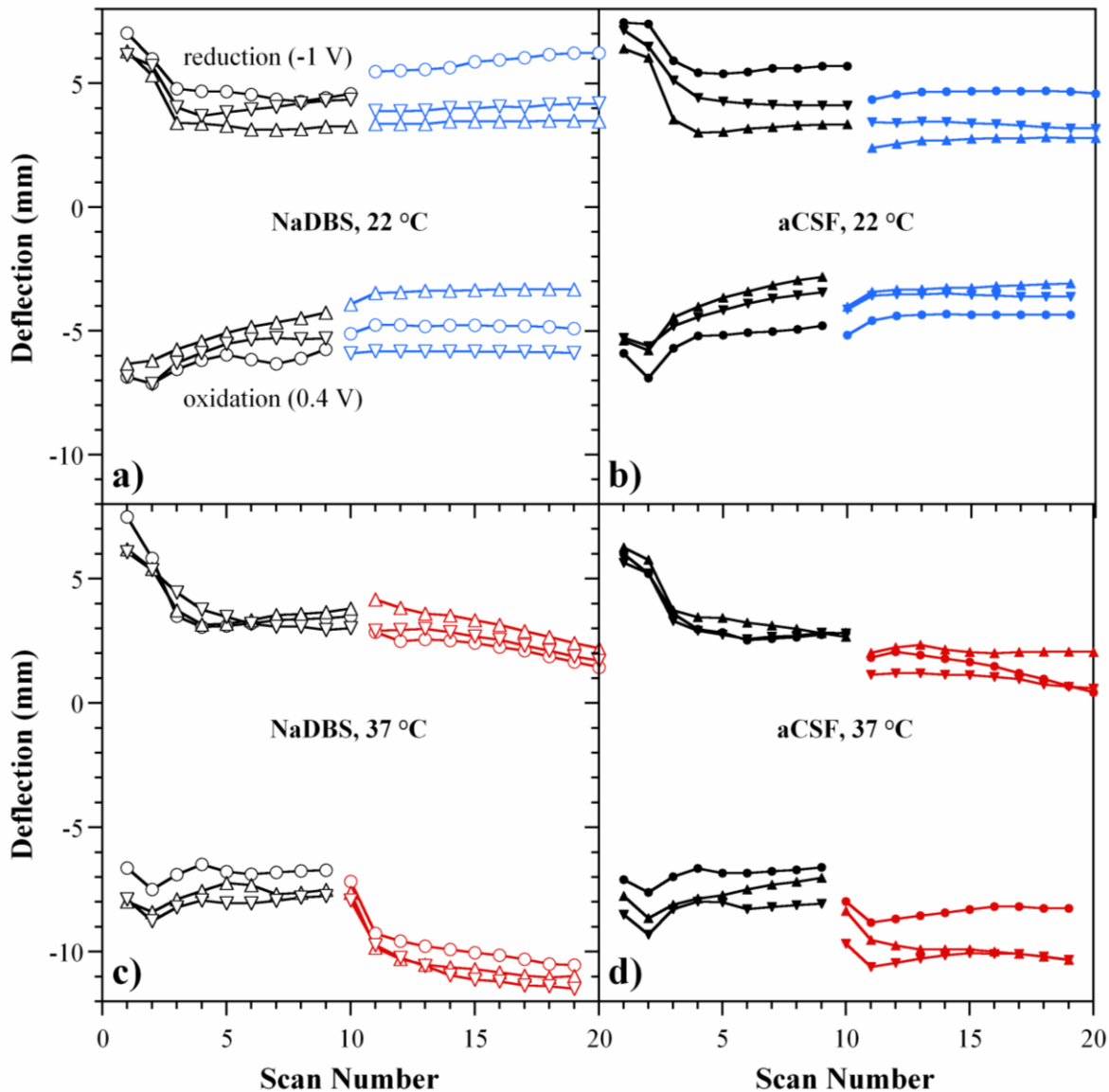
2.6.2 Deflection of all twelve bilayers under all four conditions

The deflections of all the bilayers are shown in Sup. Figure 2-2. The samples used in the main text, Figure 2-5, were: NaDBS, 22 °C: ▼ (sample 2), aCSF, 22 °C: ▼ (sample 2), NaDBS, 37 °C: ▼ (sample 2), aCSF, 37 °C: ▲ (sample 3).

Sup. Table 2-1. Peak to peak deflections for the samples in Figure 2-5 of the main text.

Peak-to-Peak Deflection (mm)				
	NaDBS RT	NaDBS 37 °C	aCSF RT	aCSF 37 °C
Scan 9	9.61	10.70	7.56	9.84
Scan 19	10.03	13.27	6.80	12.26
Deflection Difference from Scan 19 to 9 (mm)				
Scan 19-9	0.42	2.56	-0.76	2.42
Peak-to-Peak Deflection Ratio (Scan 19/9)				
Scan 19/9	1.04	1.24	0.90	1.25

As shown in Figure 2-2 of the main text, during each CV scan the bilayer beam would deflect to a proximal position relative to the straight position during reduction and oxidation. Sup. Table 2-1 shows the net deflections in scans 9 and 19 for the samples shown in Figure 2-5 of the main text. In addition, the differences in displacements between scans 19 and 9 as well as their ratios are also given.

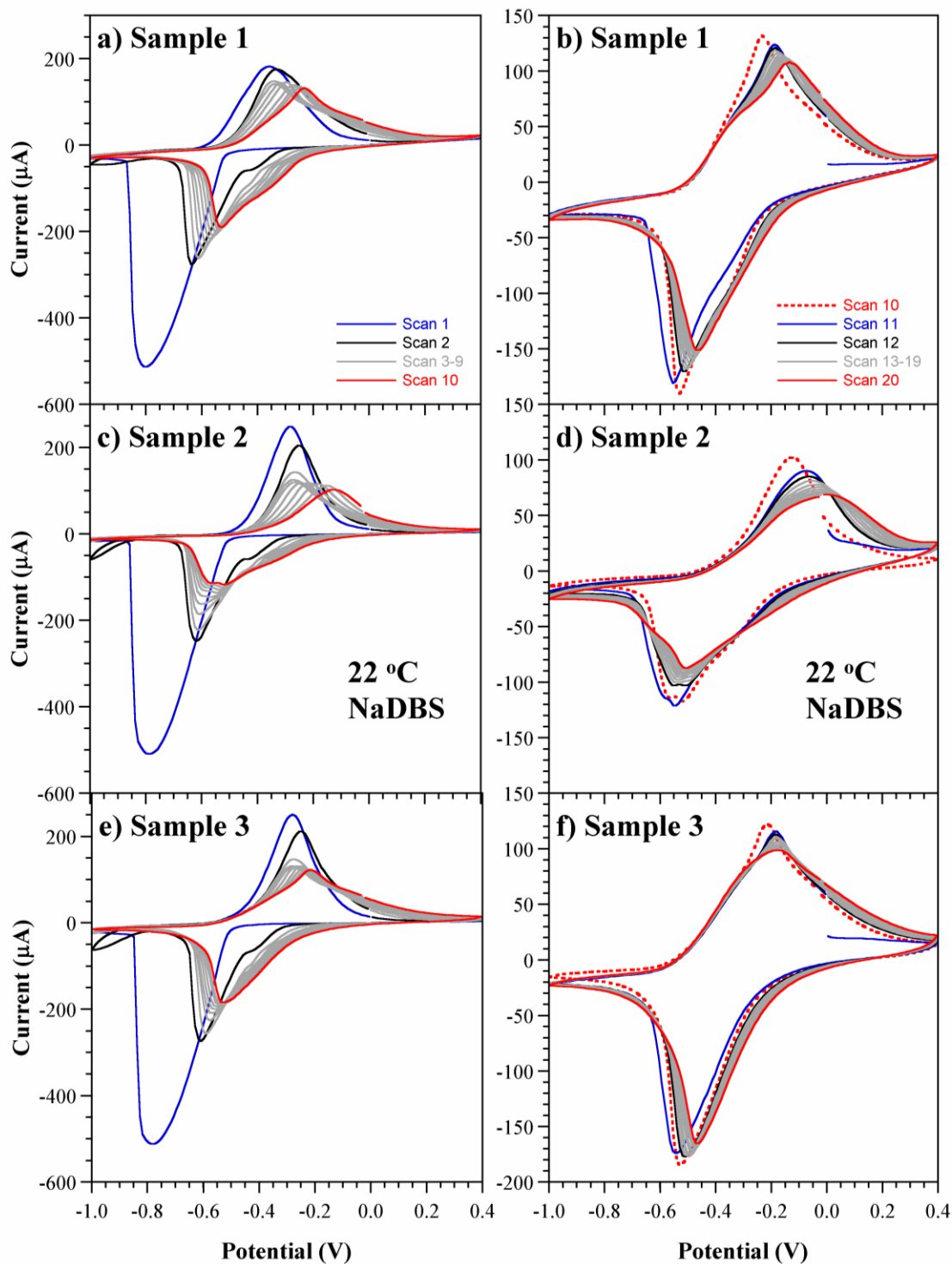


Sup. Figure 2-2. The maximum deflections during cyclic voltammetry of all twelve samples, cycled in NaDBS at 22 °C for the first 10 cycles, then in the medium and at the temperature indicated. (For correlation with Sup. Figure 2-3-Sup. Figure 2-6, circles = sample 1, up-pointing triangles = sample 2, and down-pointing triangles = sample 3.)

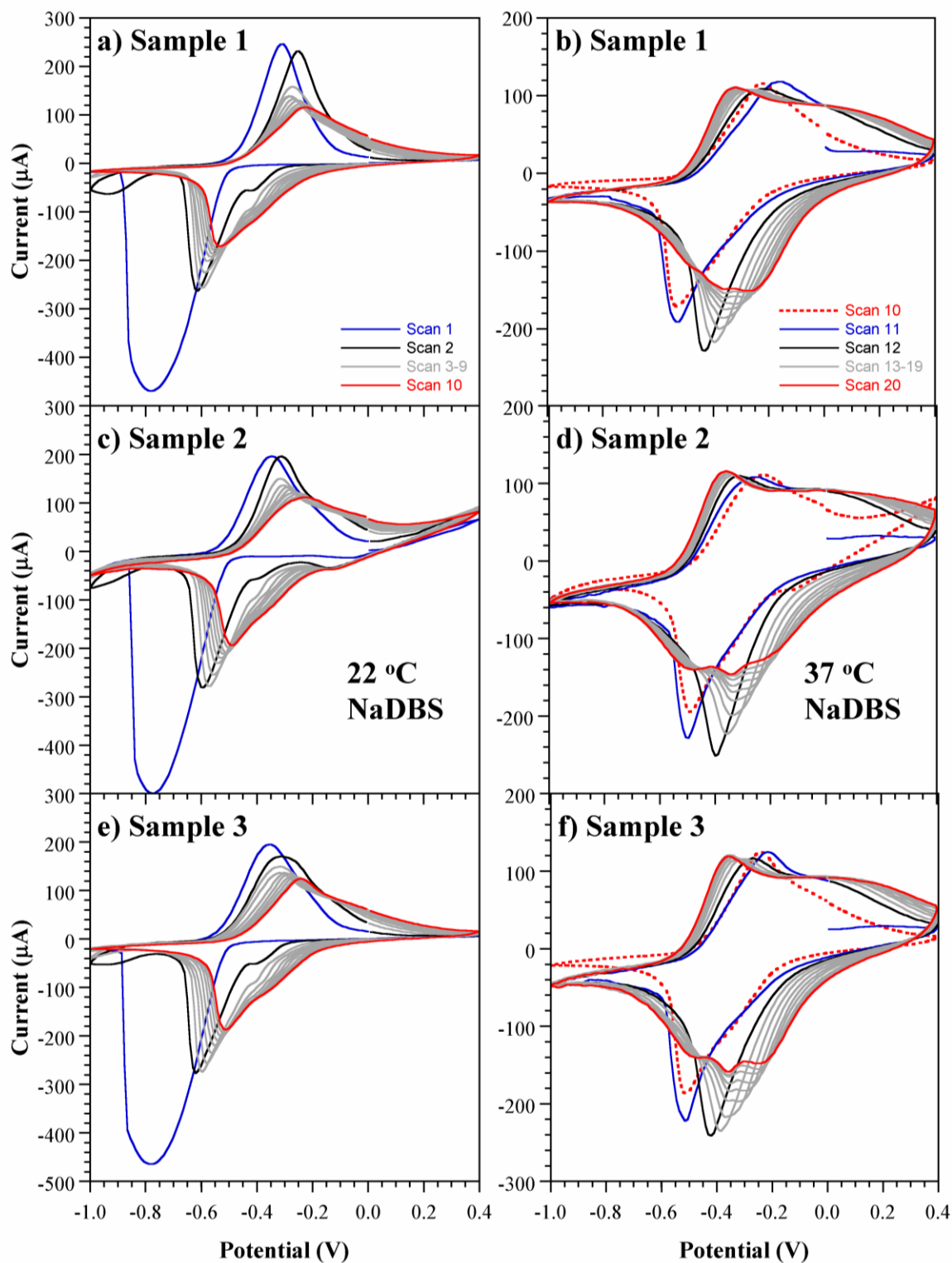
2.6.3 Cyclic voltammetry of bilayers under the four conditions

Figure 2-4 of the main text shows current-voltage relationships of representative samples in each of the four solutions. To illustrate the variability, the cyclic voltammograms (CVs) of all three samples in each of the four solutions are shown in Sup. Figure 2-3-Sup.

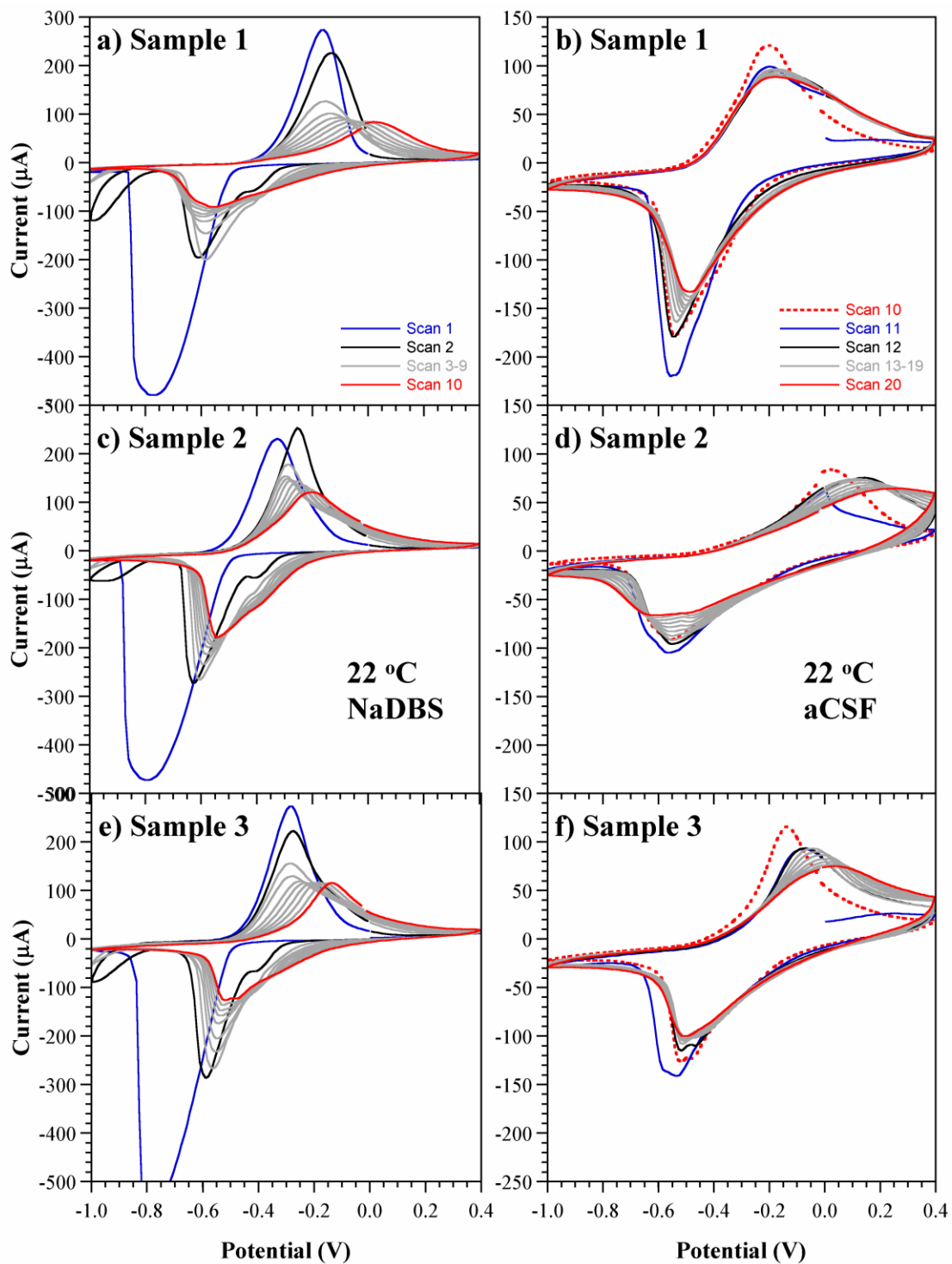
Figure 2-6. PPy(DBS) was galvanostatically (constant current) polymerized to a thickness of $11.3 \pm 0.8 \mu\text{m}$. The scan rate was 10 mV/s, and the reference electrode was Ag/AgCl.



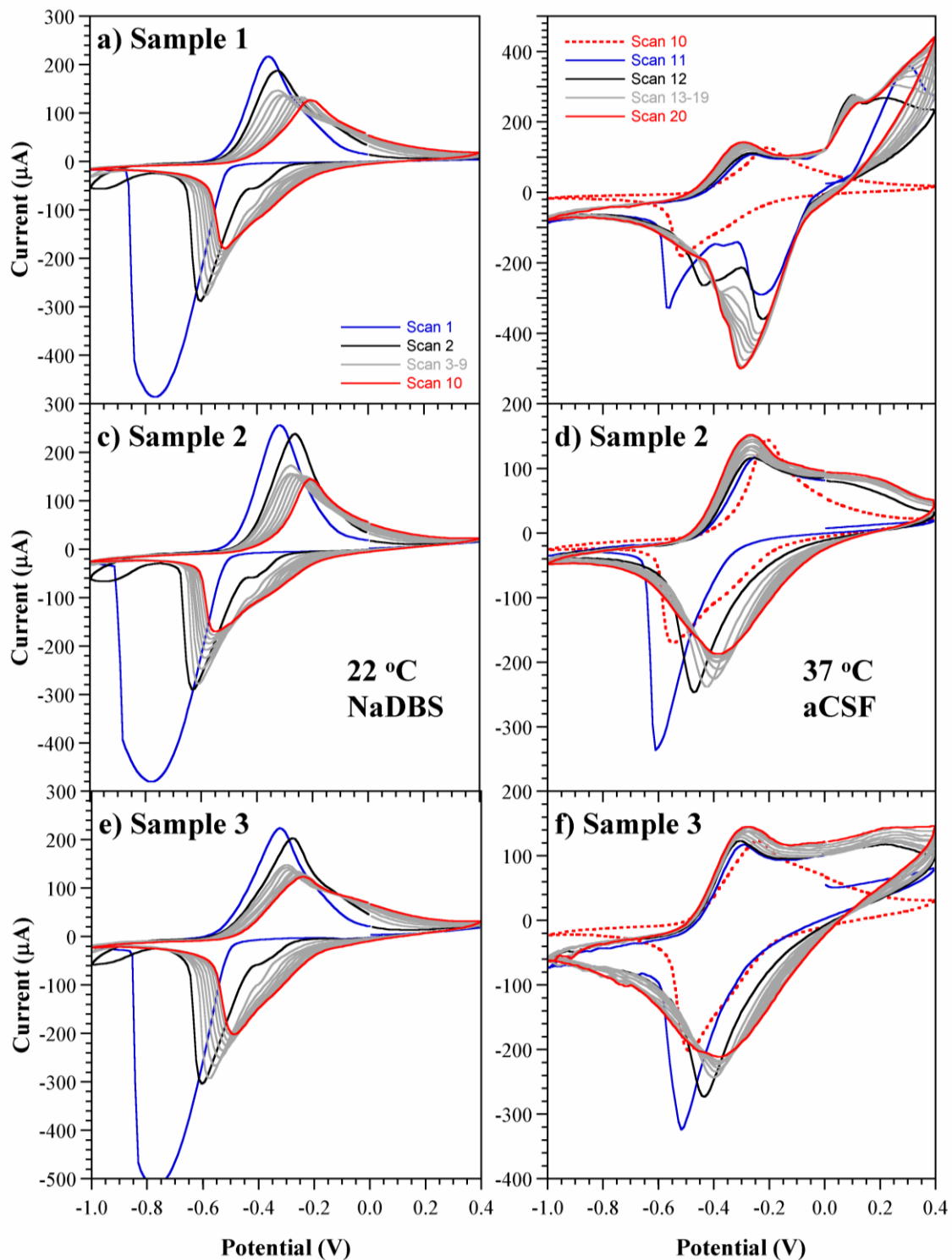
Sup. Figure 2-3. Cyclic voltammograms of three samples cycled in NaDBS at 22 °C for (left) the first 10 scans and then (right) the second 10 scans. To facilitate comparison, since the scales on the left and the right differ, scan 10 is repeated. Sample 3 was used in the main text.



Sup. Figure 2-4. Cyclic voltammograms of three samples cycled in NaDBS at (left) 22 °C for the first 10 scans and then (right) at 37 °C for the second 10 scans. Sample 2 was used in the main text.



Sup. Figure 2-5. Cyclic voltammograms of three samples cycled (left) in NaDBS at 22 °C for the first 10 scans and then (right) in aCSF at 22 °C for the second 10 scans. Sample 3 was used in the main text.

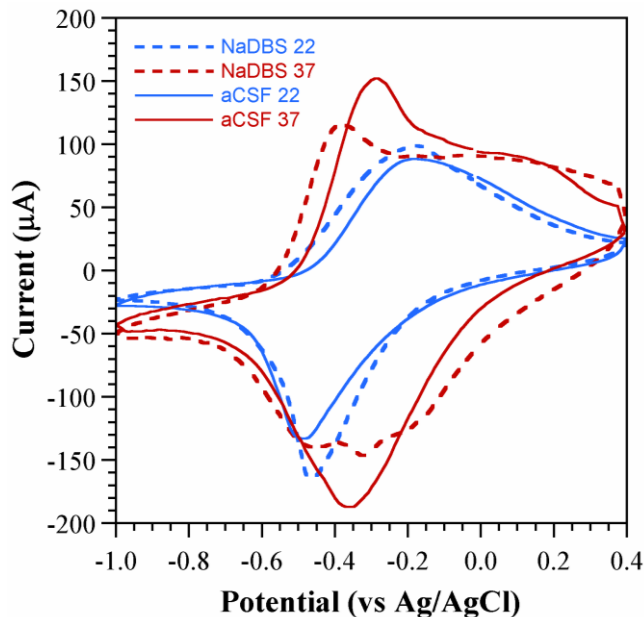


Sup. Figure 2-6. Cyclic voltammograms of three samples cycled (left) in NaDBS at 22 °C for the first 10 scans and then (right) in aCSF at 37 °C for the second 10 scans. Note that the vertical scale for (b) is almost twice that for (d) and (f). Sample 2 was used in the main text.

The expected large current is seen during the very first reduction scan in NaDBS [61]. Thereafter, the reduction peak shifts anodically (to the right) and decreases in height. The second scan shows a small current at -1 V that is not seen in any of the other scans. The oxidation peak shifts anodically and also decreases in size with scan number. The CVs have not completely stabilized after the first 10 scans. In Sup. Figure 2-3, the cycling continues in the same NaDBS solution, after the samples were removed from the cell and placed back into it. The anodic shifts and reductions in current magnitude continue. It is possible that an irreversible change is occurring, such as delamination. Sample 3 in Sup. Figure 2-3f is an exception, since the CVs more or less stabilize; this sample also has the highest currents, or exchanged charge, supporting the hypothesis that the others may be delaminating.

As noted above, the samples later cycled at room temperature (Sup. Figure 2-3 and Sup. Figure 2-5) were polymerized individually, while those later cycled at 37 °C (Sup. Figure 2-4 and Sup. Figure 2-6) were all polymerized together. The CVs of the former showed somewhat greater variability upon cycling in NaDBS than did the latter, but the basic behavior was the same.

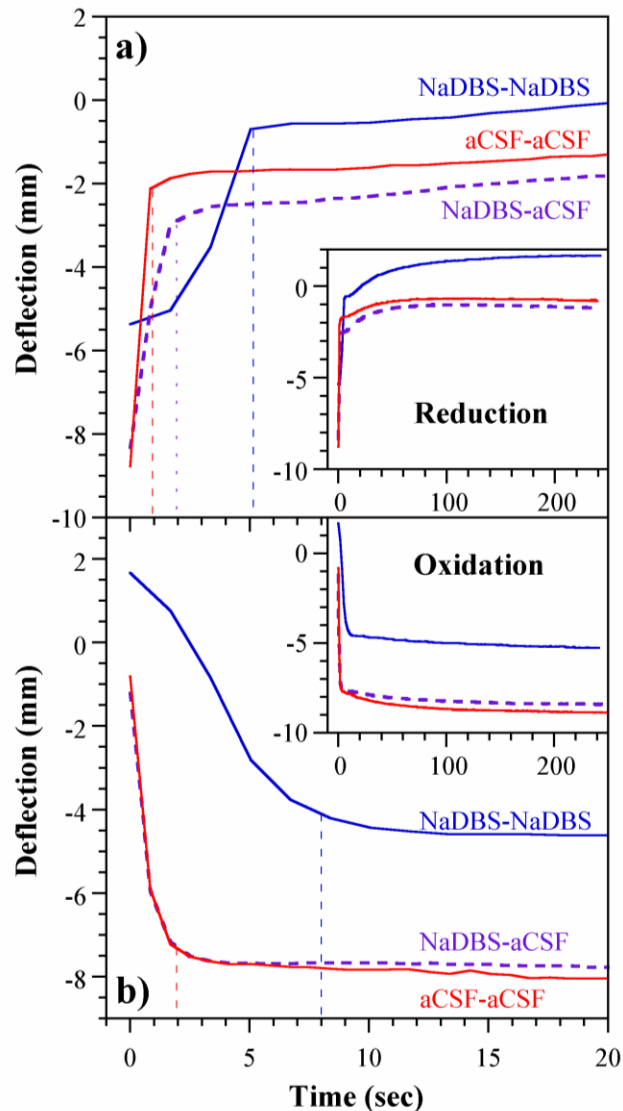
Sup. Figure 2-7 overlays the current-voltage relationships in the four solutions in scan 19 for the samples of Figure 2-4 in the main text.



Sup. Figure 2-7. Typical cyclic voltammograms in the four solutions.

2.6.4 Deflection upon voltage stepping

During slow potential scanning the deflection is limited by the scan rate, but under a voltage step the speed is determined by the rate-limiting oxidation or reduction process, typically mass transport of the solvated ions within the polymer [73]. To ascertain the speed of the actuators, voltage stepping was carried out. Three new samples were primed by performing ten CVs at 25 mV/s; two in NaDBS at RT and one in aCSF at RT. Next, the samples were stepped ten times between 0.4 V and -1.0 V using a voltage square wave, holding each potential for 240 seconds. One was stepped in NaDBS at RT (NaDBS-NaDBS) and two in aCSF at 37 °C (NaDBS-aCSF & aCSF-aCSF). The tip deflections from the video and the current data were synchronized and segmented into reduction and oxidation partitions. The deflections from the final cycle are shown in Sup. Figure 2-8. Curve fitting was accomplished using Matlab, and rise and fall time constants were obtained.



Sup. Figure 2-8. Preliminary data for 3 samples (one per group). Deflection during the 10th step between 0.4 V and -1.0 V either in NaDBS at RT or in aCSF at 37 °C after prior electrochemical cycling in one of these two solutions at RT. NaDBS-NaDBS indicates priming in NaDBS followed by stepping in NaDBS.

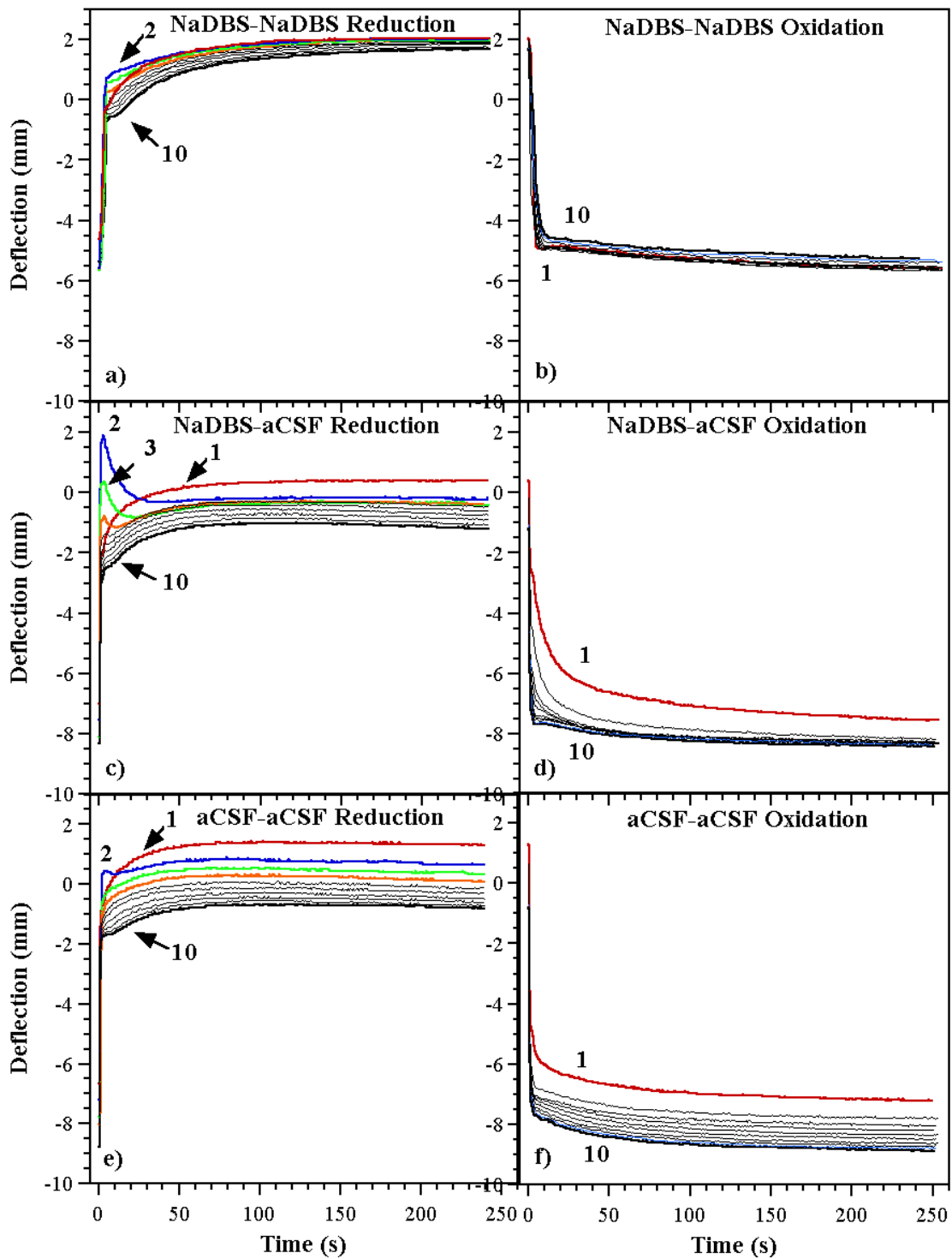
Tip deflections comprised an initial fast movement that took on the order of seconds (indicated by the dashed vertical lines) followed by a slower movement that took place on the order of hundreds of seconds (shown in the inset). The two bilayers that were stepped in 37 °C aCSF moved more quickly during the first few seconds than the one in 22 °C NaDBS. The fast component, which would be the one used in actual applications, was

approximately 5 seconds for reduction and 8 seconds for oxidation in 22 °C NaDBS, while it was 1-2 seconds for reduction and 2 seconds for oxidation in 37 °C aCSF, about 4 times faster. The increase in speed with temperature is fortunate for applications in the body.

Over longer times, the deflections gradually increased somewhat further. This is in the opposite direction as observed for salt draining in PPy(DBS) [74], instead suggesting a continued slow uptake of mass during reduction and loss of mass during oxidation, indicating a very slow-moving species or slow polymer chain motions [75].

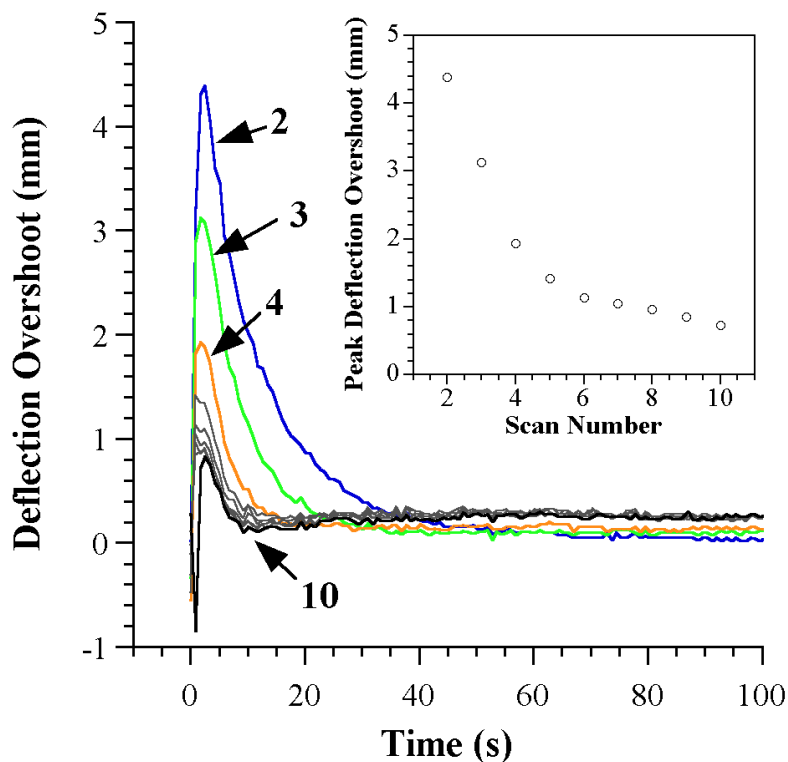
2.6.5 Transient effects upon voltage stepping

The data in Sup. Figure 2-8 are for the 10th step in the second electrolyte. All 10 tip deflections in each electrolyte are shown in Sup. Figure 2-9. With each step, the final deflections under all three conditions, during both oxidation and reduction, shifted downward on the y axis, from positive displacements toward (more) negative ones. The shifts were larger in aCSF at 37 °C than they were in NaDBS at RT. For the NaDBS-aCSF (Sup. Figure 2-9c) condition, there were noticeable overshoots during reduction in which the deflection changed direction. Interestingly, the overshoot peak was not present during the first reduction step; instead, it was maximal in the second step and persisted until the fifth. A small overshoot was also seen in the second step upon raising the temperature from 22 °C to 37 °C in aCSF.



Sup. Figure 2-9. Preliminary data for 3 samples. Step responses of ten consecutive oxidation and reduction cycles, overlaid, in either NaDBS at RT or aCSF at 37 °C. Samples “NaDBS-aCSF” and “aCSF-aCSF” were stepped in 37 °C aCSF after priming in NaDBS at RT or aCSF at RT, respectively.

The transient deflection peaks during reduction of the NaDBS-aCSF sample were extracted from the deflection profile by subtracting scan 1 from subsequent scans and considering the “deflection overshoot” as the distance relative to scan 1’s steady state value. The resultant peaks indicate the differences in the initial response and are shown in Sup. Figure 2-10. Despite the fact that the tip reached a steady final value, the overshoot peak reappeared in the next scan, although its magnitude decayed in each subsequent step. Even after ten scans there was a residual 0.8 mm overshoot that decayed over 5 sec. This transient peak was not found in the NaDBS-NaDBS sample, and it was less prominent in the aCSF sample primed in aCSF.



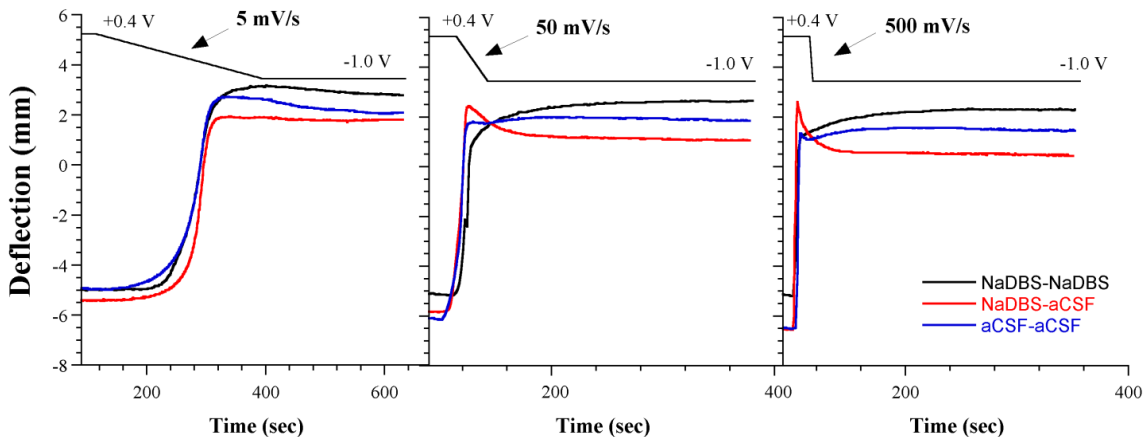
Sup. Figure 2-10. Preliminary data for 3 samples. Transient deflection peaks during reduction for scans 2-10 relative to scan 1 for the sample primed in NaDBS at RT and cycled in aCSF at 37 °C (NaDBS-aCSF, Sup. Figure 2-9c). Deflection overshoot is the difference of each scan relative to the steady state value of scan 1 (at 100 s). The peak deflection overshoots for scans 2-10 are plotted in the inset.

Reversals in beam motion have been seen when motion of one species in one direction is followed by motion of another species of the opposite charge in the opposite direction, with the time lag due to differences in mobility (and thus transport speeds) due to e.g. ion sizes [22, 40, 69, 76]. It is also known that the ions in conjugated polymers can be completely exchanged upon cycling in different electrolytes, and this was also shown for this PPy(DBS) system by the EDX spectra in Figure 2-6. The reduction in the amplitude of the overshoot peak with cycle number is not inconsistent with replacement of the ions. Another interpretation is that the overshoot is related to water transport. Skaarup et al. reported an actuation-frequency-dependent strain and proposed that actuation speed depends not only on the transport rate of hydrated ions, but also on the rate of movement of water that is not directly associated with ions due to changes in osmotic pressure as the ion concentrations within the polymer change [21]. The lesson from this transient behavior is that the actuators must be primed under the conditions in which they will be applied, or else ion-exchange phenomena may result in poor control during the initial cycles.

2.6.6 Ramping voltage to attenuate initial transient effects

In section 2.6.5, the stepping experiments revealed a transient behavior. To further examine this, the applied voltage was ramped at different rates. Three fresh samples (polymerized together) were first primed by 10 CVs at 25 mV/s in either NaDBS at RT or aCSF at 37 °C. Immediately afterward (in the case of NaDBS-aCSF after transferring to the 2nd electrolyte), the actuators were held at +0.4 V for 100 seconds, ramped down to -1.0 V at 5 mV/s, and then held for 240 seconds. The priming-(transferring)-ramping

procedure was repeated at voltage ramps of 50 and 500 mV/s in either NaDBS at RT or aCSF at 37 °C. The beam tip deflections are shown in Sup. Figure 2-11.



Sup. Figure 2-11. Deflection as a function of time in response to the voltage profiles shown at the top: samples were held at +0.4 V (oxidized) for 100 seconds, ramped to -1.0 V (reduced) at varying scan rates (5, 50, and 500 mV/s), and then held at -1.0 V for 240 seconds. Priming and ramping electrolytes were either NaDBS at RT or aCSF at 37 °C.

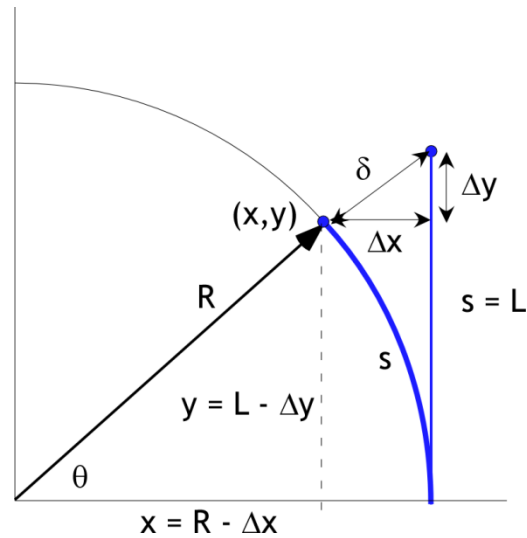
As expected, the bending behavior of the NaDBS-NaDBS sample was similar at the three ramp rates. However, the bending behavior of the NaDBS-aCSF sample depended strongly on the ramp rate, and that of the aCSF-aCSF sample less so.

At 5 mV/s, the deflections changed substantially monotonically, although the aCSF-aCSF sample drifted from its maximum deflection to a less curved state over the next 300 seconds, as did the NaDBS-NaDBS sample to a lesser extent. At 50 and 500 mV/s, the tip of the NaDBS-aCSF sample swung back again instead of remaining still. At 50 mV/s, the tip “overshot” by 1.3 mm beyond the final value (19% of the peak-to-peak value), reversed, and settled to its final position during the first 20 seconds. At 500 mV/s the overshoot was even larger at 2 mm (28% of the final value), but it settled to its final value in about half the time, within 11 sec.

These transients are likely due to multiple ion transport events with different rates, such as the incorporation of ions other than Na⁺ and the expulsion of Na⁺, although one cannot rule out contributions due to the expulsion of water or changes in chain conformation. As discussed in the previous section, transients are undesirable in an application setting. These results motivate future protocols for priming the actuators after deposition in an ionic medium and temperature matching those in the final application. A more thorough investigation would need to be performed to better understand the overshoot phenomenon.

2.6.7 Calculation of curvature and actuation strain from deflection measurements

The curvature of the beam was obtained by trigonometry from the measured Δx and Δy deflections of the beam tip.



Sup. Figure 2-12. Trigonometry of beam bending used to obtain curvature.

$$(1) \quad \delta = \sqrt{\Delta x^2 + \Delta y^2}$$

$$(2) \quad R^2 = (L - \Delta y)^2 + (R - \Delta x)^2 = (L - \Delta y)^2 + R^2 - 2R\Delta x + \Delta x^2$$

$$(3) \quad R = \frac{(L - \Delta y)^2 + \Delta x^2}{2\Delta x}$$

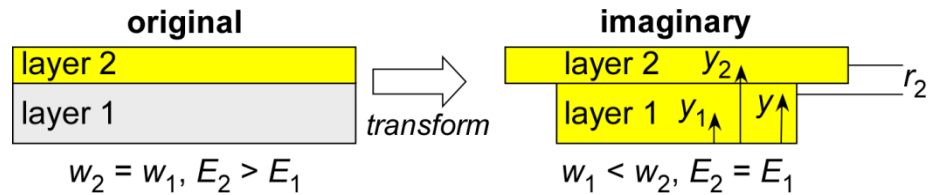
$$(4) \quad \kappa = \frac{1}{R} = \frac{2\Delta x}{(L - \Delta y)^2 + \Delta x^2}$$

2.6.8 Calculation of effective substrate modulus

The bilayer model

$$(5) \quad \kappa = \frac{\alpha_{PPy}}{h_{sub}} \frac{6mn(1+m)}{1 + 4mn + 6m^2n + 4m^3n + m^4n^2}$$

was used with an effective modulus E_{sub} for the Parylene+Cr+Au composite substrate. E_{sub} was determined by the transformed section method and the parallel-axis theorem to determine the moment of inertia for a composite area [54, 77]. In the transformed section method, the widths of the layers in the composite beam are adjusted to create an imaginary beam composed of only one material, in this case Au. The layer thicknesses for the Parylene, Cr, and Au were h_{Pa} , h_{Cr} , and h_{Au} respectively. (The beam width w cancels out).



Sup. Figure 2-13. Beam cross-sections illustrating the transformed section method for a 2-layer beam.

The width ratios are given by n_i :

$$(6) \quad n_1 = \frac{E_{Cr}}{E_{Au}}, \quad n_2 = \frac{E_{Pa}}{E_{Au}} .$$

Next, the parallel-axis theorem is used to determine the moment of inertia for the imaginary beam. The moment of inertia I_{yi} of a layer with respect to the plane going through its center of mass is equal to the moment of inertia I'_{yi} with respect to any parallel plane plus the product of the area A_i and the square of the distance r_i between the two planes. The moment of inertia of a composite beam I_y is the sum of the moments of inertia of all the layers with respect to the same reference plane.

$$(7) \quad I_y = \sum_{i=1}^n I_{yi} = \sum_{i=1}^n I'_{yi} + A_i \cdot r_i^2$$

where $r_i = y_i - y$ and y is the position of the reference plane. The reference plane was chosen at the centroid (geometric center) of the imaginary beam, a distance y from the bottom of the beam, given by:

$$(8) \quad y = \frac{\sum_{i=1}^n y_i A_i}{\sum_{i=1}^n A_i} = \frac{h_{Au} \left(h_{Cr} + h_{Pa} + \frac{h_{Au}}{2} \right) + n_1 \cdot h_{Cr} \left(h_{Pa} + \frac{h_{Cr}}{2} \right) + n_2 \cdot h_{Pa} \left(\frac{h_{Pa}}{2} \right)}{h_{Au} + n_1 \cdot h_{Cr} + n_2 \cdot h_{Pa}}$$

where y_i is the centroid of each layer and A_i is the cross-sectional area (thickness*width) of each transformed layer.

Substituting Equation (8) for every layer into equation y, I_y is given as:

$$(9) \quad I_y = w \left(\begin{aligned} & \frac{1}{12} h_{Au}^3 + h_{Au} \left(h_{Cr} + h_{Pa} + \frac{h_{Au}}{2} - y \right)^2 + \frac{1}{12} n_1 \cdot h_{Cr}^3 \\ & + n_1 \cdot h_{Cr} \left(h_{Pa} + \frac{h_{Cr}}{2} - y \right)^2 + \frac{1}{12} n_2 \cdot h_{Pa}^3 + n_2 \cdot h_{Pa} \left(y - \frac{h_{Pa}}{2} \right)^2 \end{aligned} \right)$$

The composite substrate equivalent stiffness $(EI)_{sub}$ is obtained by multiplying the Young's modulus E of the reference layer, here E_{Au} , by I_y .

$$(10) \quad (EI)_{sub} = E_{Au} \cdot I_y$$

The moment of inertia of the imaginary beam is I_{sub} .

$$(11) \quad I_{sub} = \frac{1}{12} w \cdot (h_{Au} + h_{Cr} + h_{Pa})^3$$

E_{sub} is finally obtained by dividing the equivalent stiffness $(EI)_{sub}$ by I_{sub} .

$$(12) \quad E_{sub} = \frac{(EI)_{sub}}{I_{sub}}$$

The Young's modulus E_{pa} for Parylene-C was reported by the manufacturer [78] to be 2.76 GPa, but another reports places it between 3.0-3.2 GPa [79] and a third as high as 4.75 GPa [80]. The manufacturer's value was used for this work. The bulk modulus for Au of $E_{Au} = 83$ GPa was used here, although the value for thin film gold has been reported as differing from this [33, 81]. The Cr adhesion layer is generally ignored, but it was thicker than usual on these beams (150 Å) and the Young's modulus E_{Cr} of Cr is high, ranging from 86 GPa up to 279 GPa in bulk Cr [82], so it may significantly contribute to the composite thickness. However, thin film deposited Cr has a reported value of 180 GPa [83]. Therefore, the conservative value of 180 GPa was used for this work. Using these values, the average E_{sub} was 5.07 ± 0.09 GPa. Strains derived from a multiple layer model [84] were compared with those from the bilayer model, and the difference was about 0.3%. The largest uncertainty was contributed by the Parylene layer thicknesses, which were known only to within ± 0.8 μm .

Sup. Table 2-2. Average actuation strain α , exchanged charge density, and strain-to-charge density (during reduction and oxidation and their sum) in the 9th and 19th scans under different cycling conditions, as well as the ratios of the 19th and 9th scan (n = 3).

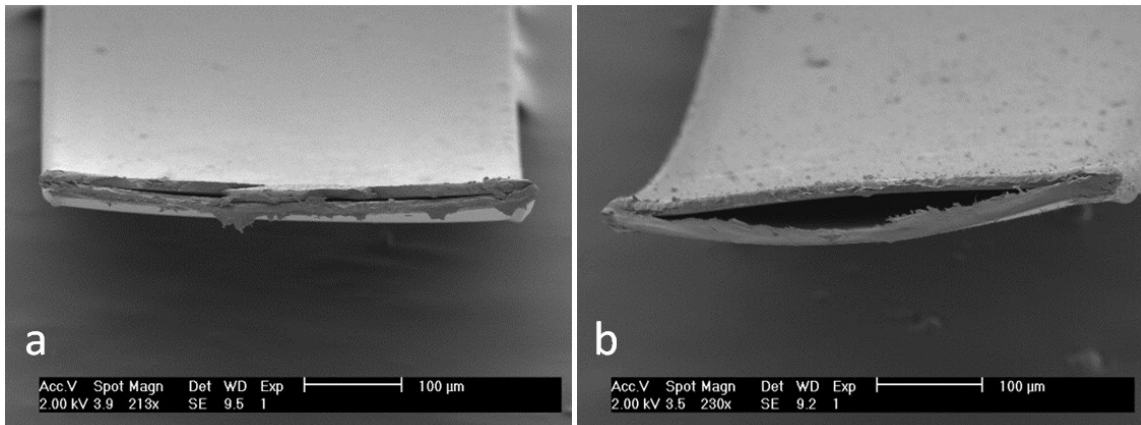
Scan 9		NaDBS RT		NaDBS 37C		aCSF RT		aCSF 37C	
α Reduction	%	0.46	± 0.12	0.34	± 0.02	0.43	± 0.11	0.25	± 0.00
α Oxidation	%	-0.35	± 0.08	-0.46	± 0.02	-0.23	± 0.06	-0.39	± 0.06
α Total	%	0.81	± 0.21	0.80	± 0.02	0.66	± 0.17	0.64	± 0.06
Re Charge Density	C/m ³ x 10 ⁶	101	± 14	102	± 19	89	± 17	105*	
Ox Charge Density	C/m ³ x 10 ⁶	82	± 11	85	± 8	69	± 13	79*	
Total Charge Density	C/m ³ x 10 ⁶	183	± 24	187	± 21	158	± 28	184*	
Re α / Charge Density	($\Delta l/l$) / (C/m ³) x 10 ⁻¹²	45.68	± 13.89	33.24	± 6.57	48.70	± 15.35	23.35	± 0.47
Ox α / Charge Density	($\Delta l/l$) / (C/m ³) x 10 ⁻¹²	-42.81	± 11.47	-53.70	± 5.76	-33.08	± 10.88	-49.88	± 7.66
Tot α / Charge Density	($\Delta l/l$) / (C/m ³) x 10 ⁻¹²	44.40	± 12.64	42.54	± 4.95	41.88	± 13.08	34.74	± 3.47

Scan 19		NaDBS RT		NaDBS 37C		aCSF RT		aCSF 37C	
α Reduction	%	0.50	± 0.14	0.20	± 0.03	0.37	± 0.11	0.10	± 0.07
α Oxidation	%	-0.32	± 0.13	-0.70	± 0.07	-0.21	± 0.04	-0.50	± 0.04
α Total	%	0.83	± 0.25	0.90	± 0.07	0.59	± 0.15	0.60	± 0.11
Re Charge Density	C/m ³ x 10 ⁶	112	± 9	182	± 26	91	± 4	176*	
Ox Charge Density	C/m ³ x 10 ⁶	87	± 13	133	± 18	70	± 2	135*	
Total Charge Density	C/m ³ x 10 ⁶	199	± 21	311	± 44	161	± 22	312*	
Re α / Charge Density	($\Delta l/l$) / (C/m ³) x 10 ⁻¹²	45.03	± 13.36	10.84	± 2.10	41.08	± 12.08	5.56	± 3.86
Ox α / Charge Density	($\Delta l/l$) / (C/m ³) x 10 ⁻¹²	-37.34	± 15.60	-52.61	± 9.05	-30.47	± 5.67	-37.26	± 3.21
Tot α / Charge Density	($\Delta l/l$) / (C/m ³) x 10 ⁻¹²	41.67	± 13.43	28.84	± 4.59	36.47	± 10.45	19.26	± 3.49

Ratio of Scans 19/9		NaDBS RT		NaDBS 37C		aCSF RT		aCSF 37C	
α Reduction		1.09	± 0.43	0.58	± 0.09	0.86	± 0.33	0.40	± 0.28
α Oxidation		0.93	± 0.42	1.53	± 0.18	0.93	± 0.31	1.28	± 0.22
α Total		1.02	± 0.40	1.13	± 0.09	0.89	± 0.32	0.94	± 0.19
Re Charge Density		1.11	± 0.18	1.78	± 0.42	1.02	± 0.20	1.68*	
Ox Charge Density		1.06	± 0.21	1.56	± 0.26	1.01	± 0.19	1.71*	
Total Charge Density		1.09	± 0.18	1.66	± 0.30	1.02	± 0.23	1.70*	
Re α / Charge Density		0.99	± 0.42	0.33	± 0.09	0.84	± 0.36	0.24	± 0.17
Ox α / Charge Density		0.87	± 0.43	0.98	± 0.20	0.92	± 0.35	0.75	± 0.13
Tot α / Charge Density		0.94	± 0.40	0.68	± 0.13	0.87	± 0.37	0.55	± 0.11

* Denotes data from one sample.

2.6.9 Cross-sectional images of devices showing delamination



Sup. Figure 2-14. SEM images of bilayer cross sections of devices after being cut mid-length with some samples showing (a) no delamination and (b) delamination of the PPy layer. The delamination may have occurred during actuation or due to cutting.

In order to quantify the layer thicknesses, devices were cut using a razor blade midway along the length of the beam. Images of the cross-section of many of the devices showed signs of delamination, such as in Sup. Figure 2-14b. Delamination during actuation may explain the shifts in repeated CV current peaks as seen in 2.6.3, however, it is difficult to distinguish when the separation occurred.

2.7 References

- [1] E. Smela, "Conjugated polymer actuators for biomedical applications," *Adv. Mater.*, 15, 481-494, 2003.
- [2] C. Immerstrand, K. Holmgren-Peterson, K. E. Magnusson, E. Jager, M. Krogh, M. Skoglund, A. Selbing, and O. Inganäs, "Conjugated-polymer micro- and milliactuators for biological applications," *MRS Bull.*, 27, 461-464, 2002.
- [3] P. M. George, A. W. Lyckman, D. A. LaVan, A. Hegde, Y. Leung, R. Avasare, C. Testa, P. M. Alexander, R. Langer, and M. Sur, "Fabrication and biocompatibility of polypyrrole implants suitable for neural prosthetics," *Biomaterials*, 26, 3511-3519, 2005.
- [4] R. A. Green, N. H. Lovell, G. G. Wallace, and L. A. Poole-Warren, "Conducting polymers for neural interfaces: Challenges in developing an effective long-term implant," *Biomaterials*, 29, 3393-3399, 2008.
- [5] K. K. C. Lee, N. R. Munce, T. Shoa, L. G. Charron, G. A. Wright, J. D. Madden, and V. X. D. Yang, "Fabrication and characterization of laser-micromachined polypyrrole-based artificial muscle actuated catheters," *Sens. Act. A*, 153, 230-236, 2009.
- [6] E. W. H. Jager, E. Smela, and O. Inganäs, "Microfabricating conjugated polymer actuators," *Science*, 290, 1540-1545, 2000.
- [7] C. E. Schmidt, V. R. Shastri, J. P. Vacanti, and R. Langer, "Stimulation of neurite outgrowth using an electrically conducting polymer," *Proc. Natl. Acad. Sci.*, 94, 8948-8953, 1997.
- [8] R. L. Williams and P. J. Doherty, "A preliminary assessment of poly(pyrrole) in nerve guide studies," *J. Mater. Sci. Mater. Med.*, 5, 429-433, 1994.
- [9] X. D. Wang, X. S. Gu, C. W. Yuan, S. J. Chen, P. Y. Zhang, T. Y. Zhang, J. Yao, F. Chen, and G. Chen, "Evaluation of biocompatibility of polypyrrole in vitro and in vivo," *J. Biomed. Mater. Res. A*, 68A, 411-422, 2004.
- [10] D. D. Ateh, H. A. Navsaria, and P. Vadgama, "Polypyrrole-based conducting polymers and interactions with biological tissues," *J. R. Soc. Interface*, 3, 741-752, 2006.
- [11] B. Shapiro and E. Smela, "Bending actuators with maximum curvature and force and zero interfacial stress," *J. Intel. Mat. Syst. Str.*, 18, 181-186, 2007.

- [12] A. S. Hutchison, T. W. Lewis, S. E. Moulton, G. M. Spinks, and G. G. Wallace, "Development of polypyrrole-based electromechanical actuators," *Synth. Met.*, 113, 121-127, 2000.
- [13] L. Bay, K. West, and S. Skaarup, "Pentanol as co-surfactant in polypyrrole actuators," *Polymer*, 43, 3527-3532, 2002.
- [14] E. Smela, "Microfabrication of PPy microactuators and other conjugated polymer devices," *J. Micromech. Microeng.*, 9, 1-18, 1999.
- [15] Y. Liu, Q. Gan, S. Baig, and E. Smela, "Improving PPy adhesion by surface roughening," *J. Phys. Chem. C*, 111, 11329-11338, 2007.
- [16] J. G. Cham, E. A. Branchaud, Z. Nenadic, B. Greger, R. A. Andersen, and J. W. Burdick, "Semi-chronic motorized microdrive and control algorithm for autonomously isolating and maintaining optimal extracellular action potentials," *J. Neurophysiol.*, 93, 570-579, 2005.
- [17] D. V. Palanker, A. Vankov, P. Huie, and S. A. Baccus, "Design of a high-resolution optoelectronic retinal prosthesis." *J. Neural Eng.*, 2, S105-S120, 2005.
- [18] B. S. Wilson and M. F. Dorman, "Cochlear implants: A remarkable past and a brilliant future," *Hear. Res.*, 242, 3-21, 2008.
- [19] J. A. Saint-Cyr, T. Hoque, L. C. M. Pereira, J. O. Dostrovsky, W. D. Hutchison, D. J. Mikulis, A. Abosch, E. Sime, A. E. Lang, and A. M. Lozano, "Localization of clinically effective stimulating electrodes in the human subthalamic nucleus on magnetic resonance imaging," *J. Neurosurg.*, 97, 1152-1166, 2002.
- [20] E. D. Daneshvar, D. R. Kipke, and E. Smela, "Navigating conjugated polymer actuated neural probes in a brain phantom," *Proc. SPIE Smart Struct. Mater. (EAPAD)*, San Diego, vol. 8340, 09.1-09.12, edited by Y. Bar-Cohen (March 12-15, 2012).
- [21] M. J. M. Jafeen, M. A. Careem, and S. Skaarup, "Speed and strain of polypyrrole actuators: dependence on cation hydration number," *Ionics*, 16, 1-6, 2010.
- [22] S. Skaarup, L. Bay, K. Vidanapathirana, S. Thybo, P. Tofte, and K. West, "Simultaneous anion and cation mobility in polypyrrole," *Solid State Ionics*, 159, 143-147, 2003.
- [23] L. Bay, N. Mogensen, S. Skaarup, P. Sommer-Larsen, M. Jorgensen, and K. West, "Polypyrrole doped with alkyl benzenesulfonates," *Macromolecules*, 35, 9345-9351, 2002.

- [24] A. G. MacDiarmid, "Synthetic metals: a novel role for organic polymers," *Synth. Met.*, 125, 11-22, 2001.
- [25] A. F. Diaz and J. Bargon, "Electrochemical synthesis of conducting polymers " in Handbook of Conducting Polymers, T. A. Skotheim, Ed., (Dekker, New York, 1986).
- [26] T. Shoa, T. Mirfakhrai, and J. D. W. Madden, "Electro-stiffening in polypyrrole films: Dependence of Young's modulus on oxidation state, load and frequency," *Synth. Met.*, 160, 1280-1286, 2010.
- [27] J. Kielland, "Individual activity coefficients of ions in aqueous solutions," *J. Am. Chem. Soc.*, 59, 1675-1678, 1937.
- [28] M. A. Careem, K. P. Vidanapathirana, S. Skaarup, and K. West, "Dependence of force produced by polypyrrole-based artificial muscles on ionic species involved," *Solid State Ionics*, 175, 725-728, 2004.
- [29] M. A. Careem, Y. Velmurugu, S. Skaarup, and K. West, "A voltammetry study on the diffusion of counter ions in polypyrrole films," *J. Power Sources*, 159, 210-214, 2006.
- [30] T. Shimizu and A. Minakata, "Effect of divalent cations on the volume of a maleic acid copolymer gel examined by incorporating lysozyme," *Eur. Polym. J.*, 38, 1113-1120, 2002.
- [31] R. John and G. G. Wallace, "Doping-dedoping of polypyrrole: a study using current-measuring and resistance-measuring techniques," *J. Electroanal. Chem.*, 354, 145-160, 1993.
- [32] M. R. Gandhi, P. Murray, G. M. Spinks, and G. G. Wallace, "Mechanism of electromechanical actuation in polypyrrole," *Synth. Met.*, 73, 247-256, 1995.
- [33] M. Christophersen, B. Shapiro, and E. Smela, "Characterization and modeling of PPy bilayer microactuators - Part 1. Curvature," *Sens. Act. B*, 115, 596-609, 2006.
- [34] E. Smela and N. Gadegaard, "Surprising volume change in PPy(DBS): An atomic force microscopy study," *Adv. Mater.*, 11, 953-957, 1999.
- [35] Q. B. Pei and O. Inganäs, "Electrochemical applications of the bending beam method: 1. Mass-transport and volume changes in polypyrrole during redox," *J. Phys. Chem.*, 96, 10507-10514, 1992.
- [36] S. Skaarup, K. West, L. M. W. K. Gunaratne, K. P. Vidanapathirana, and M. A. Careem, "Determination of ionic carriers in polypyrrole," *Solid State Ionics*, 136, 577-582, 2000.

- [37] H. Yang and J. Kwak, "Mass transport investigated with the electrochemical and electrogravimetric impedance techniques. 2. Anion and water transport in PMPy and PPy films," *J. Phys. Chem. B*, 101, 4656-4661, 1997.
- [38] Q. B. Pei and O. Inganäs, "Electrochemical applications of the bending beam method; a novel way to study ion-transport in electroactive polymers," *Solid State Ionics*, 60, 161-166, 1993.
- [39] B. Gaihre, S. Ashraf, G. M. Spinks, P. C. Innis, and G. G. Wallace, "Comparative displacement study of bilayer actuators comprising of conducting polymers, fabricated from polypyrrole, poly(3,4-ethylenedioxythiophene) or poly(3,4-propylenedioxythiophene)," *Sens. Act. A*, 193, 48-53, 2013.
- [40] N. Vandesteeg, P. G. Madden, J. D. Madden, P. A. Anquetil, and I. W. Hunter, "Synthesis and characterization of EDOT-based conducting polymer actuators," *Proc. SPIE Smart Struct. Mater. (EAPAD)*, San Diego, vol. 5051, 349-356, edited by Y. Bar-Cohen (March 2-6, 2003).
- [41] M. Christophersen and E. Smela, "Polypyrrole/gold bilayer microactuators: Response time and temperature effects," *Proc. SPIE Smart Struct. Mater. (EAPAD)*, San Diego, vol. 6168, (February 27 - March 2, 2006).
- [42] S. Fanning, , "*Characterization of polypyrrole/gold bilayers for micro-valve design*," PhD. dissertation, University of Maryland, College Park, MD, 2005.
- [43] J. D. Madden, D. Rinderknecht, P. A. Anquetil, and I. W. Hunter, "Creep and cycle life in polypyrrole actuators," *Sens. Act. A*, 133, 210-217, 2007.
- [44] X. Z. Wang and E. Smela, "Cycling conjugated polymers with different cations," *Proc. SPIE Smart Struct. Mater. (EAPAD)*, San Diego, vol. 6168, (February 27-March 2, 2006).
- [45] S. Maw, E. Smela, K. Yoshida, and R. B. Stein, "Effects of monomer and electrolyte concentrations on actuation of PPy(DBS) bilayers," *Synthetic Metals*, 155, 18-26, 2005.
- [46] S. S. Pandey, W. Takashima, and K. Kaneto, "Conserved electrochemomechanical activities of polypyrrole film in complex buffer media," *Sens. Act. B*, 102, 142-147, 2004.
- [47] W. Takashima, S. S. Pandey, and K. Kaneto, "Cyclic voltammetric and electrochemomechanical characteristics of freestanding polypyrrole films in diluted media," *Thin Solid Films*, 438, 339-345, 2003.

- [48] E. C. McNay and R. S. Sherwin, "From artificial cerebro-spinal fluid (aCSF) to artificial extracellular fluid (aECF): microdialysis perfusate composition effects on in vivo brain ECF glucose measurements," *J. Neurosci. Methods*, 132, 35-43, 2004.
- [49] I. S. Kass, A. A. Bendo, A. E. Abramowicz, and J. E. Cottrell, "Methods for studying the effect of anesthetics on anoxic damage in the rat hippocampal slice," *J. Neurosci. Methods*, 28, 77-82, 1989.
- [50] S. Maw, E. Smela, K. Yoshida, P. Sommer-Larsen, and R. B. Stein, "The effects of varying deposition current density on bending behaviour in PPy(DBS)-actuated bending beams," *Sens. Act. A*, 89, 175-184, 2001.
- [51] S. Skaarup, K. West, B. Zachaustriensen, M. A. Careem, and G. K. R. Senadeera, "Electrolyte and ion memory effects in highly conjugated polypyrrole," *Solid State Ionics*, 72, 108-114, 1994.
- [52] K. West, T. Jacobsen, B. Zachaustriensen, M. A. Careem, and S. Skaarup, "Electrochemical synthesis of polypyrrole - Influence of current-density on structure," *Synth. Met.*, 55, 1412-1417, 1993.
- [53] S. P. Timoshenko, "Analysis of bi-metal thermostats," *J. Opt. Soc. Am.*, 11, 233-255, 1925.
- [54] J. M. Gere and S. P. Timoshenko, Mechanics of Materials, 4th ed. (PWS-KENT Publishing Company, Boston, 1997).
- [55] H. Yang and J. Kwak, "Mass transport investigated with the electrochemical and electrogravimetric impedance techniques. 1. Water transport in PPy/CuPTS films," *J. Phys. Chem. B*, 101, 774-781, 1997.
- [56] B. J. West, T. F. Otero, B. Shapiro, and E. Smela, "Chronoamperometric study of conformational relaxation in PPy(DBS)," *J. Phys. Chem. B*, 113, 1277-1293, 2009.
- [57] M. A. Depaoli, R. C. D. Peres, S. Panero, and B. Scrosati, "Properties of electrochemically synthesized polymer electrodes .10. Study of polypyrrole dodecylbenzenesulfonate," *Electrochim. Acta.*, 37, 1173-1182, 1992.
- [58] S. Shimoda and E. Smela, "The effect of pH on polymerization and volume change in PPy(DBS)," *Electrochim. Acta.*, 44, 219-238, 1998.
- [59] E. Smela, M. Kallenbach, and J. Holdenried, "Electrochemically driven polypyrrole bilayers for moving and positioning bulk micromachined silicon plates," *J. Microelectromech. Syst.*, 8, 373-383, 1999.

- [60] P. Chiarelli, A. Della Santa, D. De Rossi, and A. Mazzoldi, "Actuation properties of electrochemically driven polypyrrole freestanding films," *J. Intell. Mater. Syst. Struct.*, 6, 32-37, 1995.
- [61] E. Smela and N. Gadegaard, "Volume change in polypyrrole studied by atomic force microscopy," *J. Phys. Chem. B*, 105, 9395-9405, 2001.
- [62] T. F. Otero, J. J. López Cascales, and G. Vázquez Arenas, "Mechanical characterization of free-standing polypyrrole film," *Mat. Sci. Eng. C*, 27, 18-22, 2007.
- [63] T. F. Otero, M. Márquez, and I. J. Suárez, "Polypyrrole: Diffusion coefficients and degradation by overoxidation," *J. Phys. Chem. B*, 108, 15429-15433, 2004.
- [64] X. Z. Wang and E. Smela, "Color and volume change in PPy(DBS)," *J. Phys. Chem. C*, 113, 359-368, 2009.
- [65] J. D. W. Madden, P. G. A. Madden, and I. W. Hunter, "Polypyrrole actuators: modeling and performance," *Proc. SPIE Smart Struct. Mater. (EAPAD)*, Newport Beach, vol. 4329, 72-83, edited by Y. Bar-Cohen (March 5-8, 2001).
- [66] P. A. Anquetil, D. Rinderknecht, N. A. Vandesteeg, J. D. Madden, and I. W. Hunter, "Large strain actuation in polypyrrole actuators," *Proc. SPIE Smart Struct. Mater. (EAPAD)*, San Diego, vol. 5385, 380-387, edited by Y. Bar-Cohen (March 15-18, 2004).
- [67] A. Della Santa, D. De Rossi, and A. Mazzoldi, "Characterization and modelling of a conducting polymer muscle-like linear actuator," *Smart Mater. Struct.*, 6, 23-34, 1997.
- [68] A. Della Santa, D. De Rossi, and A. Mazzoldi, "Performance and work capacity of a polypyrrole conducting polymer linear actuator," *Synth. Met.*, 90, 93-100, 1997.
- [69] K. P. Vidanapathirana, M. A. Careem, S. Skaarup, and K. West, "Ion movement in polypyrrole/dodecylbenzenesulphonate films in aqueous and non-aqueous electrolytes," *Solid State Ionics*, 154, 331-335, 2002.
- [70] A. J. Ramponi and J. M. Jaklevic, "The application of X-ray emission spectra to the identification of particulate sulfur compounds in ambient air," Technical Report, Lawrence Berkeley Lab., California Univ., Berkeley., LBL-7284, December 1978.
- [71] E. D. Daneshvar, E. Smela, and D. R. Kipke, "Mechanical characterization of conducting polymer actuated neural probes under physiological settings," *Proc. SPIE Smart Struct. Mater. (EAPAD)*, San Diego, vol. 7642, 1T.1-1T.10, edited by Y. Bar-Cohen (March 7-11, 2010).

- [72] H. Shinohara, J. Kojima, and M. Aizawa, "Electrically controlled ion transfer and pH change near a conducting polymer-coated electrode," *J. Electroanal. Chem.*, 266, 297-308, 1989.
- [73] X. Z. Wang, B. Shapiro, and E. Smela, "Visualizing ion currents in conjugated polymers," *Adv. Mater.*, 16, 1605-1609, 2004.
- [74] Q. B. Pei and O. Inganäs, "Electrochemical applications of the bending beam method: 2. Electroshrinking and slow relaxation in polypyrrole," *J. Phys. Chem.*, 97, 6034-6041, 1993.
- [75] T. F. Otero and J. M. Garcia de Otazo, "Polypyrrole oxidation: Kinetic coefficients, activation energy and conformational energy," *Synth. Met.*, 159, 681-688, 2009.
- [76] W. Lu, E. Smela, P. Adams, G. Zuccarello, and B. R. Mattes, "Development of solid-in-hollow electrochemical linear actuators using highly conductive polyaniline," *Chem. Mater.*, 16, 1615-1621, 2004.
- [77] W. C. Young, Roark's formulas for stress & strain, 6th ed. (McGraw-Hill, Inc., 1989).
- [78] *Specialty Coating Systems SCS Parylene Properties*, 2010, (Accessed: 11/8/2011), Available: <http://www.scscoatings.com/docs/coatspec.pdf>.
- [79] J. P. Seymour and D. R. Kipke, "Fabrication of polymer neural probes with Sub-cellular features for reduced tissue encapsulation," *Conf. Proc. IEEE Eng. Med. Biol. Soc.*, New York, vol. 1, (August 30-September 3, 2006).
- [80] C. Y. Shih, T. A. Harder, and Y. C. Tai, "Yield strength of thin-film parylene-C," *Microsyst. Technol.*, 10, 407-411, 2004.
- [81] V. K. Pamula, A. Jog, and R. B. Fair, "Mechanical property measurement of thin-film gold using thermally actuated bimetallic cantilever beams," *Nanotech.*, 1, 410-413, 2001.
- [82] J. Lintymer, N. Martin, J. M. Chappe, J. Takadoum, and P. Delobelle, "Modeling of Young's modulus, hardness and stiffness of chromium zigzag multilayers sputter deposited," *Thin Solid Films*, 503, 177-189, 2006.
- [83] K. E. Petersen and C. R. Guarnieri, "Young's modulus measurements of thin films using micromechanics," *J. Appl. Phys.*, 50, 6761-6766, 1979.
- [84] M. Benslimane, P. Gravesen, K. West, S. Skaarup, and P. Sommer-Larsen, "Performance of polymer based actuators: The three-layer model," *Proc. SPIE Smart Struct. Mater. (EAPAD)*, Newport Beach, vol. 3669, 87-97, edited by Y. Bar-Cohen (March 1-4, 1999).

CHAPTER 3 MEMS device for measuring conjugated polymer actuator force and residual stress in bilayers

The device used in this Chapter was originally described in a published paper in the SPIE Smart Structures and Materials: Electroactive Polymer Actuators and Devices (EAPAD) conference proceedings, (March 7-11, 2010, San Diego) titled "Mechanical characterization of conducting polymer actuated neural probes under physiological settings." However, the content of this Chapter is separate and new. Co-author Professor Elisabeth Smela, University of Maryland, contributed significantly to the data analysis.

Abstract

Measuring conjugated polymer actuation forces on the micro-scale and in an aqueous solution is challenging. No reliable method has been developed for bilayer actuators. For PPy(DBS) bilayer actuators, a residual stress forms between the actuator and substrate that has been unappreciated. Unaccounted for, this residual stress may be detrimental to the expected behavior of future applications.

A MEMS tip-weighted conjugated polymer bilayer actuator was designed, fabricated, and tested to quantify actuation force and residual stress. Custom parylene beams were microfabricated with a layer of Cr/Au on top for polymerization. Nickel weights were electroplated at the ends of the beams to apply known forces. PPy(DBS) was polymerized and the devices were cycled in artificial cerebrospinal fluid at 37 °C, as well as in aqueous NaDBS as a control. Digital images and video were analyzed to quantify

the deflections. A corresponding model was developed to quantify actuation forces and residual stress.

3.1 Introduction

Chapter 1 discussed conjugated polymer (CP) actuator performance measurands and testing methods. Differences between free films and bilayer actuators, and the significance of residual stress were discussed.

In this work, a MEMS device for measuring conjugated polymer actuator force and residual stress in bilayers was developed and tested. This device combines the dynamic loading due the bilayer substrate and the static loading due a weight at the end of the beam.

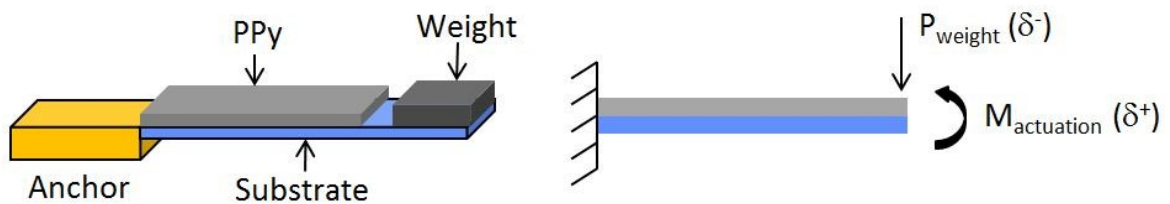


Figure 3-1. (Left) Perspective view of a single weighted bilayer beam. (Right) Diagram showing the counteracting moment and force due to the actuation strain and the weight.

Assuming the approximate polymer Young's modulus and actuation strain based on previous studies allows for prediction of expected bending behavior given the substrate stiffness and CP thickness. These expectations determine the first limitation of the design space. Fabrication considerations determine choices of substrate materials and thicknesses, which influence the beam stiffness. The amount of tip deflection is a factor of the beam width, length, and end weight. The effects of these factors are modeled in the next section.

3.2 Mechanical theory

3.2.1 Combination of forces and moments

In a bilayer actuator, actuation strain induces an interfacial stress gradient with the substrate, which creates a bending moment. In a weighted bilayer beam, the beam bends to the point where the internal moment balances the externally applied moment. The device shown in Figure 3-1 is fixed on one end and has a weight at the other. The weight acts as a point source, opposing vertical deflection of the composite beam.

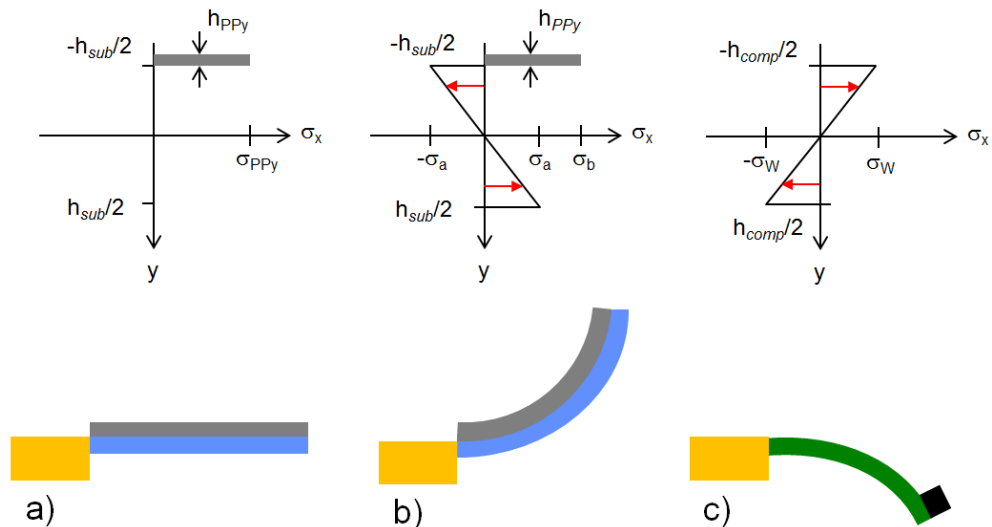


Figure 3-2. Stress distribution in the substrate (a) after polymerization but before priming, (b) after priming, (c) stress due to the weight.

The principle of superposition of forces is valid when (1) Hooke's law holds for the material, (2) deflections and rotations are small, and (3) the deflections do not alter the actions of the applied loads [1]. Assuming these conditions are met, the combined deflection can be modeled as a result of the superposition of the individual deflections due to the actuation moment M and the force of the weight P . The actuation moment M of the composite beam will result in uniform curvature κ and a tip deflection δ (+) proportional to the beam length L [1].

$$(13) \quad \delta_{act} = \frac{\kappa \cdot L^2}{2}$$

The composite beam tip will deflect (-) downward due to the force of the weight P , length L , and the effective stiffness of the composite $(EI)_{comp}$.

$$(14) \quad \delta_{weight} = -\frac{P \cdot L^3}{3 \cdot (E \cdot I)_{comp}}$$

The net measured deflection is a sum of δ_{act} and δ_{weight} .

$$(15) \quad \delta_{Tot} = \delta_{act} + \delta_{weight} = \frac{\kappa \cdot L^2}{2} + \frac{-P \cdot L^3}{3 \cdot (E \cdot I)_{comp}}$$

The inplane strain of the CP actuator layer must exert enough force to bend the substrate layer and also lift the weight at the end. The total deflection should not exceed bending greater than 90° or else the force of gravity would bend the beam more and complicate analysis. Therefore, a working device is considered to have PPy thickness sufficient to result in an actuation moment that bends the substrate, as well as lift the weight, while maintaining uniform curvature.

In the following sections, equations for the curvature κ and effective composite stiffness $(EI)_{comp}$ are established in terms of the device layers used, as shown in Figure 3-3.

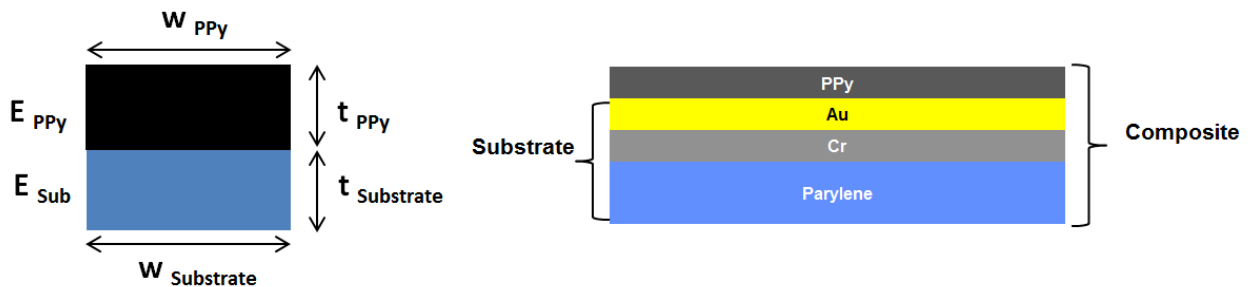


Figure 3-3. Beam cross-sections showing the effective layers (Left) and the layers considered as the composite vs. substrate (Right).

By calculating the stiffness of the substrate layer and measuring the deflection of the composite beam the CP actuation strain can be solved for.

3.2.2 Effective substrate Young's moduli

The bilayer model for curvature:

$$(16) \quad \kappa = \frac{\alpha_{PPy}}{h_{sub}} \frac{6mn(1+m)}{1+4mn+6m^2n+4m^3n+m^4n^2}$$

was used with an effective modulus E_{sub} for the Parylene+Cr+Au composite substrate. E_{sub} was determined by the transformed section method and the parallel-axis theorem to determine the moment of inertia for a composite area [1, 2]. In the transformed section method, the widths of the layers in the composite beam are adjusted to create an imaginary beam composed of only one material, in our case Au. The layer thicknesses for the Parylene, Cr, and Au were h_{Pa} , h_{Cr} , and h_{Au} respectively. (The beam width w cancels out).

The width ratios are given by n_i :

$$(17) \quad n_1 = \frac{E_{Cr}}{E_{Au}}, \quad n_2 = \frac{E_{Pa}}{E_{Au}}$$

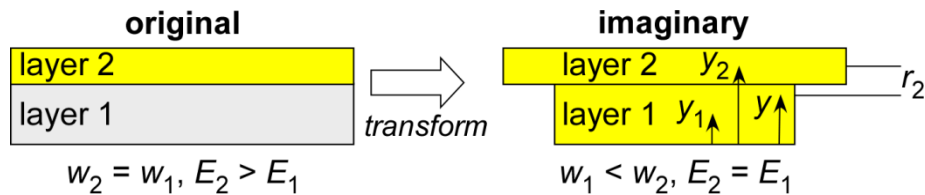


Figure 3-4. Beam cross-sections illustrating the transformed section method for a 2-layer beam. (Figure credit E. Smela.)

Next, the parallel-axis theorem is used to determine the moment of inertia for the imaginary beam. The moment of inertia I_{yi} of a layer with respect to the plane going

through its center of mass is equal to the moment of inertia I'_{yi} with respect to any parallel plane plus the product of the area A_i and the square of the distance r_i between the two planes. The moment of inertia of a composite beam I_y is the sum of the moments of inertia of all the layers with respect to the same reference plane.

$$(18) \quad I_y = \sum_{i=1}^n I_{yi} = \sum_{i=1}^n I'_{yi} + A_i \cdot r_i^2$$

where $r_i = y_i - y$ and y is the position of the reference plane. We choose to place the reference plane at the centroid (geometric center) of the imaginary beam, a distance y from the bottom of the beam, given by:

$$(19) \quad y = \frac{\sum_{i=1}^n y_i A_i}{\sum_{i=1}^n A_i} = \frac{h_{Au} \left(h_{Cr} + h_{Pa} + \frac{h_{Au}}{2} \right) + n_1 \cdot h_{Cr} \left(h_{Pa} + \frac{h_{Cr}}{2} \right) + n_2 \cdot h_{Pa} \left(\frac{h_{Pa}}{2} \right)}{h_{Au} + n_1 \cdot h_{Cr} + n_2 \cdot h_{Pa}}$$

where y_i is the centroid of each layer and A_i is the cross-sectional area (thickness*width) of each transformed layer.

Substituting Equation (8) for every layer into equation y, I_y is given as:

$$(20) \quad I_y = w \left(\begin{aligned} & \frac{1}{12} h_{Au}^3 + h_{Au} \left(h_{Cr} + h_{Pa} + \frac{h_{Au}}{2} - y \right)^2 + \frac{1}{12} n_1 \cdot h_{Cr}^3 \\ & + n_1 \cdot h_{Cr} \left(h_{Pa} + \frac{h_{Cr}}{2} - y \right)^2 + \frac{1}{12} n_2 \cdot h_{Pa}^3 + n_2 \cdot h_{Pa} \left(y - \frac{h_{Pa}}{2} \right)^2 \end{aligned} \right)$$

The composite substrate equivalent stiffness $(EI)_{sub}$ is obtained by multiplying the Young's modulus E of the reference layer, here E_{Au} , by I_y .

$$(21) \quad (EI)_{sub} = E_{Au} \cdot I_y$$

The moment of inertia of the imaginary beam is I_{sub} .

$$(22) \quad I_{sub} = \frac{1}{12} w \cdot (h_{Au} + h_{Cr} + h_{Pa})^3$$

E_{sub} is finally obtained by dividing the equivalent stiffness $(EI)_{sub}$ by I_{sub} .

$$(23) \quad E_{sub} = \frac{(EI)_{sub}}{I_{sub}}$$

Equation (23) can now be substituted into equation (16) to obtain the deflection due to the actuation moment.

3.2.3 Composite beam stiffness

In section 3.2.2, the transformed section method was used to calculate the effective substrate stiffness and Young's moduli for the cantilever beam substrate layers (Parylene+Cr+Au) in order to solve for the deflection due to the actuation moment. In equation (14) the deflection due to the weight acts on the bilayer composite including the PPy layer. Therefore, a new model is established for all four layers using the transformed section method with the PPy layer as the reference. A new equivalent cross section and distance to the centroid, relative to the bottom, is given as y_2 .

$$(24) \quad \text{let } n_3 = \frac{E_{Au}}{E_{PPy}}, \quad n_4 = \frac{E_{Cr}}{E_{PPy}}, \quad n_5 = \frac{E_{Pa}}{E_{PPy}}$$

$$y_2 = \frac{h_{PPy} \left(h_{Au} + h_{Cr} + h_{Pa} + \frac{h_{PPy}}{2} \right) + n_3 \cdot h_{Au} \left(h_{Cr} + h_{Pa} + \frac{h_{Au}}{2} \right) + n_4 \cdot h_{Cr} \left(h_{Pa} + \frac{h_{Cr}}{2} \right) + n_5 \cdot h_{Pa} \left(\frac{h_{Pa}}{2} \right)}{h_{PPy} + n_3 \cdot h_{Au} + n_4 \cdot h_{Cr} + n_5 \cdot h_{Pa}}$$

The equivalent composite stiffness is determined similar as methods described in section 3.2.2.

$$(25) \quad (EI)_{comp} = E_{PPy} \cdot w \left(\frac{1}{12} h_{PPy}^3 + h_{PPy} \left(h_{Au} + h_{Cr} + h_{Pa} + \frac{h_{PPy}}{2} - y_2 \right)^2 + \right.$$

$$\left. \frac{1}{12} n_3 \cdot h_{Au}^3 + n_3 \cdot h_{Au} \left(h_{Cr} + h_{Pa} + \frac{h_{Au}}{2} - y_2 \right)^2 + \frac{1}{12} n_4 \cdot h_{Cr}^3 + n_4 \cdot \right.$$

$$\left. h_{Cr} \left(h_{Pa} + \frac{h_{Cr}}{2} - y_2 \right)^2 + \frac{1}{12} n_5 \cdot h_{Pa}^3 + n_5 \cdot h_{Pa} \left(y_2 - \frac{h_{Pa}}{2} \right)^2 \right)$$

3.2.4 Solving for ϵ_{act}

Assuming E_{PPy} for a device with known dimensions, weight, measured deflection, the actuation strain ϵ_{act} can be solved for using equation (15), by substituting in equations (23) and (25).

3.2.5 Design parameters

The design of the device dimensions can be tailored in multiple ways to accommodate a range of actuation strain and moments. The useful region of interest is ϵ_{act} in the linear range of elasticity under stress, which should result in uniform curvature. The device's substrate stiffness, beam length, and weight at the tip can be changed independently to span the expected range of actuation moment and residual stress. Using equation (16) for expected beam curvature from CP bilayer actuators with an initial ϵ_{act} , allows for identifying the optimal thickness ratio for a given substrate stiffness for maximum deflection.

CP thickness

The thickness range of the CPs determines the first limitation of the design space. CP's used for bio-sensors and coatings are typically submicron [3-5], however, thicker films are needed for micro-actuators to produce any substantial work. The polymer strength increases monotonically with thickness; however, for bilayer actuators a very thick layer of polymer will prevent the beam from bending effectively [6]. Therefore, multiple models have been developed defining the optimal polymer-to-substrate ratio for bending actuators [6-8]. Characterization of CPs for actuators has typically been done with

thicker films between 10-25 μm with either flexible substrate materials such as parylene, KaptonTM film, or free-standing [8-13].

The thin film assumption simplifies the mechanical behavior of beams; however, it requires that the contribution of the film to the rigidity of the film/substrate combination is negligible. This does not hold true for the larger thickness ratios of interest.

Material properties

Substrate materials used neural electrode devices span orders of magnitude range of hardness. Typical materials include Silicon (160 GPa), Parylene or Kapton (~ 3 GPa), and polydimethylsiloxane (PDMS) (~ 2 MPa) (Dow Corning). The Parylene-C was chosen for this device. The Young's modulus E_{pa} for Parylene-C was reported by the manufacturer [14] to be 2.76 GPa, but another reports places it between 3.0-3.2 GPa [15] and a third as high as 4.75 GPa [16]. The manufacturer's value was used for this work. The bulk modulus for Au of $E_{Au} = 83$ GPa was used here, although the value for thin film gold has been reported as differing from this [7, 17]. The Cr adhesion layer is generally ignored, but it was thicker than usual on these beams (150 \AA) and the Young's modulus E_{Cr} of Cr is high, ranging from 86 GPa up to 279 GPa in bulk Cr [18], so it may significantly contribute to the composite thickness. However, thin film deposited Cr has a reported value of 180 GPa [19]. Therefore, the conservative value of 180 GPa was used for this work. An approximate actuation strain of 1% was used in the model to design the device dimensions and PPy thickness to obtain working devices.

Beam dimensions and weight

Ideally the substrate thickness could be increased alone or the material it is comprised of could be exchanged to maintain device dimensions and span a range of stiffnesses, however, this would complicate the fabrication process. Assuming the approximate polymer modulus and actuation strain based on previous studies allows us to use existing models to predict expected bending behavior given the substrate stiffness. The following figures assume $E_{PPy} = 450$ MPa, $\epsilon_{act} = 1\%$, $E_{Pa} = 2.76$ GPa, $h_{Pa} = 21$ μm , $E_{Au} = 83$ GPa, $h_{Au} = 1000$ \AA , $E_{Cr} = 180$ GPa, and $h_{Cr} = 100$ \AA .

Substrate thickness was held constant for comparing the curvature to Young's moduli for different materials in Figure 3-5. However, less thickness would be needed to achieve the same stiffness for devices made from materials with higher moduli. With a PPy(DBS) thickness of 21 μm and 1:1 substrate thickness ratio (chosen to match experimental values), the curvature drops off for very soft and very hard materials.

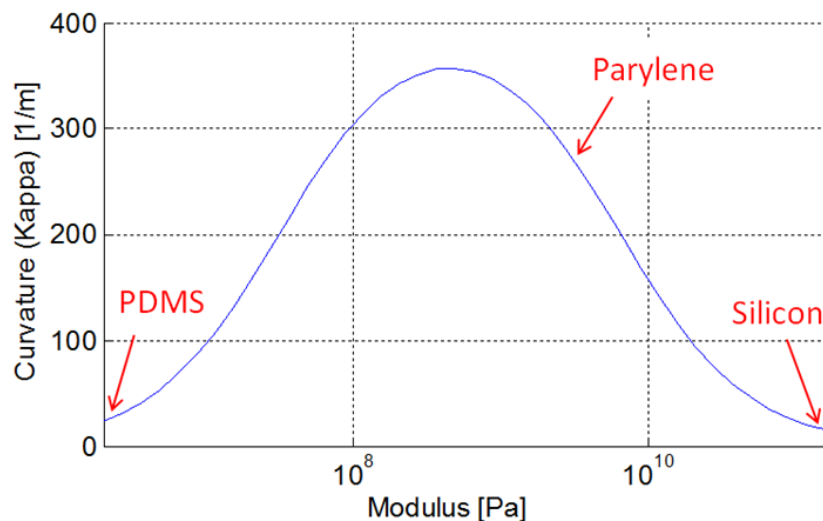


Figure 3-5. Bilayer curvature modeled as a function of E_{sub} (2 MPa – 160 GPa) with $h_{PPy} = 21$ μm . The arrows indicate the approximate Young's moduli for three types of materials used in neural interfaces. (Code provided by E. Smela, written by A. Nacev)

Parylene was used for these devices, therefore, its thickness was fixed and the thickness of PPy(DBS) was varied between 1-100 μm . Figure 3-6 shows the curvature as a function of PPy thickness, where the maximum was found at a PPy-to-substrate thickness ratio of 1.3.

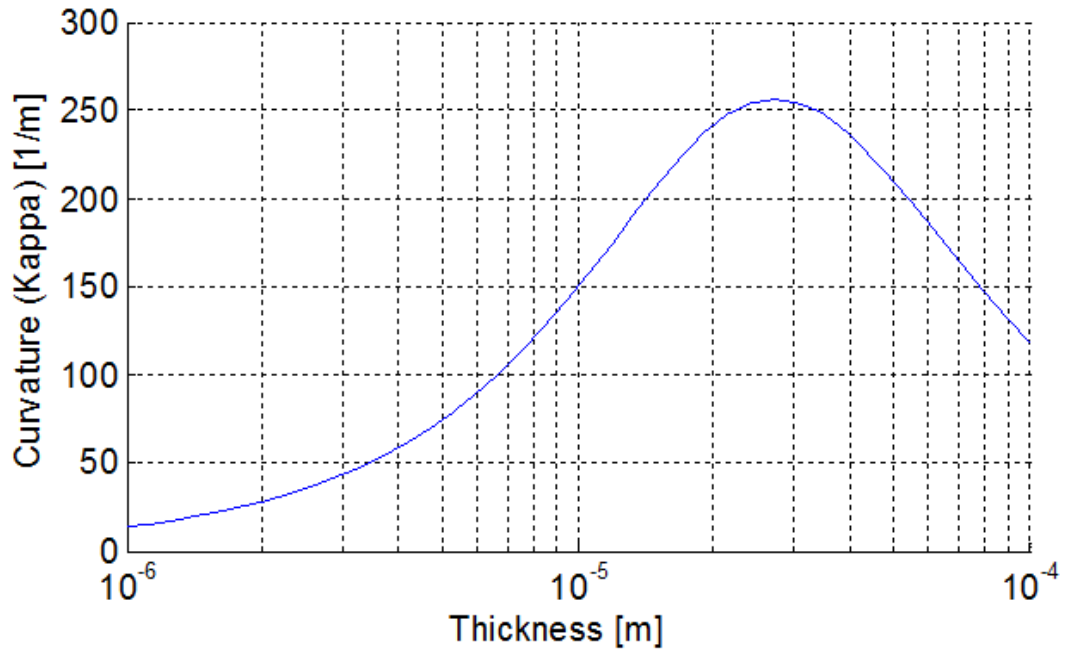


Figure 3-6. Bilayer curvature modeled as a function of h_{PPy} assuming Parylene as the substrate. The maximum curvature was at $h_{PPy} = 27.3 \mu\text{m}$, resulting in $h_{PPy}/h_{sub} = \sim 1.3$. (Code provided by E. Smela written by A. Nacev)

Using equation (15) the beam tip deflection was plotted as a function of PPy thickness in Figure 3-7; assuming a beam length of 10 mm, width of 1000 μm , and varying amount of point force due to the weight. Devices are assumed to be supported on a substrate, therefore, deflection less than 0 mm is excluded. The maximum deflection was effectively the same with an opposing force of 10 μN . By increasing the opposing force to 100 μN , the maximum deflection decreased by about 20% and occurred at an increased PPy thickness of about 10 μm . With 1000 μN of force applied, the expected deflection dramatically decreased and only plateaued at the maximum PPy thickness. These results

indicate that the minimum potential range of opposing tip force that decreases the maximum deflection without substantially shifting the PPy thickness is between 10-100 μN .

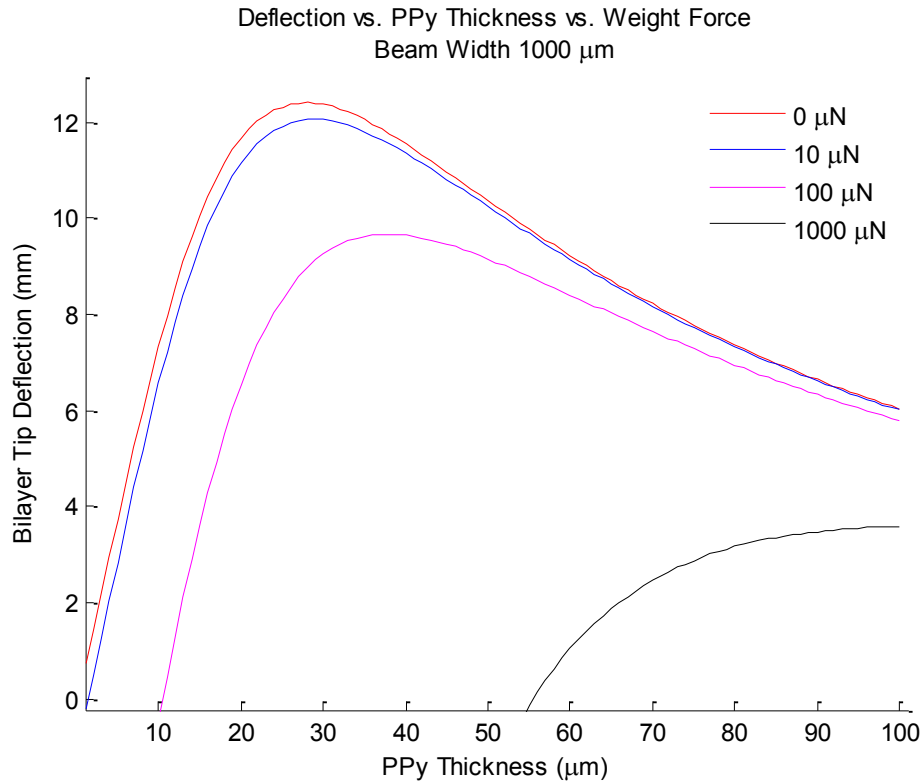


Figure 3-7. Positive bilayer tip deflection modeled as a function of h_{PPy} (1 - 100 μm), with beam length = 10 mm, beam width = 1000 μm , and varied opposing point force at the tip = 0, 10, 100, 1000 μN . Devices are assumed to be supported on a substrate, therefore, deflection less than 0 mm is excluded. In Figure 3-8, the beam tip deflection

was plotted as a function of PPy thickness, with an opposing tip force of 50 μN ; assuming a beam length of 10 mm, and varying widths of 200, 400, 600, 800, and 1000 μm . The widest beam resulted in the greatest deflection and peaked at the lowest PPy thickness relative to the smaller widths. A large decrease in maximum deflection occurred between widths of 400 μm and 200 μm , with the peak also shifted for greater amount of PPy thickness.

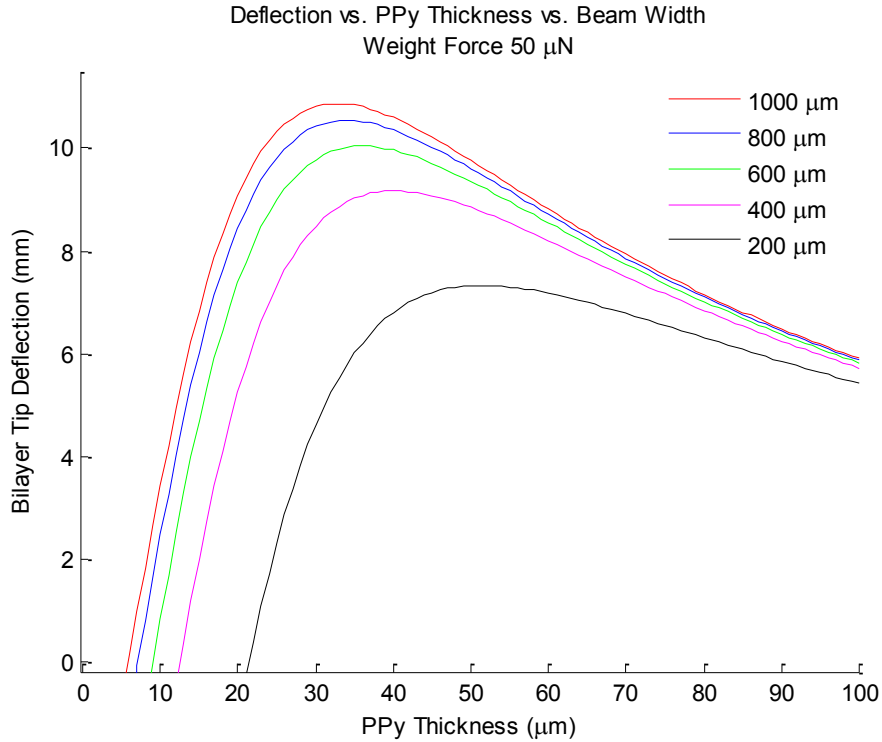


Figure 3-8. Positive bilayer tip deflection modeled as a function of h_{PPy} (1 - 100 μm) and beam length = 10 mm, beam widths 200 - 1000 μm , with opposing 50 μN point force at the tip.

3.2.6 Residual stress

As mentioned in Chapter 1, from the perspective of the substrate, the polymer's tensile strain results in a compressive stress to the top of the substrate and similarly, the PPy's compressive strain results in a tensile stress to the top of the substrate. These stresses on the substrate can be determined by the cantilever deflection method used for quantifying residual stresses from deposited thin-films [20].

As described in [20] for a bilayer cantilever, σ is the residual stress, y is the neutral axis, δ is the deflection, L is the length, w is the width, h is the thickness, with subscripts PPy , sub , and $comp$ denote additional PPy, base and composite layers, respectively. E , M , and I denote Young's modulus, the bending moment, and the moment of inertia, respectively.

$$\text{let } n_6 = \frac{E_{PPy}}{E_{Sub}}$$

$$(26) \quad y_{comp} = \frac{\left(\frac{h_{sub}}{2}\right) h_{sub} + \left(\frac{h_{PPy}}{2}\right) \cdot n_6 \cdot h_{PPy}}{h_{sub} + n_6 \cdot h_{PPy}}$$

$$(27) \quad I_{comp} = I_{sub} + w_{sub} \cdot h_{sub} \left(y_{comp} - \frac{h_{sub}}{2}\right)^2 + I_{PPy} + n_6 \cdot w_{PPy} \cdot h_{PPy} \left(y_{comp} - \frac{h_{sub}}{2}\right)^2$$

$$(28) \quad M_{sub} = \frac{2E_{sub}}{L^2} I_{sub} \cdot \delta_{sub}, \quad M_{comp} = \frac{2E_{comp}}{L^2} I_{comp} \cdot \delta_{comp}$$

$$(29) \quad M_{comp} - M_{sub} = \sigma_{PPy} \cdot w_{PPy} \cdot h_{PPy} \left(h_{sub} + \frac{h_{PPy}}{2} - y_{comp}\right) - \sigma_{sub} \cdot w_{sub} \cdot h_{sub} \left(y_{comp} - \frac{h_{sub}}{2}\right)$$

$$(30) \quad \sigma_{PPy} = \frac{\left(\frac{2E_{sub}}{L^2}\right)(I_{comp} \cdot \delta_{comp} - I_{sub} \cdot \delta_{sub}) + \sigma_{sub} \cdot w_{sub} \cdot h_{sub} \left(y_{comp} - \frac{h_{sub}}{2}\right)}{w_{PPy} \cdot h_{PPy} \left(h_{sub} + \frac{h_{PPy}}{2} - y_{comp}\right)}$$

Assuming there is no initial stress on the beam ($\sigma_{sub} = 0$) there will be no initial deflection ($\delta_{sub} = 0$).

$$(31) \quad \sigma_{PPy} = \frac{\left(\frac{2E_{sub}}{L^2}\right) \cdot (I_{comp} \cdot \delta_{comp})}{w_{PPy} \cdot h_{PPy} \left(h_{sub} + \frac{h_{PPy}}{2} - y_{comp}\right)}$$

The calculation of the residual stress σ_{PPy} on the substrate requires accounting for the opposing deflection due to the weight δ_{weight} . While the actuation strain bends the beam up (+), the weight of the mass opposes this deflection (-) due to gravity. Therefore, δ_{act} is used for the effective composite deflection δ_{comp} , which is the net measured deflection δ_{Tot} , minus the opposing deflection due to the weight δ_{weight} .

$$(32) \quad \delta_{comp} = \delta_{act} = \delta_{Tot} - \delta_{weight}$$

Since δ_{weight} is a negative value, the effective δ_{act} will be larger than the measured δ_{Tot} .

3.3 Materials and Methods

3.3.1 Fabrication

Two series of devices were fabricated. The first generation was described in [21]. The fabrication process for the second generation is overviewed in Figure 3-9. Devices were fabricated using standard photolithography techniques (Lurie Nanofabrication Facility, University of Michigan).

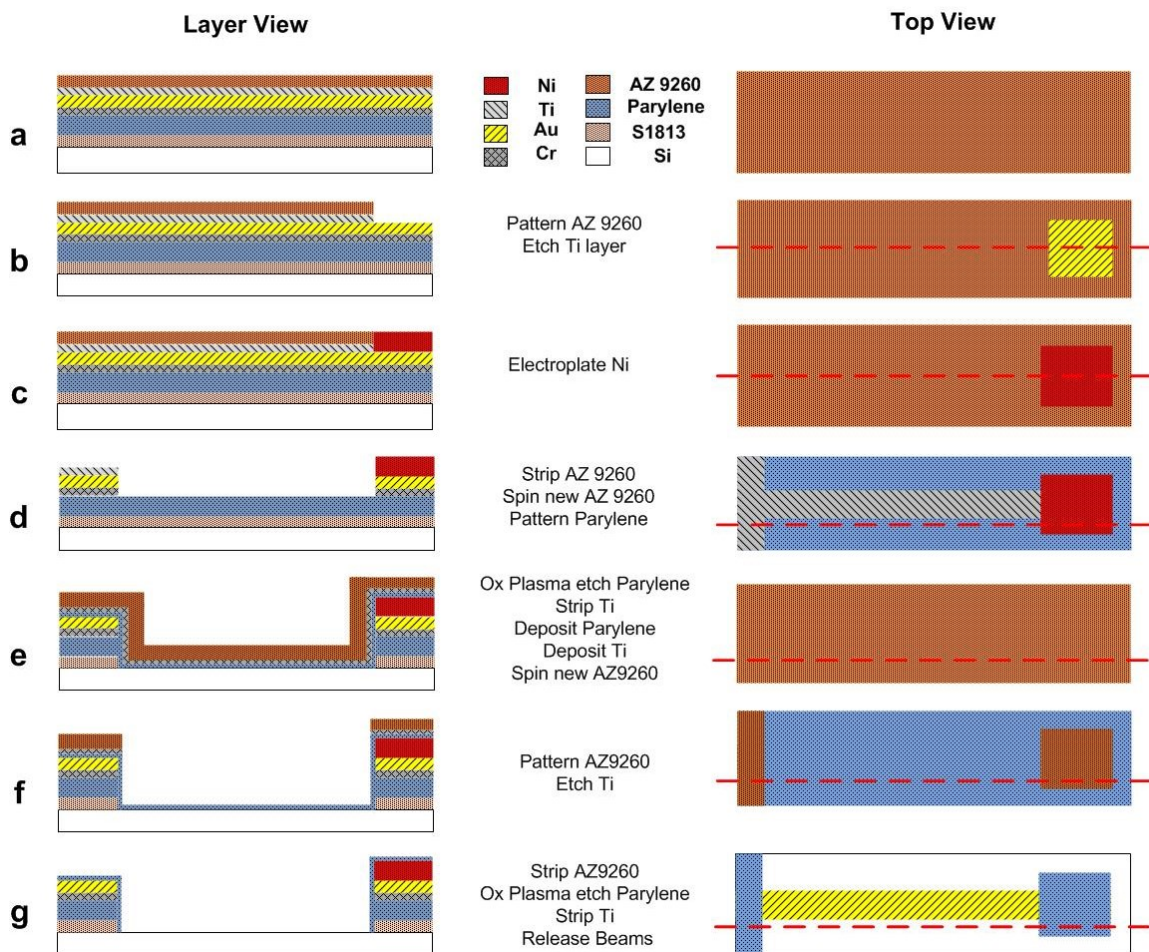


Figure 3-9. Fabrication process overview.

(Figure 3-9a) As the final release layer, photoresist (Shipley 1813, AZ Electronic Materials, Branchburg, NJ) was spin-coated onto a 4" silicon wafer and baked at 95 °C for 90 minutes. Parylene C was deposited (PDS 2035, Specialty Coating Systems,

Indianapolis, IN), and after an oxygen plasma clean (PlasmaTherm 790, 150 mT, 99 sccm O₂, 100 W, 30 sec), chromium (Cr, 100 Å), gold (Au, 1000 Å), and titanium (Ti, 1000 Å) were evaporated (Enerjet Evaporator, 2 μT, 10 Å/sec) onto the Parylene. A thick photoresist layer of AZ 9260 (MicroChemicals, Germany) was spun on (2000 RPM for 2 sec, laid flat for stabilization for 10 min, soft baked at 85 °C for 30 min then at 115 °C for 2 min, reabsorption of water for 30 min).

(Figure 3-9b) The AZ9260 resist was exposed using a Cr/glass mask (1500 mJ/cm² for 220 sec (MA 6 Mask Aligner)), and patterned (allowed to settle 10 min, developed in 400K:Di (1:4) with regular agitation) to define the mold for the electroplating of the nickel weights. The Ti layer exposed by the mold openings were wet etched using a mixture of DI, HF, and H₂O₂ (20:1:1). The depths of the mold trenches (also the AZ 9260 thickness) were measured with a surface profilometer (Dektak 6 M, Veeco Instruments Inc., Plainview, NY) as a reference for determining the Ni thickness during plating.

(Figure 3-9c) On the edge of the wafer, a small corner (~4 mm²) of the top photoresist was manually removed using acetone for electrical connection. The wafer was connected to the anode of a power generator using an alligator clip and immersed in Ni plating solution. The solution was heated to 50 °C and was continually stirred by a magnetic stir bar. A 9 mm x 9 mm Ni plate was immersed parallel to the wafer and connected to the cathode. The electroplating waveform applied is shown in Figure 3-10. A reverse current was applied to mitigate sidewall edge effects, which result in plating at a more rapid rate (unpublished Lurie Nanofabrication Facility standard operating procedure for Ni Electroplating by Pilar Herrera-Fierro, March 2008). The mold trenches were

intermittently measured to monitor the Ni thickness. Plating concluded when the targeted thickness was met.

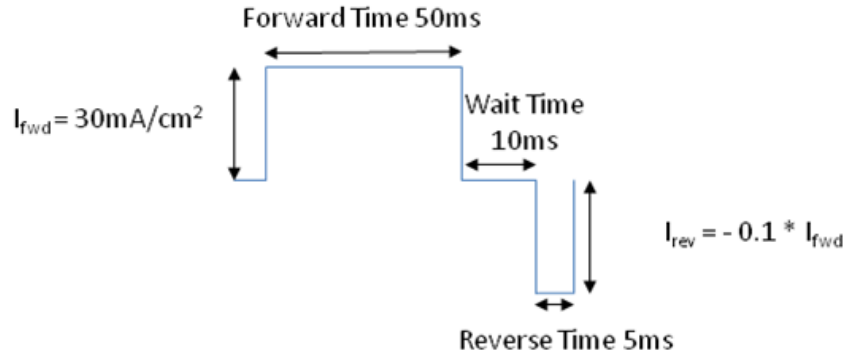


Figure 3-10. Electroplating waveform used in electroplating the nickel weights.

(Figure 3-9d) The AZ 9260 layer was stripped and Ni weight thicknesses were measured across the middle of two sides of their square shapes. Weight volume was calculated as this profile thickness multiplied by the length of another side. The weights were designed to be in the middle of the range of forces that the beams were expected to exert (weight volume $4.83 \text{ E-}04 \text{ cm}^3$, nickel density 19.3 g/cm^3 , calculated force $93 \text{ }\mu\text{N}$).

(Figure 3-9e) A second AZ 9260 photoresist was spun and patterned with a mask to define the metal and beam shapes. The metal layers were patterned by wet etching (Ti etch mixture DI, HF, and H_2O_2 (20:1:1), Transene TFA Au etchant, CR-14 Cr etchant). The Parylene was dry etched using an oxygen plasma (conditions as above, 200 nm/min etch rate). The Ti layer was stripped and an insulating layer of Parylene was deposited. A new AZ 9260 layer was spun.

(Figure 3-9f) The AZ 9260 layer was exposed and patterned using a new mask defining the insulation areas. The exposed Ti layer was etched.

(Figure 3-9g) The AZ 9260 layer was stripped and the exposed Parylene was etched. The Ti layer was stripped, which also resulted in the undercut of the initial resist release layer. Released devices were rinsed in isopropyl alcohol and DI water, and were transferred to glass slides.

A set of MEMS tip-weighted conjugated polymer bilayer actuator devices consisting of $20.8 \pm 0.9 \mu\text{m}$ thick Parylene, 100/1000 Å Cr/Au, and electroplated Ni weights, listed in Table 3-1, were successfully fabricated. Each device had five beams that were electrically connected and therefore polymerized together.

Polymerization

PPy(DBS) was polymerized galvanostatically (at constant current) to a thickness of $11.3 \pm 0.8 \mu\text{m}$ (individual thicknesses are listed in Table 3-2) onto the Au surface in a solution of deionized (DI) water, 0.1 M pyrrole (Aldrich), and 0.1 M NaDBS (Aldrich) using a galvanostat/potentiostat (Ecochemie Autolab PGStat 12). The deposition current density was 1 mA/cm^2 . Polymerizing at higher currents has been shown to reduce actuation strain [22-24]. Thickness was estimated based on consumed charge [25]. A porous carbon counter electrode and Ag/AgCl reference electrode (Bioanalytical Systems Inc.) were used during polymerization. Samples were rinsed in DI water and allowed to dry at ambient conditions for at least 24 hours. Parylene and PPy thicknesses were measured using SEM images (Philips XL30ESEM) of beam cross-sections. Devices were stored in closed Petri dishes lined with cleanroom paper wipes. Images of the resulting device are shown in Figure 3-11. Devices remained flat after polymerization.

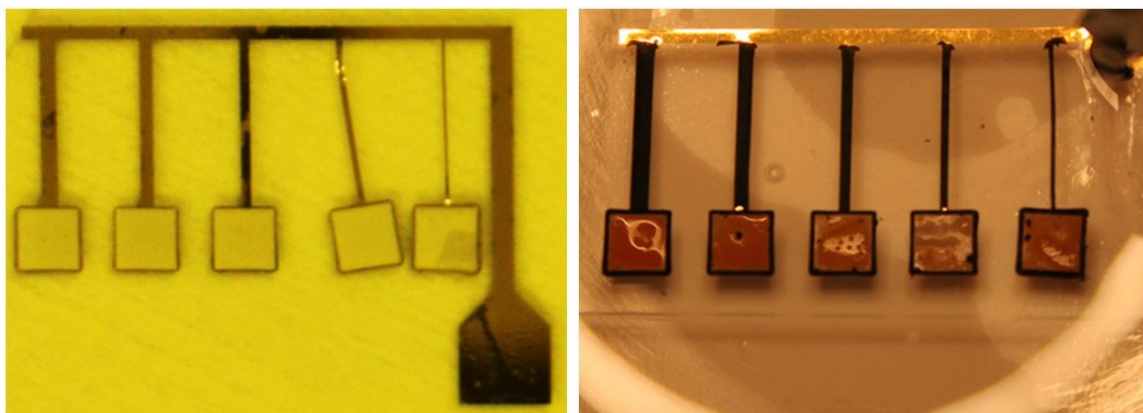


Figure 3-11. (Left) Fabricated weighted bilayer device with thickness of 21 μm Parylene, 100/1000 \AA Cr/Au, lengths of 10 mm, and widths of 1000, 800, 600, 400, and 200 μm . (Right) Device from the left polymerized with PPy(DBS).

The edges of the Ni weights also showed polymerization, indicating a failure of the Parylene insulation layer. To further insulate the Ni weights, a thin layer of photoresist (Shipley 1813) was manually applied using a paint brush and allowed to dry for 48 hours (resulting in the orange color).

3.3.2 Experimental setup

Immersed in solution, devices were connected to the working electrode of a galvanostat/potentiostat (Ecochemie Autolab PGStat 12) with an Ag/AgCl reference electrode (Bioanalytical Systems Inc.) and a 1x1" platinum foil used as a counter electrode. Videos of actuation were recorded (Canon EOS Ti1) and images were extracted. Deflections were quantified using device dimensions for calibration. After testing was complete, the weights were cut off using a razor blade at the beam end and measured on a digital microscale (AG204, Mettler Toledo Inc.). Forces required to produce the resulting curvatures were calculated.

3.4 Results

3.4.1 Residual stress is sufficient to bend beams and lift weights

Devices were cycled from 0 V to -1.0 V vs Ag/AgCl at 10 mV/s in 0.1 M NaDBS at RT, a solution in which the actuation strain of PPy(DBS) is known. Beam deflections from three trials were obtained from still images captured from video and are listed in Table 3-1. Devices with smaller weights were lifted by all beams, which resulted in bending greater than 90°, such as in Figure 3-12. These devices were excluded since the force due to the weight would increase the curvature rather than decrease it. Devices with weights that were too large did not produce any movement and were also excluded. Figure 3-13 shows alternate views of a device with weighted beams that resulted in bending between these extremes.

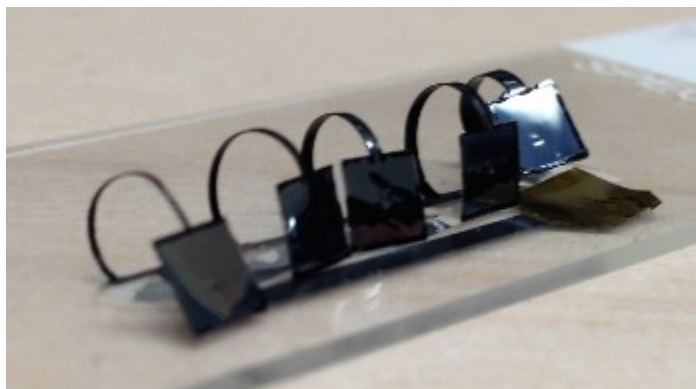


Figure 3-12. Image of a device in air (PPy was fully dried) with full curvature that was excluded.

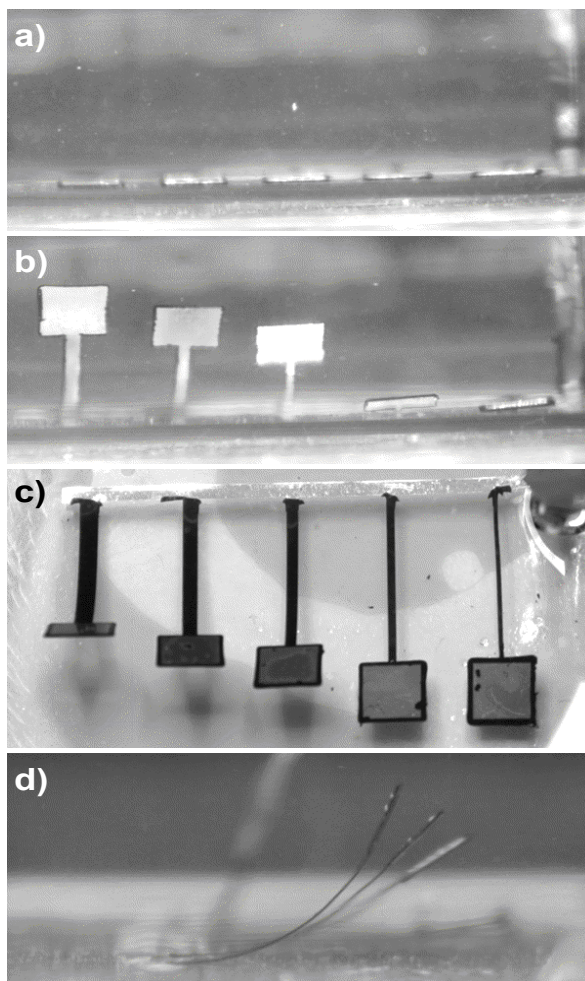


Figure 3-13. Images of weighted bilayer beams after the initial actuation cycle residual stress builds up. a) Horizontal view showing the devices laying flat when reduced (-1.0 V). b) Horizontal, c) top, and d) side views of the devices lifting when oxidized (0 V).

The effect of the initial priming cycle can be seen by comparing the right image in Figure 3-11, taken prior to cycling (at 0 V) and Figure 3-13a when reduced (at -1.0 V). After the initial priming cycle, the devices lift up during oxidation, when the Na hydrated ions leave the polymer.

3.4.2 Cycling in NaDBS and aCSF

After repeated actuation cycles and consistent deflection, the solution was replaced with aCSF solution heated at 37 °C, and new CVs were taken until the I-V curves stabilized; between solutions the samples were rinsed in deionized water. Representative deflections in both solutions are shown in Figure 3-14. The point at which the weight connected to the beam was considered to be the tip of the bilayer.

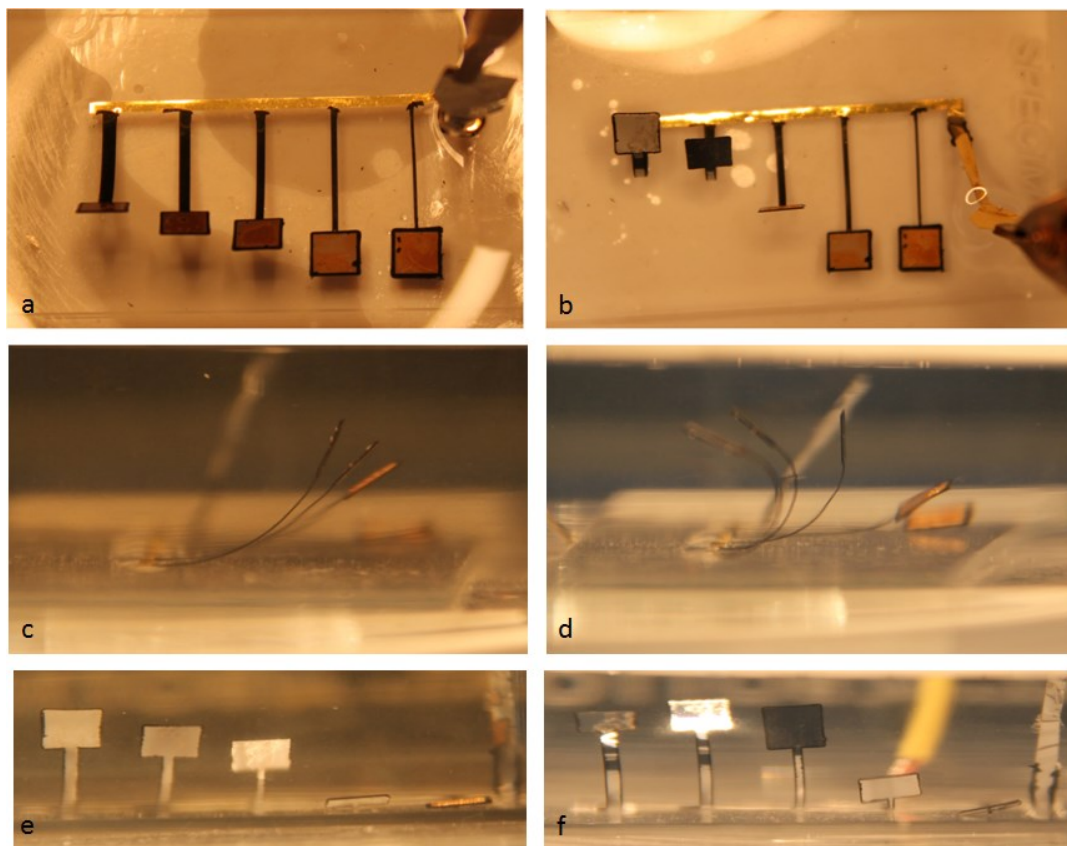


Figure 3-14. Actuated devices in NaDBS at 22 °C (a,c,e) and in aCSF at 37 °C (b,d,f). (Top) overhead view; (Middle) inline side view; (Bottom) parallel side view.

Beam deflections and weights of the samples are listed in Table 3-1. As expected, the wider bilayers produced greater deflections. Consistent with the previous deflection data, when the samples were cycled in aCSF at 37 °C they deflected more than in NaDBS at RT [26].

Table 3-1. Average deflections from three scans of a set of devices and weight mass with (*) indicating bending greater than 90° and (-) indicating no bending observed. Mass force was corrected for buoyancy.

Beam Width (μm)	Thickness ratio PPy/Sub	Deflection (mm)		Mass Weight (mg)	Mass Force (μN)
		NaDBS at RT	aCSF at 37°C		
1000	1.34	4.84 ± 0.49	*	5.3	46.1
800	1.17	4.08 ± 0.44	*	5.0	43.5
600	1.28	3.09 ± 0.49	5.17 ± 0.57	4.7	40.9
400	1.33	0.6^\dagger	1.88 ± 0.65	5.0	43.5
200	2.07	-	-	6.5	56.5

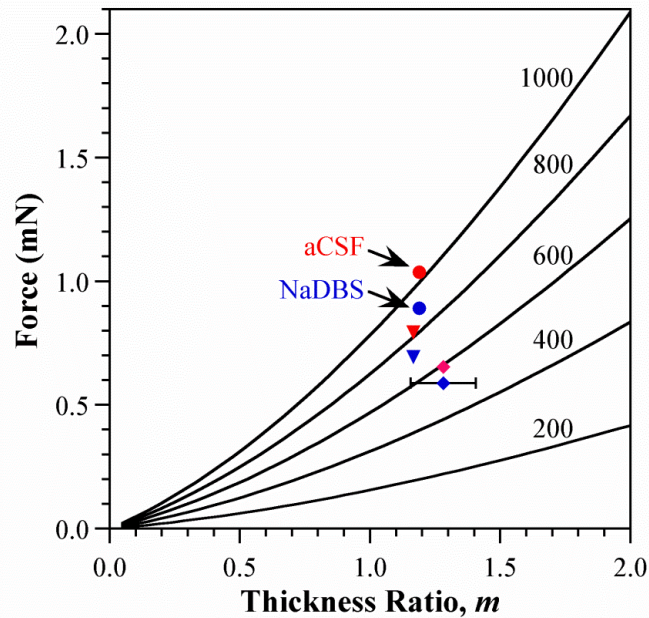


Figure 3-15. Model prediction (lines) of bilayer actuation force as a function of thickness ratio m for $\alpha_{PPy} = 0.03$, $h_{sub} = 21 \mu\text{m}$, $n = 0.14$, $L = 10 \text{ mm}$, and $w = 200, 400, 600, 800,$ and $1000 \mu\text{m}$. Actuation forces calculated from the data in Table 3-1 (blue points, NaDBS, red points, aCSF). Experimental uncertainty in the thickness was $5 \mu\text{m}$, shown by the error bar.

For the bilayers having widths of 200 and 400 μm , the force was already greater than what the model predicted the beams could exert; they were not expected to deflect and did not. The experimental data and the predicted forces showed good agreement. This model will therefore allow the design of neural probe actuators with desired forces and deflections, a powerful tool for future work.

3.4.3 Calculation of PPy actuation strain

A summary of device dimensions and calculated stiffness using equations from section 3.2.1, are compiled in Table 3-2.

Table 3-2. Summary of device dimensions and calculated values

Dimensions of Weighted Bilayer Devices						
Width (μm)		1000	800	600	400	200
Length (m)		10.0E-3	10.0E-3	10.0E-3	10.0E-3	10.0E-3
Thickness (m)	PPy	28.1E-6	24.5E-6	26.9E-6	28.0E-6	43.5E-6
	Base Layer	20.8E-6	20.8E-6	20.8E-6	20.8E-6	20.8E-6
	Au	150.00E-9	150.00E-9	150.00E-9	150.00E-9	150.00E-9
	Cr	15.00E-9	15.00E-9	15.00E-9	15.00E-9	15.00E-9
Young's Moduli (Pa)	Base	2.76E+9	2.76E+9	2.76E+9	2.76E+9	2.76E+9
	Au	83.0E+9	83.0E+9	83.0E+9	83.0E+9	83.0E+9
	Cr	180.0E+9	180.0E+9	180.0E+9	180.0E+9	180.0E+9
	PPy(Ox)	450.0E+6	450.0E+6	450.0E+6	450.0E+6	450.0E+6
n1	Eau/Eppy	184.44	184.44	184.44	184.44	184.44
n2	Ecr/Eppy	400.00	400.00	400.00	400.00	400.00
n3	Epa/Eppy	6.13	6.13	6.13	6.13	6.13
n4	Ecr/Eau	2.17	2.17	2.17	2.17	2.17
n5	Epa/Eau	0.03	0.03	0.03	0.03	0.03
Effective Substrate	Thickness (m)	20.97E-6	20.97E-6	20.97E-6	20.97E-6	20.97E-6
	Young's Moduli (Pa)	4.41E+9	4.41E+9	4.41E+9	4.41E+9	4.41E+9
Neutral Axis (m)	y1 (Composite)	15.92E-6	15.31E-6	15.71E-6	15.90E-6	18.99E-6
	y2 (Substrate)	12.59E-6	12.59E-6	12.59E-6	12.59E-6	12.59E-6
$k = E*w*t^3 / (4*L^3)$ r	kppy	2.50E-3	1.32E-3	1.31E-3	987.84E-6	1.85E-3
	ksub	10.16E-3	8.12E-3	6.09E-3	4.06E-3	2.03E-3
	ksub/kppy	4.07	6.14	4.64	4.11	1.10
Stiffness (N/m)	Composite	9.63E-9	6.41E-9	5.43E-9	3.83E-9	4.09E-9
	Substrate	3.39E-9	2.71E-9	2.03E-9	1.35E-9	677.02E-12
	PPy	832.05E-12	441.18E-12	437.96E-12	329.28E-12	617.35E-12
Moment of Inertia	Composite	358.2E-18	765.5E-18	313.9E-18	148.3E-18	157.4E-18
	Substrate	767.9E-21	614.3E-21	460.7E-21	307.2E-21	153.6E-21
	PPy	1.8E-18	980.4E-21	973.3E-21	731.7E-21	1.4E-18
Weight Force, F_w (N)	(Buoyancy corrected)	46.1E-6	43.5E-6	40.9E-6	43.5E-6	56.5E-6

3.4.4 Calculation of residual stress

The method for calculating the residual stress σ_{PPy} on the substrate is discussed in section 3.2.5. The results using equations (31) and (32), measured deflections in Table 3-1, and beam dimensions in Table 3-2 are listed in Table 3-3.

Table 3-3. Beam deflections with (*) indicating bending greater than 90° and (-) indicating no bending observed, and calculation of σ_{PPy} .

Beam Width (μm)		1000	800	600	400	200
δ due to F_W (m)		-1.60E-3	-2.26E-3	-2.51E-3	-3.78E-3	-4.61E-3
δ measured (m)	NaDBS at RT	4.84E-3	4.08E-3	3.09E-3	600.00E-6	-
	aCSF at 37 °C	*	*	5.17E-3	1.88E-3	-
δ due to ϵ_{act} (m)	NaDBS at RT	6.44E-3	6.34E-3	5.60E-3	4.38E-3	
	aCSF at 37 °C			7.68E-3	5.66E-3	
Residual Stress (Pa)	NaDBS at RT	378.67E+6	1.22E+9	513.06E+6	268.24E+6	
	aCSF at 37 °C			703.70E+6	346.59E+6	

3.5 Conclusions

This work introduced a new method for measuring conjugated polymer actuation forces on the micro-scale, in an aqueous solution. A MEMS tip-weighted conjugated polymer bilayer actuator was designed, fabricated, and tested. A corresponding model was developed to quantify actuation forces and residual stress. Initial experimental results indicated that forces corresponded with 1% actuation strain, similar as found in the work described in Chapter 2. Cycling at 37 °C resulted in greater bending, also similar as found in the work in Chapter 2. While a greater number of devices need to be tested to draw conclusions on scientific trends, it is clear that this device is capable to acquire the data needed.

3.6 Supplemental Information

3.6.1 Novel method to measure conjugated polymer Young's modulus and actuation strain

A comparison of at least two devices with either different dimensions (widths or thicknesses) or weights, resulting in differential bending moments and deflection, may allow for calculation of the CP Young's modulus and actuation strain using a system of equations. Assuming constant actuation strain ε_{act} , for a given set of devices with known, but modified dimensions and/or weight, the measured deflections and weights can be used to solve equation (15), by substituting in equations (23) and (25), to solve a system of equations with two unknowns ε_{act} and E_{PPy} .

$$(33) \quad \delta_{TotA} = \delta_{actA} + \delta_{weightA} \quad \& \quad \delta_{TotB} = \delta_{actB} + \delta_{weightB}$$

The system of equations (15), (16), and (25) were solved using Mathematica 8 software (Wolfram Research). The results are listed in Sup. Table 3-1. The combination of samples cycled in NaDBS at RT with widths of 1000 μm and 800 μm resulted in a E_{PPy} value of 450 MPa matching that of previously reported value of 450 ± 55 MPa for oxidized PPy(DBS) [27, 28]. The remaining combinations either did not result in a combination of real values or was substantially different the previously reported values.

There are several potential explanations for failure of this method to solve for a match. First, the error in measuring the layer thicknesses may have been significant. Secondly, as mentioned above, this method assumes that the actuation strain and Young's moduli are identical in both devices. Delamination of PPy may have occurred on some devices, which would decrease the actuation strain. Lastly, as shown in Figure 3-8, the maximum

deflection shifts slightly as a function PPy thickness for the different widths, and greater differences were expected between the smaller widths, as compared to the 1000 μm and 800 μm beams that resulted in a match.

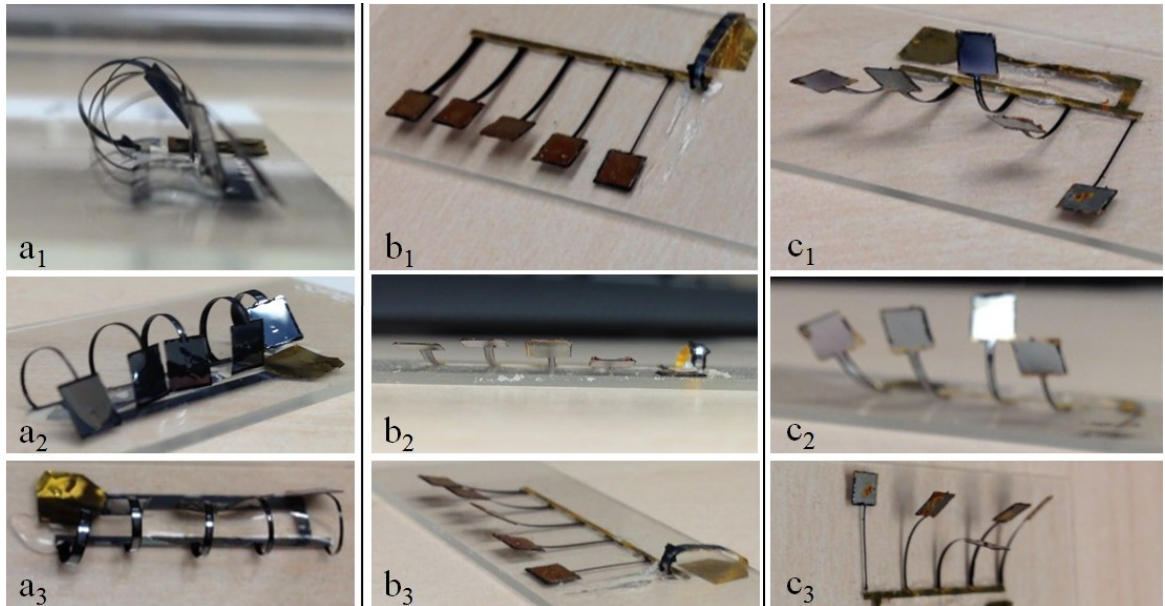
Sup. Table 3-1 PPy oxidized Young's modulus and actuation strain calculated from sample combinations cycled in NaDBS at RT.

Sample Combination (Beam Widths)	<i>ϵ_{act}</i>	<i>E_{PPy}</i>
1000 μm & 800 μm	0.51%	450 MPa
1000 μm & 600 μm	0.99%	136 MPa
800 μm & 600 μm	-0.09%	-428 MPa

3.6.2 Excluded devices

Sup. Table 3-2 Excluded devices having variable width

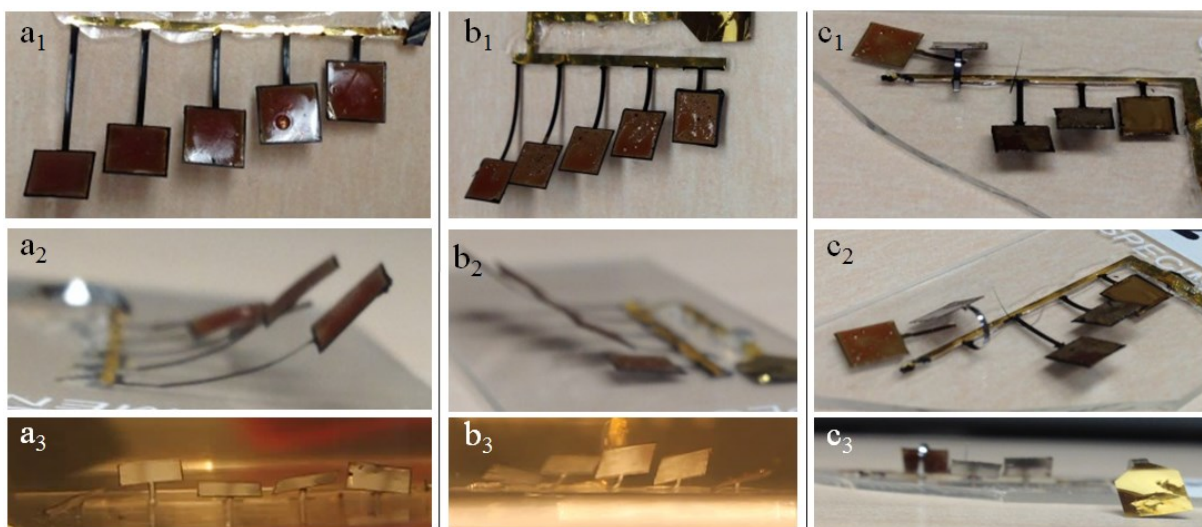
Wafer	Device	Lengths (um)	Widths (um)	Parylene thickness (μm)	Estimated Weight (mg)	Force W (μN)	Average F (μN)	Polymerization Charge (C)	Estimated Thickness Ratio
NG1	D1	10000	200	22.0	10.2	100			
NG1	D2	10000	400	22.0	7.9	77			
NG1	D3	10000	600	22.0	7.2	71	76	2.56	2 to 1
NG1	D4	10000	800	22.0	6.6	65			
NG1	D5	10000	1000	22.0	7.1	70			
NG3	D1	10000	200	22.4	24.0	235			
NG3	D2	10000	400	22.4	19.4	191			
NG3	D3	10000	600	22.4	18.9	185	214	1.28	1 to 1
NG3	D4	10000	800	22.4	20.8	204			
NG3	D5	10000	1000	22.4	26.2	257			
NG3	D6	10000	200	22.4	11.8	115			
NG3	D7	10000	400	22.4	11.5	113			
NG3	D8	10000	600	22.4	11.2	110	126	1.28	1 to 1
NG3	D9	10000	800	22.4	12.9	126			
NG3	D10	10000	1000	22.4	17.1	167			



Sup. Figure 3-1 Excluded devices with variable widths (a₁-a₃) NG1 D1-5, (b₁-b₃) NG3 D1-5, (c₁-c₃) NG3 D6-10.

Sup. Table 3-3 Excluded devices having variable length

Wafer	Device	Lengths (um)	Widths (um)	Parylene thickness (μm)	Estimated Weight (mg)	Force W (μN)	Average F (μN)	Polymerization Charge (C)	Estimated Thickness Ratio
NG2	C1	2000	500	20.8	11.2	109			
NG2	C2	4000	500	20.8	8.5	83			
NG2	C3	6000	500	20.8	7.8	77	87	1.28	1 to 1
NG2	C4	8000	500	20.8	7.7	75			
NG2	C5	10000	500	20.8	9.3	91			
NG2	C6	2000	500	20.8	10.5	102			
NG2	C7	4000	500	20.8	9.8	96			
NG2	C8	6000	500	20.8	9.8	96	111	1.28	1 to 1
NG2	C9	8000	500	20.8	10.9	107			
NG2	C10	10000	500	20.8	15.4	151			
NG3	C1	2000	500	22.4	24.5	240			
NG3	C2	4000	500	22.4	16.1	158			
NG3	C3	6000	500	22.4	14.4	141	170	0.86	0.5 to 1
NG3	C4	8000	500	22.4	13.9	136			
NG3	C5	10000	500	22.4	17.7	173			



Sup. Figure 3-2 Excluded devices with variable lengths (a₁-a₃) NG2 C1-5, (b₁-b₃) NG2 C6-10, (c₁-c₃) NG3 C1-5.

3.6.3 Stiffness ratios from referenced bilayer papers

Sup. Table 3-4. Values used to determine stiffness ratios in referenced bilayer papers

	Reference	2010 Lin	2004 Careem	2004 Careem	2001 Maw
	Base Material	Kapton	Polyimide	Polyimide	Kapton
Length (m)		20.0E-3	20.0E-3	20.0E-3	15.0E-3
Width (m)		1.0E-3	5.0E-3	5.0E-3	1.0E-3
	PPy	9.12E-6	1.00E-6	3.00E-6	10.0E-6
	Base Layer	25.0E-6	25.0E-6	25.0E-6	25.4E-6
Thickness (m)	Au	200.00E-9	25.00E-9	25.00E-9	35.0E-9
	Cr	000.00E+0	000.00E+0	000.00E+0	000.0E+0
	Base	3.00E+9	3.00E+9	3.00E+9	3.00E+9
Young's Moduli (Pa)	Au	83.0E+9	83.0E+9	83.0E+9	83.0E+9
	Cr	180.0E+9	180.0E+9	180.0E+9	180.0E+9
	PPy(Ox)	450.0E+6	450.0E+6	450.0E+6	450.0E+6
n1	Eau/Eppy	184.44	184.44	184.44	184.44
n2	Ecr/Eppy	400.00	400.00	400.00	400.00
n3	Epa/Eppy	6.67	6.67	6.67	6.67
n4	Ecr/Eau	2.17	2.17	2.17	2.17
n5	Epa/Eau	0.04	0.04	0.04	0.04
	Thickness (m)	25.20E-6	25.03E-6	25.03E-6	25.44E-6
Composite	Young's moduli (Pa)	4.55E+9	3.23E+9	3.23E+9	3.32E+9
	y1 (composite)	15.43E-6	12.91E-6	13.07E-6	14.10E-6
Neutral Axis (m)	y2 (substrate)	14.78E-6	12.84E-6	12.84E-6	13.17E-6
	Kppy	10.7E-6	70.3E-9	1.9E-6	33.3E-6
$k = E*w*t^3 / (4*L^3)$	Ksub	2.3E-3	7.9E-3	7.9E-3	4.0E-3
r	ksub/kppy	213.18	112596.58	4170.24	121.32
	Composite	7.0E-9	21.5E-9	22.4E-9	5.9E-9
Stiffness (N/m)	Substrate	6.1E-9	21.1E-9	21.1E-9	4.5E-9
	PPy	28.4E-12	187.5E-15	5.1E-12	37.5E-12

3.7 References

- [1] J. M. Gere and S. P. Timoshenko, Mechanics of Materials, 4th ed. (PWS-KENT Publishing Company, Boston, 1997).
- [2] W. C. Young, Roark's formulas for stress & strain, 6th ed. (McGraw-Hill, Inc., 1989).
- [3] X. Cui, J. F. Hetke, J. A. Wiler, D. J. Anderson, and D. C. Martin, "Electrochemical deposition and characterization of conducting polymer polypyrrole/PSS on multichannel neural probes," *Sensors and Actuators A: Physical*, 93, 8-18, 2001.
- [4] M. R. Abidian and D. C. Martin, "Experimental and theoretical characterization of implantable neural microelectrodes modified with conducting polymer nanotubes," *Biomaterials*, 29, 1273-1283, 2008.
- [5] A. Gelmi, M. J. Higgins, and G. G. Wallace, "Physical surface and electromechanical properties of doped polypyrrole biomaterials," *Biomaterials*, 31, 1974-1983, 2010.
- [6] B. Shapiro and E. Smela, "Bending actuators with maximum curvature and force and zero interfacial stress," *J. Intel. Mat. Syst. Str.*, 18, 181-186, 2007.
- [7] M. Christophersen, B. Shapiro, and E. Smela, "Characterization and modeling of PPy bilayer microactuators - Part 1. Curvature," *Sens. Act. B*, 115, 596-609, 2006.
- [8] P. Du, X. Lin, and X. Zhang, "A multilayer bending model for conducting polymer actuators," *Sensors and Actuators A-Physical*, 163, 2010.
- [9] M. J. M. Jafeen, M. A. Careem, and S. Skaarup, "Speed and strain of polypyrrole actuators: dependence on cation hydration number," *Ionics*, 16, 1-6, 2010.
- [10] U. L. Zainudeen, M. A. Careem, and S. Skaarup, "PEDOT and PPy conducting polymer bilayer and trilayer actuators," *Sens. Act. B*, 134, 467-470, 2008.
- [11] L. Bay, N. Mogensen, S. Skaarup, P. Sommer-Larsen, M. Jorgensen, and K. West, "Polypyrrole doped with alkyl benzenesulfonates," *Macromolecules*, 35, 9345-9351, 2002.
- [12] J. D. Madden, D. Rinderknecht, P. A. Anquetil, and I. W. Hunter, "Creep and cycle life in polypyrrole actuators," *Sens. Act. A*, 133, 210-217, 2007.
- [13] M. A. Careem, K. P. Vidanapathirana, S. Skaarup, and K. West, "Dependence of force produced by polypyrrole-based artificial muscles on ionic species involved," *Solid State Ionics*, 175, 725-728, 2004.
- [14] *Specialty Coating Systems SCS Parylene Properties*, 2010, (Accessed: 11/8/2011), Available: <http://www.scscoatings.com/docs/coatspec.pdf>.

- [15] J. P. Seymour and D. R. Kipke, "Fabrication of polymer neural probes with Sub-cellular features for reduced tissue encapsulation," *Conf. Proc. IEEE Eng. Med. Biol. Soc.*, New York, vol. 1, (August 30-September 3, 2006).
- [16] C. Y. Shih, T. A. Harder, and Y. C. Tai, "Yield strength of thin-film parylene-C," *Microsyst. Technol.*, 10, 407-411, 2004.
- [17] V. K. Pamula, A. Jog, and R. B. Fair, "Mechanical property measurement of thin-film gold using thermally actuated bimetallic cantilever beams," *Nanotech.*, 1, 410-413, 2001.
- [18] J. Lintymer, N. Martin, J. M. Chappe, J. Takadoum, and P. Delobelle, "Modeling of Young's modulus, hardness and stiffness of chromium zigzag multilayers sputter deposited," *Thin Solid Films*, 503, 177-189, 2006.
- [19] K. E. Petersen and C. R. Guarnieri, "Young's modulus measurements of thin films using micromechanics," *J. Appl. Phys.*, 50, 6761-6766, 1979.
- [20] Y. H. Min and Y. K. Kim, "In situ measurement of residual stress in micromachined thin films using a specimen with composite-layered cantilevers," *J. Micromech. Microeng.*, 10, 314-321, 2000.
- [21] E. D. Daneshvar, E. Smela, and D. R. Kipke, "Mechanical characterization of conducting polymer actuated neural probes under physiological settings," *Proc. SPIE Smart Struct. Mater. (EAPAD)*, San Diego, vol. 7642, 1T.1-1T.10, edited by Y. Bar-Cohen (March 7-11, 2010).
- [22] S. Maw, E. Smela, K. Yoshida, P. Sommer-Larsen, and R. B. Stein, "The effects of varying deposition current density on bending behaviour in PPy(DBS)-actuated bending beams," *Sens. Act. A*, 89, 175-184, 2001.
- [23] S. Skaarup, K. West, B. Zachaustriansen, M. A. Careem, and G. K. R. Senadeera, "Electrolyte and ion memory effects in highly conjugated polypyrrole," *Solid State Ionics*, 72, 108-114, 1994.
- [24] K. West, T. Jacobsen, B. Zachaustriansen, M. A. Careem, and S. Skaarup, "Electrochemical synthesis of polypyrrole - Influence of current-density on structure," *Synth. Met.*, 55, 1412-1417, 1993.
- [25] E. Smela, "Microfabrication of PPy microactuators and other conjugated polymer devices," *J. Micromech. Microeng.*, 9, 1-18, 1999.
- [26] E. D. Daneshvar and E. Smela, "Characterization of conjugated polymer actuation under cerebral physiological conditions (Accepted)," *Adv. Healthcare Mater.*, 2014.

- [27] L. Bay, T. Jacobsen, S. Skaarup, and K. West, "Mechanism of actuation in conducting polymers: Osmotic expansion," *J. Phys. Chem. B*, 105, 8492-8497, 2001.
- [28] G. M. Spinks and V. T. Truong, "Work-per-cycle analysis for electromechanical actuators," *Sensors and Actuators A-Physical*, 119, 2005.

CHAPTER 4 Navigating conjugated polymer actuated neural probes in a brain phantom

This Chapter is published as is in the SPIE Smart Structures and Materials: Electroactive Polymer Actuators and Devices conference proceedings, (March 12-15, 2012, San Diego) titled “Navigating conjugated polymer actuated neural probes in a brain phantom.” Co-author Professor Elisabeth Smela, University of Maryland, contributed significantly to the data analysis.

Abstract

Neural probe insertion methods have a direct impact on the longevity of the device in the brain. Initial tissue and vascular damage caused by the probe entering the brain triggers a chronic tissue response that is known to attenuate neural recordings and ultimately encapsulate the probes. Smaller devices have been found to evoke reduced inflammatory response. One way to record from undamaged neural networks may be to position the electrode sites away from the probe. To investigate this approach, probes with controllably movable electrode projections, which would move outside of the zone that is damaged by the insertion of the larger probe, are being developed. The objective of this study was to test the capability of conjugated polymer bilayer actuators to actuate neural electrode projections from a probe shank into a transparent brain phantom.

Parylene neural probe devices, having five electrode projections with actuating segments and with varying widths (50 – 250 μm) and lengths (200 – 1000 μm) were fabricated. The electroactive polymer polypyrrole (PPy) was used to bend or flatten the projections.

The devices were inserted into the brain phantom using an electronic microdrive while simultaneously activating the actuators. Deflections were quantified based on video images.

The electrode projections were successfully controlled to either remain flat or to actuate out-of-plane and into the brain phantom during insertion. The projection width had a significant effect on their ability to deflect within the phantom, with thinner probes deflecting but not the wider ones. Thus, small integrated conjugated polymer actuators may enable multiple neuro-experiments and applications not possible before.

4.1 Introduction

Brain machine interfaces (BMIs), such as neural probes, are devices that couple the brain with machines in order to control advanced prosthetics, treat neurological disorders, and make further advancements in the area of neuroscience [1]. One of the primary challenges in this area is placing recording electrode sites in healthy neural tissue. An implanted neural probe is detected as a foreign object by the brain, which initiates a complex reactive response, including glial cell reactivity, encapsulation, and silencing or damaging neurons close to the probe. These processes tend to cause neural signals to degrade and ultimately to fail [2]. Small, thinner projections from a neural probe shank elicit a less severe reactive response, including less encapsulation. Theoretically, this should result in higher signal quality and longer recording times [3]. Despite the less reactive response from minimally sized scaffold designs, the electrode sites will be still embedded into perturbed tissue where connections between neural networks in the brain have been cut.

Minimally-sized deployable projections with electrode sites at the tip may be an alternative way to mitigate the reactive response near the electrode by keeping existing neural connections mostly intact. Compared to electrode sites fixed on the surface of the probe, electrode sites at the ends of these electrode projections are expected to be surrounded the minimal amount of perturbed tissue and able to record from the surrounding unperturbed neuronal network. A passive spring-loaded approach to deploying electrode sites is currently being investigated [4]. As shown in Figure 4-1b, small-area electrode projections may be actuated during probe insertion away from the probe shank (i.e. base substrate) and into healthy tissue outside of the anticipated encapsulation layer. Such active moveable electrode projections may also be used to control the proximity of the electrodes to healthy neurons after implantation. Polypyrrole actuators have several advantages over other types of actuators, including biocompatibility [5-8], low power consumption, compatibility with neural probe fabrication, and small size.

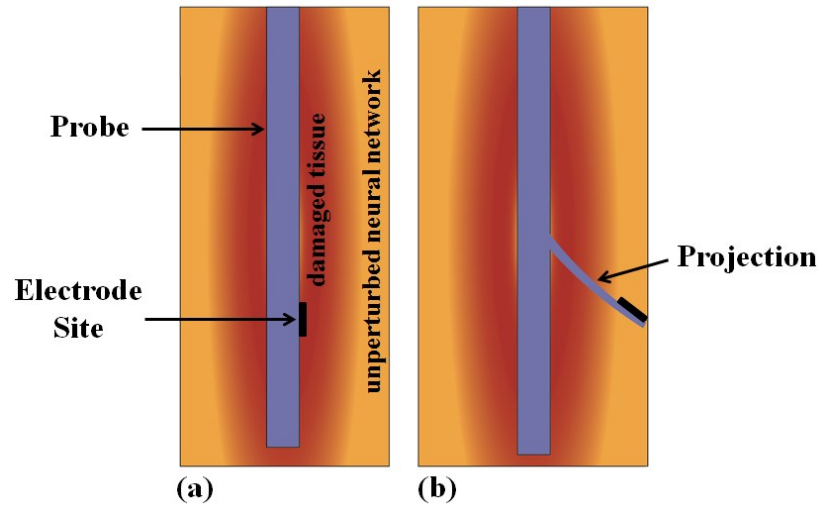


Figure 4-1. Side view of (a) a standard neural probe and (b) a neural probe with an electrode projection. Damaged tissue surrounds the larger probe in both designs, but smaller projections are expected to cause less damage [3, 9].

Insertion dynamics of penetrating substrates such as probes and needles into quasi-solid volumes is an active area of research. Multiple critical parameters of implantable devices influence the forces, trajectory, and dynamics of insertion. Generally there are three insertion forces that predominate: normal reaction, friction, and cutting [10]. The normal reaction forces are experienced before puncture of the tissue and can lead to buckling, depending on the stiffness of the tissue and the device, and the geometric shape of the device. Frictional forces occur between the interfacing materials, and cutting forces relate to the ability to slice through the tissue. Tip shape and angle, which directly affect the cutting force, have been repeatedly shown to influence the insertion forces in brain matter and other tissues [10-12]. In addition, the symmetry in tip geometry influences the amount of deflection during insertion [10]. To avoid deflection, symmetry is preferred, while asymmetry can be used to promote greater deflection. Other factors such as insertion speed and insertion method (manual vs. automated) have also been investigated for their effects on tissue damage due to rupture of blood vessels and interfacial stress

[13, 14]. The objective of this work was to identify the critical parameters that influence mechanical insertion of thin, narrow electrode projections and determine whether conjugated polymer actuators are capable of controlling the projection placement.

4.2 Methods

4.2.1 Stiffness to overcome insertion force

Insertion forces required to penetrate brain tissue are affected by the elasticity and moduli of the tissue and the device, as well as the interfacing geometry. Multiple studies have measured the force of neural probe penetration into brain tissue [11, 12, 15, 16] showing that for a given tissue type and insertion method, the force required for insertion increases linearly with insertion depth. The stiffness of the device must overcome these insertion forces to allow the device to reach the intended depth and avoid excessive buckling. The buckling load (or Euler's load) that the device can withstand is given by

$$(1) \quad P = \frac{K * \pi^2 * E * I}{L^2},$$

where P = buckling force threshold, K = column effective length factor (one pinned end, one fixed end) = 2.045, E = elastic modulus, I = area moment of inertia, and L = unsupported column length [15, 17]. The moment of inertia, I, for rectangular cross sections is given by

$$(2) \quad I = \frac{1}{12} * w * t^3,$$

where w = column width and t = column thickness. The buckling load varies as $t^3 * w / L^2$ [15]. Buckling can be prevented by increasing the thickness, increasing the width,

reducing the length, or a combination of all three. Applications for neural electrodes are not standardized; therefore, these parameters can be adjusted as needed. Theoretically, bilayer actuators exert greater force with increasing width [18]. Unloaded free deflection is invariant of beam width, but normal forces due to the tissue's resistance to compression will also increasingly oppose deflection with greater surface area. This tradeoff will be investigated with specially designed array of projections.

4.2.2 Device design and fabrication

Microfabricated neural probes have typically been made of silicon. However, recently several more flexible substrate materials, such as polyimide and parylene, have become popular [9, 19, 20]. For a lower substrate modulus, a thinner conducting polymer layer is able to deflect the beams. However, polymer substrates are susceptible to water absorption, which causes swelling, and swelling can lead to delamination of the overlying layers. Parylene C was chosen as the device substrate material due to its low modulus (~3 GPa for parylene C vs. 130 GPa for silicon) and because it has a lower water absorption than polyimide [21].

In this work, devices were designed having a base substrate supporting five electrode projections of the same length and thickness but varying widths (50, 100, 150, 200, 250 μm). Tip angle (opening angles) for all probe tips were 45° . The electrical traces to the actuating segments of all five devices were coupled together to ensure coordinated actuation, allowing the effect of projection width on insertion to be isolated.

Devices were fabricated using standard photolithography techniques at the Lurie Nanofabrication Facility at The University of Michigan. Photoresist (Shipley 1813, AZ

Electronic Materials, Branchburg, NJ) was spun onto a new silicon wafer and baked for 90 minutes to act as the probe release layer. A first parylene layer was deposited over the resist (PDS 2035, Specialty Coating Systems, Indianapolis, IN). A liftoff resist (SPR 220, Shipley Company, LLC, Marlborough, MA) was patterned for the recording electrode sites, traces, and contact pads. After an oxygen plasma clean, chromium (Cr), gold (Au), and titanium (Ti) were evaporated to thicknesses of 100 Å, 1000 Å, and 1000 Å. The metals were patterned by removing the liftoff resist in acetone (Figure 4-2a). A second layer of parylene was deposited to act as an insulating layer over the electrode sites. A second layer of Cr/Au was evaporated and patterned to define the actuator segments, electrical traces, and contact pads (Figure 4-2b). A third layer of parylene was deposited to insulate the actuator leads. In combination, these three parylene layers were ~25 μm thick. A thin layer of Ti (100 Å) was evaporated and patterned using a Ti wet etch (diluted hydrofluoric acid) to define the projection shape and electrode site opening (Figure 4-2c). This Ti layer also acted as an etch-stop for the final oxygen plasma etch of the all the parylene layers. A fourth and final parylene layer (10 μm) was deposited to further increase the probe thickness, while a final evaporated layer of Ti was patterned to define the probe shape. After oxygen plasma etching to remove the exposed parylene, the wafers were slowly dipped into Ti wet etch to remove the Ti mask. The devices were released from the wafer by soaking the wafers in acetone and dissolving the initial resist layer (Figure 4-2d). The released devices were rinsed in IPA and water and allowed to dry before use.

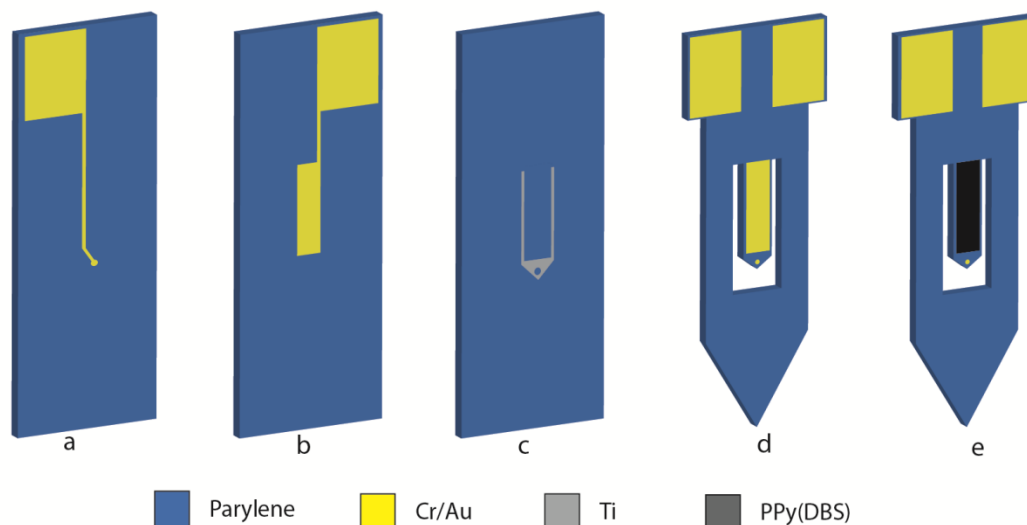


Figure 4-2. Overview of the fabrication of electrode projections on the probe. (a) Electrode sites and traces patterned with mask 1, (b) actuator areas and traces defined by mask 2, (c) etch-stop pattern for the projections using mask 3, and (d) device shape defined by mask 4. (e) PPy was polymerized post release. For clarity, only one of the five projections is shown.

4.2.3 Actuator polymerization

Polypyrrole was potentiostatically polymerized onto the actuator segments at 0.6 V in a solution of 0.1 M pyrrole (Aldrich) and 0.1 M dodecylbenzenesulfonate (DBS) (Aldrich) to varying thicknesses using an Autolab potentiostat (Ecochemie Autolab PGStat 12). An Ag/AgCl reference electrode and porous carbon counter electrode were used. PPy(DBS) thicknesses were estimated based on consumed charge [22]. Devices were cycled from 0 V to -1 V at 25 mV/s repeatedly until the I-V curves no longer varied. Devices were allowed to dry overnight prior to use.

4.2.4 Insertion and actuation method

The mechanism of actuation for conjugated polymer actuation has been described previously [23, 24]. Briefly, a potential of -1 V (electrochemical reduction) leads to

expansion of the polymer so that the projections lie flat, and a potential of 0 V (electrochemical oxidation) leads to contraction, bending the projections away from the probe.

A computer-controlled microdrive (Mercury C-862, Physik Instrumente, Karlsruhe, Germany) was used to drive the probe device into the phantom; it was manually coordinated with the actuation potential. A flat-tipped copper alligator clip attached to the end of the inserter was used to make electrical contact with the leads as well as to provide mechanical support. The insertion speed was held constant at 100 $\mu\text{m/s}$, which was found previously to be the optimal speed to reduce insertion forces during insertion into brain tissue [11]. As described in [25, 26], a 0.6% agarose gel brain phantom was used to mimic the mechanical consistency of brain tissue. Agarose gel allows ion transport, necessary for actuation of the PPy, and its transparency permits visualization of the motion of the devices. An Ag/AgCl reference electrode penetrated the agarose gel, and a platinum foil on the bottom of the dish was used as the counter electrode. A small amount of artificial cerebrospinal fluid [27] was added to the top of the gel brain phantom as an electrolyte to allow the actuators to be electrochemically oxidized or reduced, and 0 V was applied in order to flatten the projections prior to insertion.

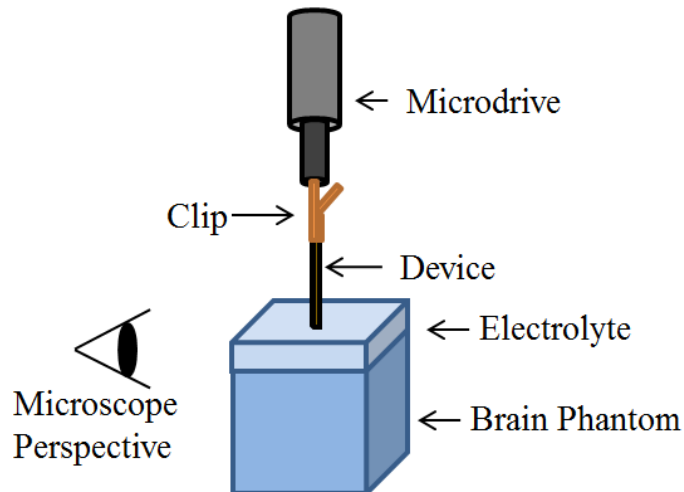


Figure 4-3. Electrodes were clamped to the end of the microdrive. The clip also acted as an electrical connection to the actuators. Artificial cerebrospinal fluid was used as the electrolyte to actuate the projections to lie flat prior to insertion.

4.3 Results

4.3.1 Acceptable designs to prevent buckling

Equations (1) and (2) showed that greater width and thickness increased probe stiffness, but larger projections may evoke a greater immune response. The design of the electrode projections thus required a tradeoff between small size and adequate stiffness during insertion. A linear average of the insertion forces vs. insertion depth were extracted from prior work [11, 12] and are plotted as a dotted red line in Figure 4-4. Free deflection at the tip was estimated from similar bilayer dimensions based on an established bilayer model [18, 28] and this is superimposed on the graph. Actuation force decreases with projection length, while free deflection increases with length. Acceptable designs require both enough force to overcome buckling and enough deflection to move outside of the anticipated immune response zone. Figure 4-4 shows the region of acceptable L and w under these constraints.

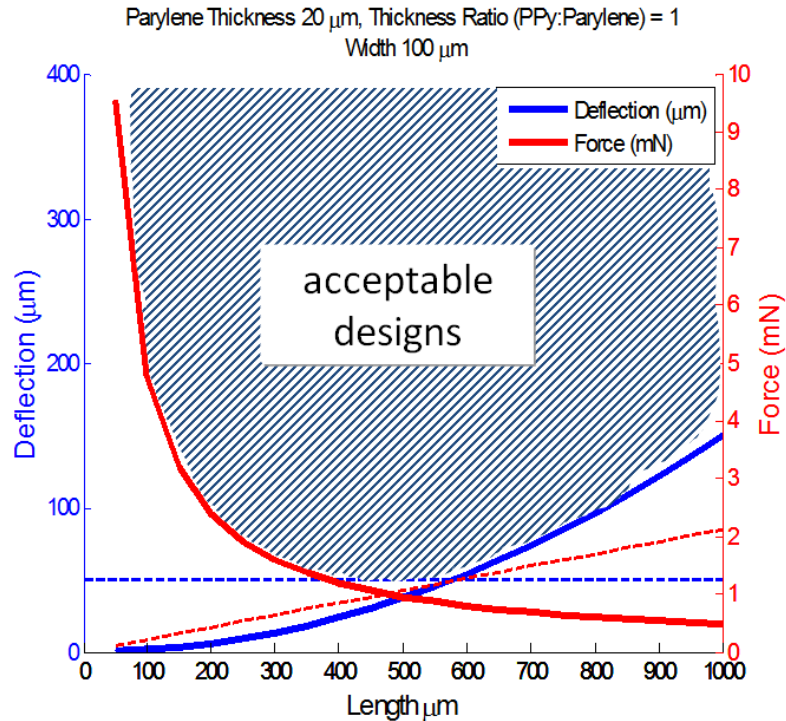


Figure 4-4. Calculated tip deflection and force vs. device length (for 20 μm thick PPy(DBS), 20 μm parylene). Force decreases with projection length, while deflection increases. Dotted red line: force required to insert the probe, which increases with insertion depth. Dotted blue line: 50 μm deflection needed to exit the encapsulation zone. Acceptable designs require both enough force and enough deflection.

4.3.2 Images of fabricated devices

The five projections on each device had the same lengths but varying widths in order to maintain identical insertion depths for comparison. Representative fabricated devices are shown in Figure 4-5. The zoomed-in image of an electrode site on a projection shows how the electrode site is electrically isolated from the actuating segment. This electrical isolation is essential for recording neural activity [29].

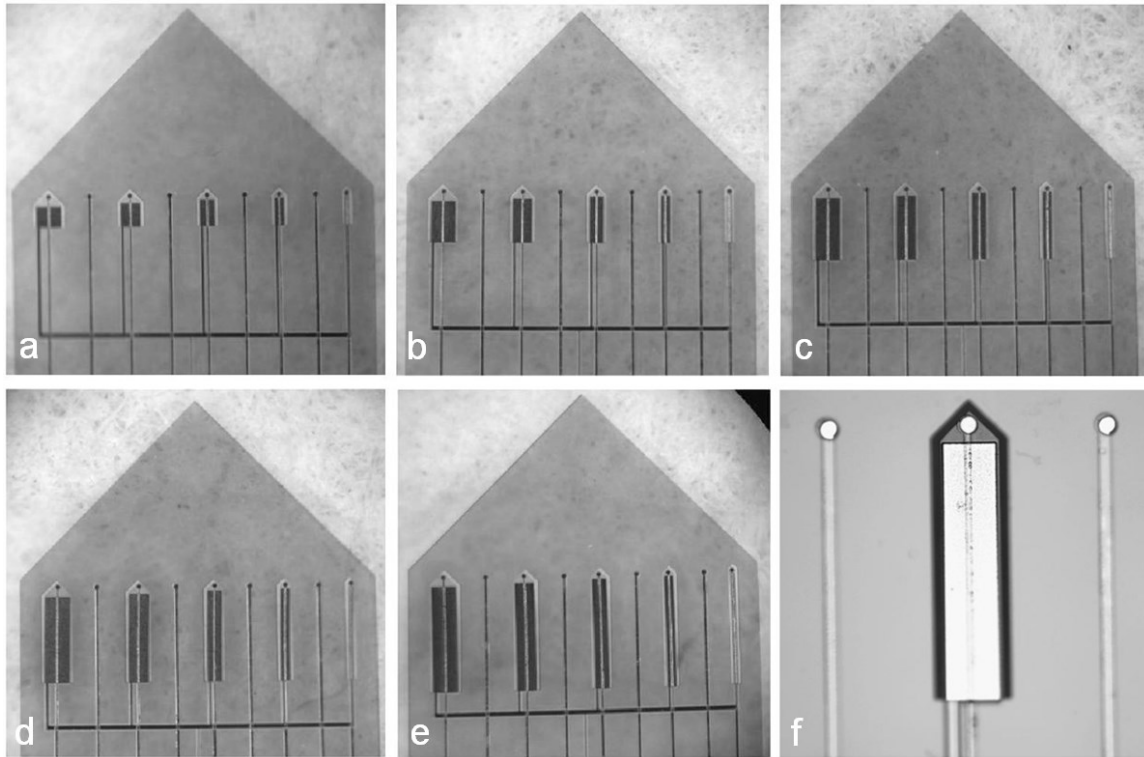


Figure 4-5. Images of devices with varying lengths (200-1000 μm) and widths (50-250 μm) prior to polymerization of PPy(DBS). Image (f) is zoomed in on a single projection in between two fixed electrode sites.

4.3.3 Electrode site impedances

Neural electrodes are used for recording action potentials from neurons as well as used for neural stimulation. Given the application, different electrode sizes and materials are chosen based on the selectivity or specificity needed [29]. Recording neural activity from individual neurons requires electrode sites small enough to be able to distinguish action potentials, yet large enough to detect potentials in the microvolt and millivolt range [30]. Smaller electrode sites improve the ability to discriminate between different neurons (selectivity), but they also have higher electrode impedance and thermal (background) noise [31]. Electrodes used for stimulation are typically larger so that they can transfer more charge without causing damage to the tissue. The electrode sites for these devices

were circular with a 20 μm diameter ($\sim 314 \mu\text{m}^2$), which would work well for recording purposes.

Electrode impedances are generally characterized by impedance spectroscopy, which measures the impedance magnitude and phase shift as a function of frequency. Action potentials typically occur at a frequency of approximately 1 kHz, and therefore the impedance value at this rate is most referenced [32]. Impedance spectroscopy was performed using a potentiostat (Ecochemie Autolab PGStat 12) in a two-electrode setup (a platinum foil was used as both the counter and reference electrode) in 1 M phosphate buffered saline. The average impedance spectroscopy results from nine electrode sites are shown in Figure 4-6. These impedance values closely match previously reported values for comparable electrode sites [33]. There were no significant differences between the fixed electrode sites and those on the projections ($N = 9$).

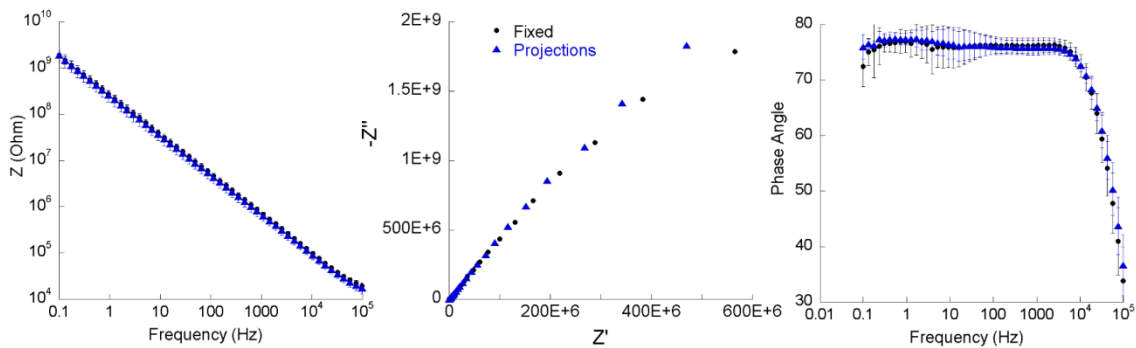


Figure 4-6. Impedance values of electrode sites as shown in a Bode magnitude plot (left), Nyquist plot (center), and Bode phase angle plot (right). Impedances of electrode sites fixed to the substrate and on the projections have similar values.

4.3.4 Articulated projections

Prior to insertion into the brain phantom, devices were actuated in 0.15 M NaDBS ten times to “prime” them. After this step, the electrode projections became bent out of plane

with no voltage applied. Next, devices were actuated ten times in artificial cerebrospinal fluid (aCSF), which matches the ionic composition of the brain. Images were taken from video of the electrode projections cycled in a bath of aCSF are shown in Figure 4-7. The sharp contrast difference at the electrode tip in Figure 4-7b is due to light reflected off the electrode site. This is an indication that the electrode site and polymerized actuator segment were successfully electrically insulated (otherwise the site would have been covered with a dark layer of PPy). Figure 4-7 also shows that the projections bent out of plane. The five projections in Figure 4-7c show similar free deflections, as expected, since curvature is independent of width [28]. The consistency of deflections indicates that the polymer thicknesses were similar and that there was appropriate spacing between the projections and the probe; if that gap is too small, lateral overgrowth of the PPy(DBS) can anchor the projection to the probe.

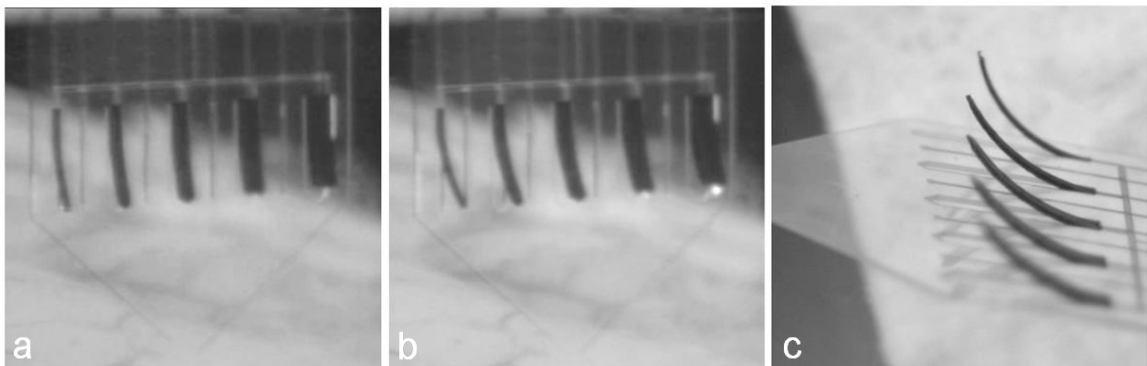


Figure 4-7. (a-b) Still images of devices in aCSF of an array of electrode projections of varying widths with sites (a) in plane, (b) actuated out of plane, showing light reflection off of the articulated electrode site. (c) Electrode projections removed from solution and deflected out of plane with no voltage applied.

4.3.5 Insertion and actuation into brain phantom

Devices were designed to isolate and compare the insertion dynamics of projections of varying width. Images from video of two devices being inserted into the brain phantom

are shown in Figure 4-8. The devices in images (a)-(c) have lengths of 1000 μm and those in (d)-(f) have lengths of 800 μm . Electrode projections were actuated at -1 V and were inserted straight for their full length as shown in images (a) and (b). This ability to straighten the projections is essential to reach deep insertion targets. Between images (b) and (c), the reduction potential was turned off and the device was advanced further to allow the projections to deflect out of plane. With a front viewing perspective, the actuation out of plane can only be seen in the narrowest beam. This beam is deflected out of plane and curls into a semi-circle. Since buckling of the beam wasn't observed, one can conclude that the stiffness was sufficient to allow the device to be advanced.

In Figure 4-8 images (d)-(f), projections were flattened as before. After 100 μm of insertion into the phantom, the projections were actuated out of plane and the device continued to be advanced. Compensating the deflections for the viewing angle in image (f), the estimated tip deflections for the projections with widths of 50 μm and 100 μm were ~ 772 μm and ~ 474 μm , respectively. The wider projections are expected to exert greater force, but they are also subject to greater normal (\perp) forces from the phantom due to their increased surface area. This multiple width device design was able to capture the cutoff point at which these forces are matched. Since the neural probe application requires smaller features, this was a good outcome.

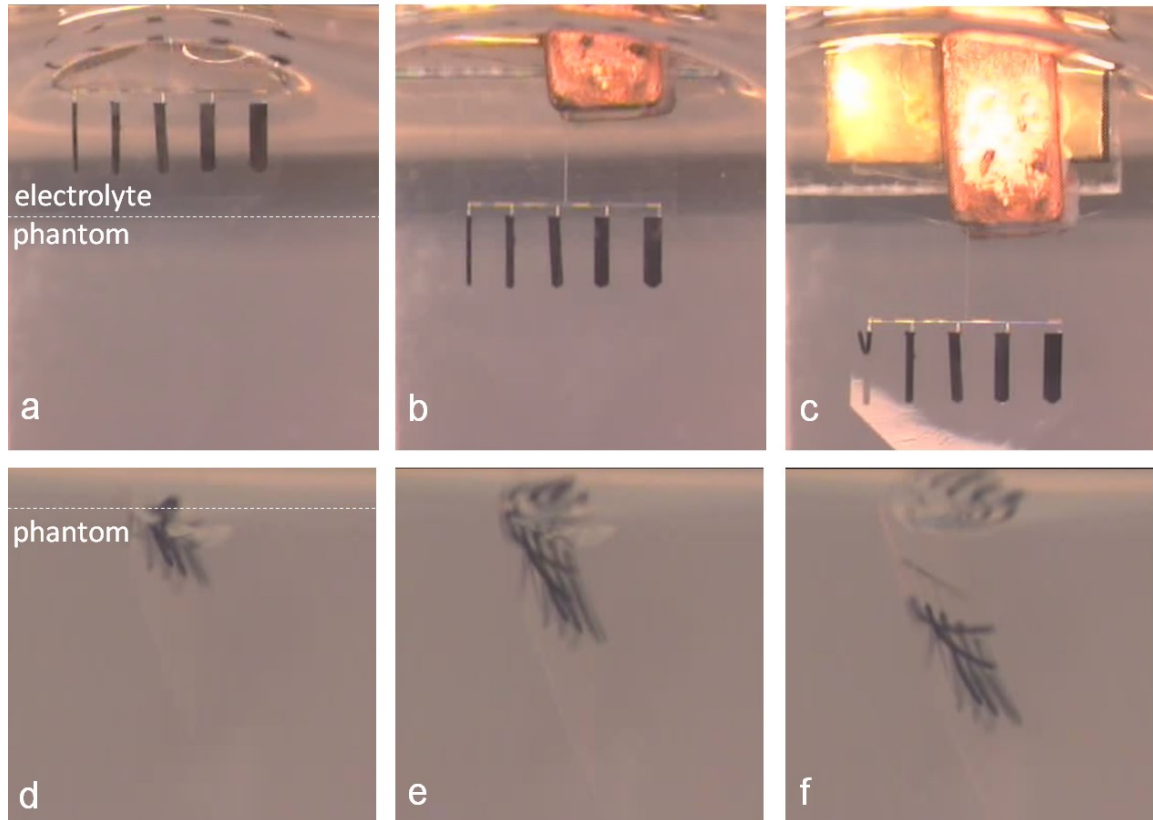


Figure 4-8. Screenshots of devices with five electrode projections of varying widths (50, 100, 150, 200, and 250 μm) and lengths (top row 1000 μm , bottom row 800 μm) penetrating a brain tissue phantom made of 0.6% agarose and 0.1 M NaDBS. Images in the top row show devices (a) outside the phantom, (b) inserted in a reduced state (straight), and (c) inserted in an oxidized state (bent). Images in the bottom row show actuation during insertion (d-f). The estimated (compensated for viewing angle) tip deflections out of plane for the 800 μm long beams with widths of 50 μm and 100 μm were $\sim 772 \mu\text{m}$ and $\sim 474 \mu\text{m}$, respectively.

4.4 Discussion and conclusions

As previously mentioned, there are multiple factors that can influence neural probe insertion and the resulting immune response surrounding the base substrate. This work demonstrates that conjugated polymer actuators may be used to steer the neural electrode projections in the brain as a way to deploy electrode sites away from the probe. In this work, an electrode projection 50 μm wide was able to deflect almost 800 μm away.

Given that immune response encapsulation of typical neural probes of 100 – 200 μm width occurs within 50 – 100 μm of the probe [2, 34], this approach may be feasible to place electrode sites in more favorable recording environments.

Further analysis is necessary to explain the relationship between the tip geometry and ability to penetrate the phantom. The tip cross-sectional area at the end of the beam that cuts into the tissue has been shown to have significant influence on the opposing forces. The insertion results in this study suggest that there may possibly be a tip aspect ratio factor resulting in non-linear cutting forces that limit tissue penetration, favoring smaller dimensions.

Table 4-1 lists the projection tip cross-sectional area and width to thickness aspect ratios for the devices used in this study. Since all projections had a 45° opening angle, the tip surface area and aspect ratios increase linearly. However, tip aspect ratios and opening angles can be designed to minimize insertion forces for projection deployment.

Table 4-1. Projection tip aspect ratios

Beam Width (μm)	Tip Area (μm^2)	Cross-sectional Aspect Ratio (width/thickness)
50 (1x)	1768 (1x)	2
100 (2x)	3536 (2x)	4
150 (3x)	5303 (3x)	6
200 (4x)	7071 (4x)	8
250 (5x)	8839 (5x)	10

In addition to cortical neural probes, similar articulating electrode arrays can potentially be used in other neural interface applications. Figure 4-9 shows images of an array of electrode projections that could be used in applications such as retinal electrodes to restore vision, cochlear electrodes to restore hearing, ECoG arrays to monitor brain-

surface electrophysiology, and peripheral nerve interfaces aimed to control advanced prostheses. These applications may not require insertion into tissue and would benefit from the electrode projections described here.

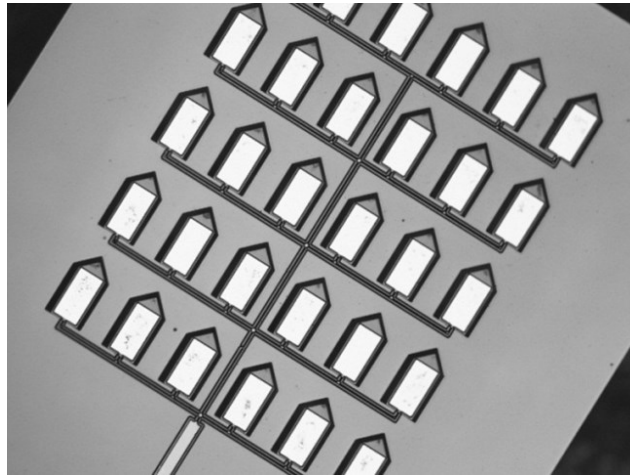


Figure 4-9. Electrode grid proof of concept shown as an array of uncoated electrode projections.

4.5 References

- [1] D. R. Kipke, G. J. Gage, E. K. Purcell, J. P. Seymour, J. Subbaroyan, and T. C. Marzullo, "Development of neural interfaces for chronic use in neuromotor prosthetics," *2007 Ieee 10th International Conference on Rehabilitation Robotics, Vols 1 and 2*, 1026-1030 1135, 2007.
- [2] V. S. Polikov, P. A. Tresco, and W. M. Reichert, "Response of brain tissue to chronically implanted neural electrodes," *J. Neurosci. Methods*, 148, 1-18, 2005.
- [3] J. P. Seymour and D. R. Kipke, "Neural probe design for reduced tissue encapsulation in CNS," *Biomaterials*, 28, 3594-3607, 2007.
- [4] D. Egert and K. Najafi, "New class of chronic recording multichannel neural probes with post-implant self-deployed satellite recording sites," *IEEE Transducers*, Beijing, China, 958-961, edited by Anonymous (June 5-9, 2011).
- [5] E. Smela, "Conjugated polymer actuators for biomedical applications," *Adv. Mater.*, 15, 481-494, 2003.
- [6] C. E. Schmidt, V. R. Shastri, J. P. Vacanti, and R. Langer, "Stimulation of neurite outgrowth using an electrically conducting polymer," *Proc. Natl. Acad. Sci.*, 94, 8948-8953, 1997.
- [7] R. L. Williams and P. J. Doherty, "A preliminary assessment of poly(pyrrole) in nerve guide studies," *J. Mater. Sci. Mater. Med.*, 5, 429-433, 1994.
- [8] X. D. Wang, X. S. Gu, C. W. Yuan, S. J. Chen, P. Y. Zhang, T. Y. Zhang, J. Yao, F. Chen, and G. Chen, "Evaluation of biocompatibility of polypyrrole in vitro and in vivo," *J. Biomed. Mater. Res. A*, 68A, 411-422, 2004.
- [9] J. P. Seymour and D. R. Kipke, "Fabrication of polymer neural probes with Sub-cellular features for reduced tissue encapsulation," *Conf. Proc. IEEE Eng. Med. Biol. Soc.*, New York, vol. 1, (August 30-September 3, 2006).
- [10] A. M. Okamura, C. Simone, and M. D. O'Leary, "Force modeling for needle insertion into soft tissue," *IEEE T. Bio. Med. Eng.*, 51, 1707-1716, 2004.
- [11] A. A. Sharp, A. M. Ortega, D. Restrepo, D. Curran-Everett, and K. Gall, "In vivo penetration mechanics and mechanical properties of mouse brain tissue at micrometer scales," *IEEE T. Bio. Med. Eng.*, 56, 45-53, 2009.
- [12] W. Jensen, K. Yoshida, and U. G. Hofmann, "In-vivo implant mechanics of flexible, silicon-based ACREO microelectrode arrays in rat cerebral cortex," *IEEE T. Bio. Med. Eng.*, 53, 934-940, 2006.

- [13] C. S. Bjornsson, S. J. Oh, Y. A. Al-Kofahi, Y. J. Lim, K. L. Smith, J. N. Turner, S. De, B. Roysam, W. Shain, and S. J. Kim, "Effects of insertion conditions on tissue strain and vascular damage during neuroprosthetic device insertion," *Journal of Neural Engineering*, 3, 196-207, 2006.
- [14] R. L. Rennaker, S. Street, A. M. Ruyle, and A. M. Sloan, "A comparison of chronic multi-channel cortical implantation techniques: manual versus mechanical insertion," *J. Neurosci. Methods*, 142, 169-176, 2005.
- [15] K. Najafi and J. F. Hetke, "Strength characterization of silicon microprobes in neurophysiological tissues," *IEEE Trans. Biomed. Eng.*, 37, 474-481, 1990.
- [16] K. J. Paralikar and R. S. Clement, "Collagenase-aided intracortical microelectrode array insertion: Effects on insertion force and recording performance," *IEEE T. Bio. Med. Eng.*, 55, 2258-2267, 2008.
- [17] B. A. Wester, R. H. Lee, and M. C. LaPlaca, "Development and characterization of in vivo flexible electrodes compatible with large tissue displacements," *Journal of Neural Engineering*, 6, 2009.
- [18] B. Shapiro and E. Smela, "Bending actuators with maximum curvature and force and zero interfacial stress," *J. Intel. Mat. Syst. Str.*, 18, 181-186, 2007.
- [19] Changlin Pang, , "*Parylene Technology for Neural Probes Applications*," California Institute of Technology, 2008.
- [20] R. R. Richardson, J. A. Miller, and W. M. Reichert, "Polyimides as Biomaterials - Preliminary Biocompatibility Testing," *Biomaterials*, 14, 627-635, 1993.
- [21] e. a. Hong-seok Noh, "Wafer bonding using microwave heating of parylene intermediate layers," *J. Micromech. Microengineering*, 14, 625, 2004.
- [22] E. Smela, "Microfabrication of PPy microactuators and other conjugated polymer devices," *J. Micromech. Microeng.*, 9, 1-18, 1999.
- [23] X. Z. Wang, E. Smela, and B. Shapiro, "Understanding ion transport in conjugated polymers," *Proc. SPIE Smart Struct. Mater. (EAPAD)*, San Diego, CA, vol. 5385, 146-154, edited by Y. BarCohen (Mar 15-18, 2004).
- [24] G. Wallace, G. Spinks, L. Kane-Maguire and P. Teasdale, Conductive Electroactive Polymers
Intelligent Polymer Systems, 3rd ed. (CRC Press, Boca Raton, Fl, 2009).
- [25] F. Pervin and W. Chen, "Mechanically Similar Gel Simulants for Brain Tissues," Indianapolis, Indiana USA, edited by Anonymous ().

- [26] Z. J. Chen, G. T. Gillies, W. C. Broaddus, S. S. Prabhu, H. Fillmore, R. M. Mitchell, F. D. Corwin, and P. P. Fatouros, "A realistic brain tissue phantom for intraparenchymal infusion studies," *J. Neurosurg.*, 101, 314-322, 2004.
- [27] E. D. Daneshvar, E. Smela, and D. R. Kipke, "Mechanical characterization of conducting polymer actuated neural probes under physiological settings," *Proc. SPIE Smart Struct. Mater. (EAPAD)*, San Diego, vol. 7642, 1T.1-1T.10, edited by Y. Bar-Cohen (March 7-11, 2010).
- [28] M. Christophersen, B. Shapiro, and E. Smela, "Characterization and modeling of PPy bilayer microactuators - Part 1. Curvature," *Sens. Act. B*, 115, 596-609, 2006.
- [29] S. F. Cogan, "Neural stimulation and recording electrodes," *Annu. Rev. Biomed. Eng.*, 10, 275-309, 2008.
- [30] M. A. Moffitt and C. C. McIntyre, "Model-based analysis of cortical recording with silicon microelectrodes," *Clinical Neurophysiology*, 116, 2240-2250, 2005.
- [31] M. P. Hughes, K. Bustamante, D. J. Banks and D. J. Ewins, Effects of electrode size on the performance of neural recording microelectrodes(2000).
- [32] S. Suner, M. R. Fellows, C. Vargas-Irwin, G. K. Nakata, and J. P. Donoghue, "Reliability of signals from a chronically implanted, silicon-based electrode array in non-human primate primary motor cortex," *Ieee Transactions on Neural Systems and Rehabilitation Engineering*, 13, 524-541, 2005.
- [33] X. Cui, J. F. Hetke, J. A. Wiler, D. J. Anderson, and D. C. Martin, "Electrochemical deposition and characterization of conducting polymer polypyrrole/PSS on multichannel neural probes," *Sensors and Actuators A: Physical*, 93, 8-18, 2001.
- [34] R. Biran, D. C. Martin, and P. A. Tresco, "Neuronal cell loss accompanies the brain tissue response to chronically implanted silicon microelectrode arrays," *Exp. Neurol.*, 195, 115-126, 2005.

CHAPTER 5 Conclusions, contributions, and future directions

5.1 Conclusions

In summary, this research work explored the feasibility of using electroactive polymer actuators to articulate neural interface devices. The capability of PPy(DBS) to operate under physiological conditions was assessed. The significance of the residual stress that is generated with the substrate as a result of actuating PPy(DBS) was distinguished. A new tool and method was developed to measure micro-scaled force generation from bilayer actuators. Lastly, integration of a conjugated polymer actuator on a neural probe was done and controlled movement of its electrode sites out-of-plane was successfully demonstrated in solution and in a brain phantom. This work demonstrated that conjugated polymer actuators may enable controlled movement of neural probes and electrode interfaces out-of-plane not possible before.

5.2 List of contributions

Below is the list of intellectual contributions that resulted from this thesis work. In addition, contributions to a significant project developing a novel peripheral nerve interface are also highlighted in the appendix.

5.2.1 Characterization of PPy(DBS) actuation performance under cerebral physiological conditions

In this thesis, characterization of the actuation strain of electroactive polymer PPy(DBS) in artificial cerebrospinal fluid and at physiological temperature was done. Results show

that under physiological conditions the actuation strain was monotonic and performance is substantially the same as the control conditions; demonstrating that these actuators may be used at elevated temperatures and in mixed ionic aqueous environments such as cerebrospinal fluid. This work is described in a journal publication in *Advanced Healthcare Materials* [1].

5.2.2 Development of a MEMS tip-weighted conjugated polymer bilayer actuator test device

The concept and development of a MEMS tip-loaded conjugated polymer bilayer actuator device for measuring actuation force and residual strain is introduced and demonstrated. A corresponding model was developed combining the forces and moments acting on the device. The design space and relationship of device dimensions to meaningful data was identified. A custom fabrication plan for making bilayer beams with electroplated end weights was developed and used. The device was experimentally validated and measurements of actuation forces resulting from PPy(DBS) was shown.

A novel method to calculate the conjugated polymer's Young's moduli and actuation strain was demonstrated using two devices with differential dimensions. Limited samples were successfully tested, however, one experimental value matched exactly that of previous reported results for oxidized PPy(DBS) Young's moduli. The device is partially described in a conference proceeding from the 2010 SPIE Electroactive Polymer Actuators and Devices (EAPAD) conference [2].

5.2.3 Proof of concept of functional articulating neural probes and electrodes demonstrated

The concept of moveable (to steer or guide) neural probes, neural electrodes, and neural interfaces was introduced. Specific benefits for different neural interfacing applications, and both neural recording and stimulating devices was theorized. Specific to the application of micro-sized thin film cortical electrodes, modeling of the opposing forces required to bend thin-film electrode projections and prevent buckling from insertion into brain tissue was done. Multiple fabrication methods for functional neural electrodes with conjugated polymer actuating segments were derived and several iterations were tested. A proof-of-concept was shown, demonstrating that electrode projections could be controllably held either remain flat or to actuate out-of-plane during insertion into a brain phantom. Electrode projections, having electrode sites at their tip, that were originally inplane with the neural probe substrate, were moved laterally hundreds of microns as a result of the residual stress between the polymer and substrate layers. The device is described in a conference proceeding from the 2012 SPIE Electroactive Polymer Actuators and Devices (EAPAD) conference [3].

5.2.4 Journal papers

- E. D. Daneshvar and E. Smela, "Characterization of conjugated polymer actuation under cerebral physiological conditions," *Adv. Healthcare Mater.*, 2014 (Accepted).
- M. R. Abidian, E. D. Daneshvar, B. M. Egeland, D. R. Kipke, P. S. Cederna, and M. G. Urbanchek, "Hybrid conducting polymer–hydrogel conduits for axonal growth and neural tissue engineering," *Adv. Healthcare Mater.*, 1, 762-767, 2012.

5.2.5 Conference papers

- E. D. Daneshvar, E. Smela, and D. R. Kipke, "Mechanical characterization of conducting polymer actuated neural probes under physiological settings," Proc. SPIE Smart Struct. Mater. (EAPAD), San Diego, vol. 7642, 1T.1-1T.10, edited by Y. Bar-Cohen (March 7-11, 2010).
- E. D. Daneshvar, D. R. Kipke, and E. Smela, "Navigating conjugated polymer actuated neural probes in a brain phantom," Proc. SPIE Smart Struct. Mater. (EAPAD), San Diego, vol. 8340, 09.1-09.12, edited by Y. Bar-Cohen (March 12-15, 2012).

5.2.6 Oral presentations

- Title: "Electroactive polymer actuators for medical applications," IDTechEx Printed Electronics Europe Conference, Berlin, Germany, April 18th, 2013. (Invited talk)
- Title: "Navigating conjugated polymer actuated neural probes in a brain phantom," SPIE Smart Structures and Materials: Electroactive Polymer Actuators and Devices Conference, San Diego, March 13th, 2012.
- Title: "Mechanical characterization of conducting polymer actuated neural probes under physiological settings," SPIE Smart Structures and Materials: Electroactive Polymer Actuators and Devices Conference, San Diego, March 11th, 2010.

5.2.7 Conference posters

- E. D. Daneshvar, A. Raof, "Demonstration of neural probes in plastinated brain sections as educational tools," 40th Neural Interfaces Conference, Salt Lake City, June 18-20, 2012.
- E. D. Daneshvar, E. Smela, D. R. Kipke, "Articulated neural interface devices using conjugated polymer actuators," Society for Neuroscience, Washington D.C., November 12-16, 2011.
- E. D. Daneshvar, E. Smela, D. R. Kipke, "Conducting polymer neural electrode projections," 39th Neural Interfaces Conference, presented by the National Institute of Neurological Disorders and Stroke, Long Beach, June 21-23, 2010.
- E. D. Daneshvar, M. R. Abidian, E. Smela, D. R. Kipke, "Conducting polymer actuated neural pivot probe," Material Research Society, Symposium NN: Active Polymers, San Francisco, April 13-17, 2009.
- E. D. Daneshvar, M. R. Abidian, D. R. Kipke, "Conducting polymer microvalves for neural microelectrodes," Biomedical Engineering Society Annual Meeting, St. Louis, October 1-4, 2008.

5.3 Future directions

5.3.1 Further characterization of actuation performance

Initial experiments on characterizing actuation speed were included in the supplemental section of Chapter 2. A greater number of replicate samples would be needed to validate the trend in the initial experiments. New device designs to improve data collection are mentioned below.

Initial experiments on characterizing actuation force were included in Chapter 3. A greater number of replicate samples would be needed to validate the results in the initial experiments. New device designs to improve data collection are mentioned below.

5.3.2 Alternate device designs for measuring actuation performance

Electronic readout using embedded strain sensors

An improvement to the devices described in Chapters 2 and 3, used to measure CP actuation performance, would be to include electronic readout of bending opposed to the optical detection method in this work. Prototypes of this method using thin-film strain sensors were designed, fabricated, and initial tests were done validating the concept. Figure 5-1 shows such a device being manually moved and the electronic readout results are shown in Figure 5-2.

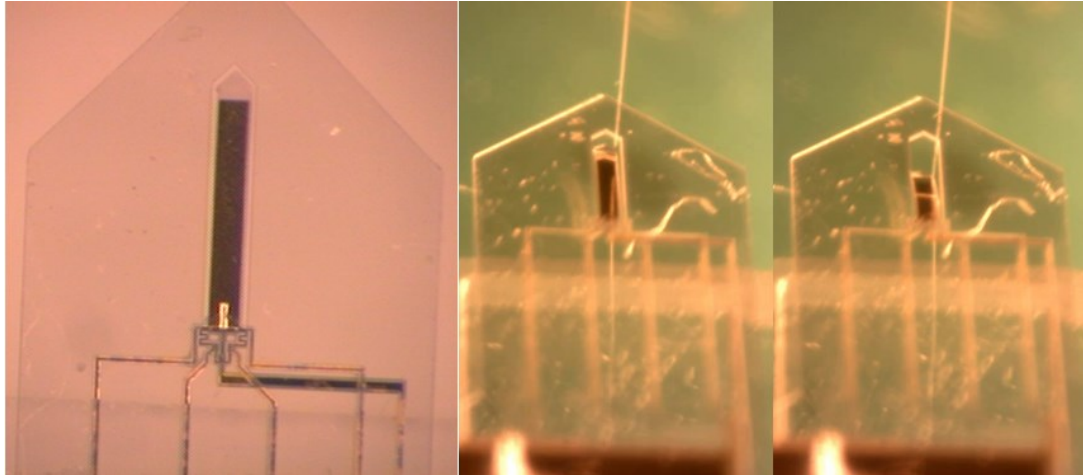


Figure 5-1. (Left) Fabricated bilayer beam with embedded strain sensor and Wheatstone bridge. (Middle) Beam prior to displacement. (Right) Beam after manual displacement by a needle and computer-controlled linear actuator.

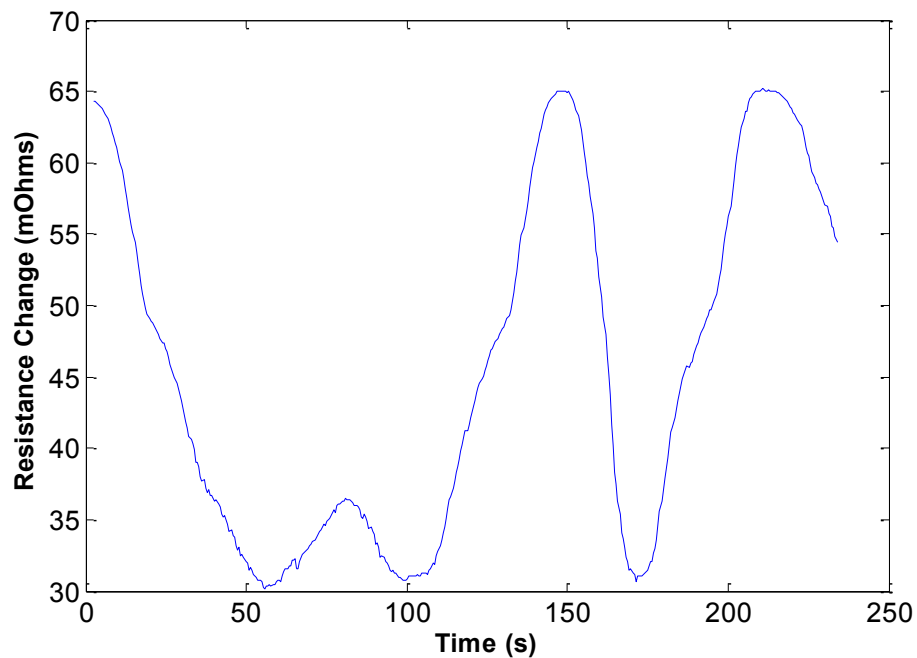


Figure 5-2. Change in resistance vs time from manually displacing bilayer beam with integrated thin film metal strain sensor.

MEMS bridge to replace weights or wider substrate width

Two alternate designs to improve the MEMS weighted bilayer device are proposed.

First, the weight in the weighted beam design could be replaced with a bridge connection

to oppose deflection. Second, the substrate stiffness could be increased simply by making the width of only the substrate wider.

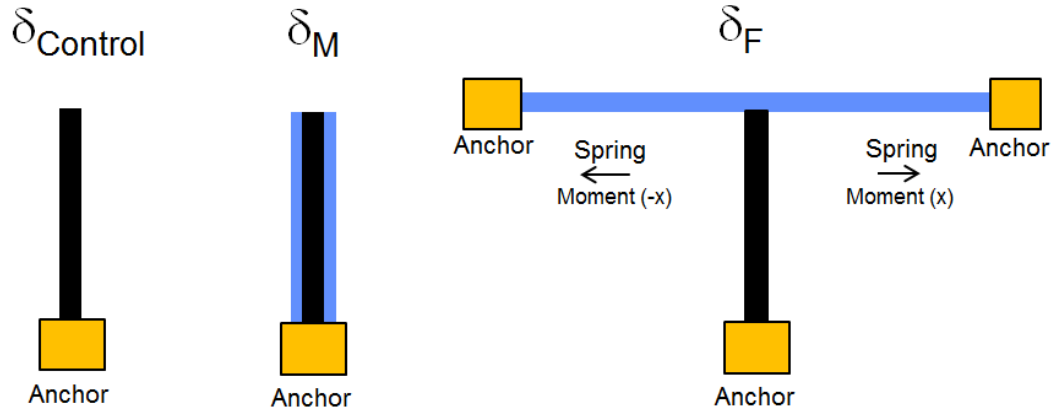


Figure 5-3. Top view of the composite beam either as a control (Left), with a wider substrate (Middle), or tethered to a bridge acting as a mechanical spring (Right).

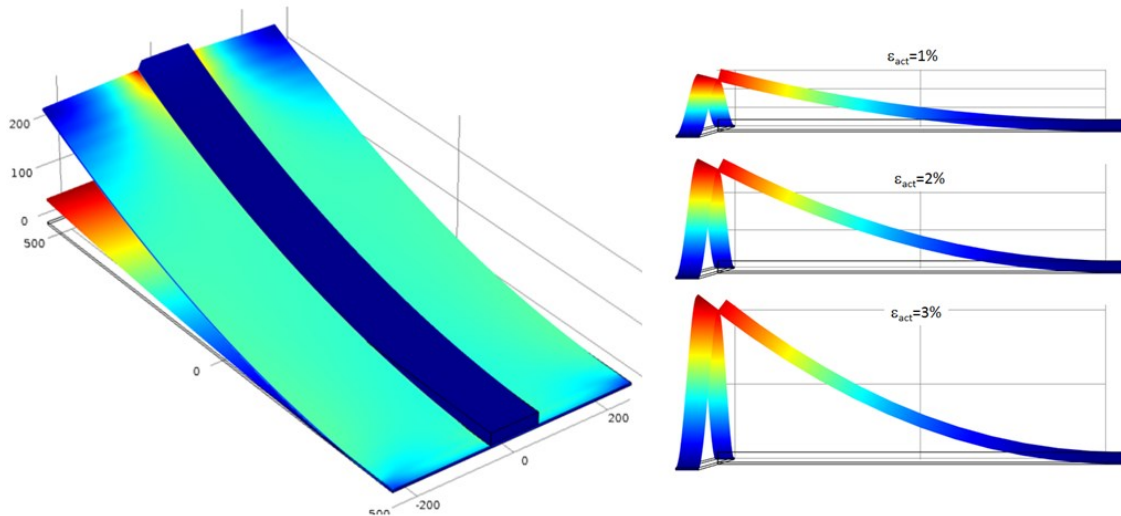


Figure 5-4. (Left) Comsol rendering of a bilayer beam with a wider substrate. (Right) Comsol rendering showing T-Bridge tip displacement vs actuation strain for a bridge length of 5000 μm .

Embedded strain sensors can readily be integrated into these designs for electrical sensing of deflection. This design would enable high-throughput testing, which has many advantages.

5.3.3 Application specific design of movable neural interfaces

Each specific application of a neural interface will have its own set of unique requirements and limitations. Applications for inserting into tissue must account for stiffness considerations of penetrating the tissue, whereas those that are surface mounted or operating in aqueous environments do not. Electrode projections inserted into tissue may likely bend greater as a result of opposing normal forces due to the tissue. This can possibly be exploited to achieve greater deflections with less polymer actuation strain. However, possible damage to the tissue should not be overlooked.

5.3.4 Projections with variable thickness and segmented joints

The bending of electrode projections may be varied several ways. Two concepts were initially explored. First, projections with larger polymer to substrate ratios (by having smaller substrate thickness) resulted in smaller radii of curvature, as shown by greater bending in Figure 5-5. Devices with projections having a variable number and coverage of segmented joints were fabricated but not tested. Although they are all electrically connected, in future designs, these segments may be individually controlled for more complex movements.

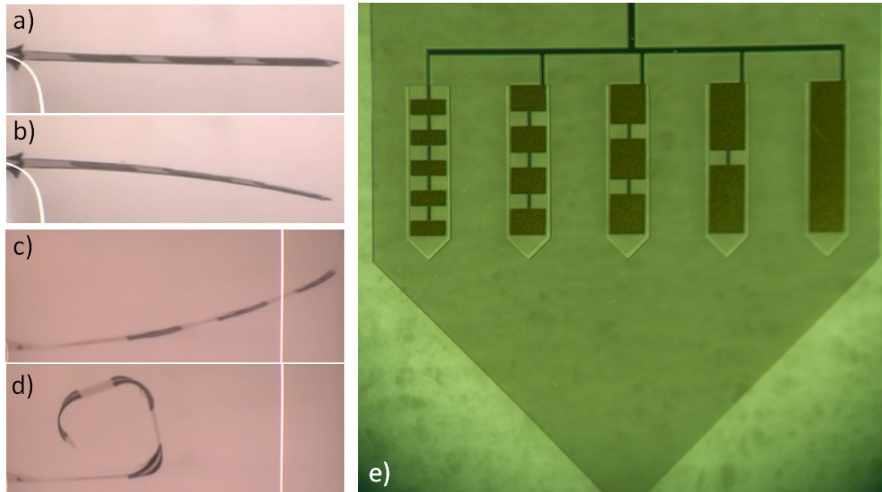


Figure 5-5. Variable segmented devices: (a-b,-c-d) effect of differing thickness ratios for the joints and (e) a device with variable number of segmented joints along the projection.

5.3.5 Alternate projection geometries

There are multiple variations of electrode projection designs. Two variations that would be useful to explore are the effect of tip shape on cutting forces during insertion into tissue, as well as the projection shape as shown in Figure 5-6. As a result of the projections bending out-of-plane, the two designs in Figure 5-6 will result in different 3D spatial distributions.

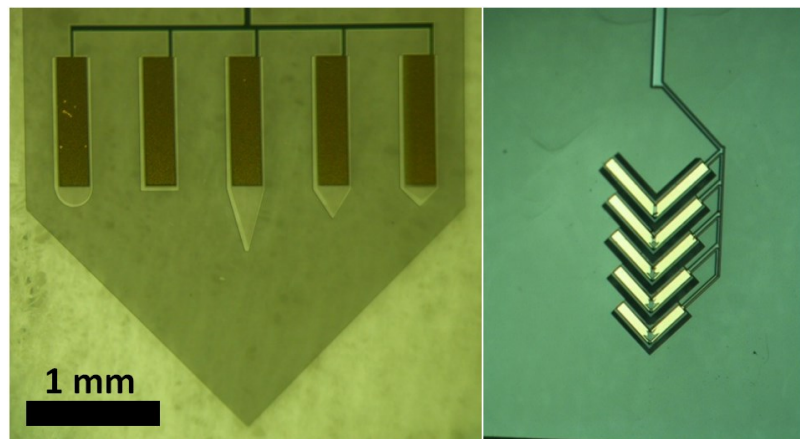


Figure 5-6. Alternate projection geometries: (Left) tip shape, (Right) projection shape.

5.3.6 Other uses of movable projections

MEMS devices are known for their small size and are increasingly being used for biomedical applications. Recently, one such device is in development to monitor ocular pressure in the eye for glaucoma patients [5]. Unfortunately, the benefit of the small size of such devices is also a technical limitation of implanting and securing it to the tissue in the eye. Currently, large appendages are incorporated in the design in order to provide the ophthalmologist a way to suture the device in place. An array of articulating electrodes may serve as “Electronic Velcro” which may secure the device to the eye without needing sutures.

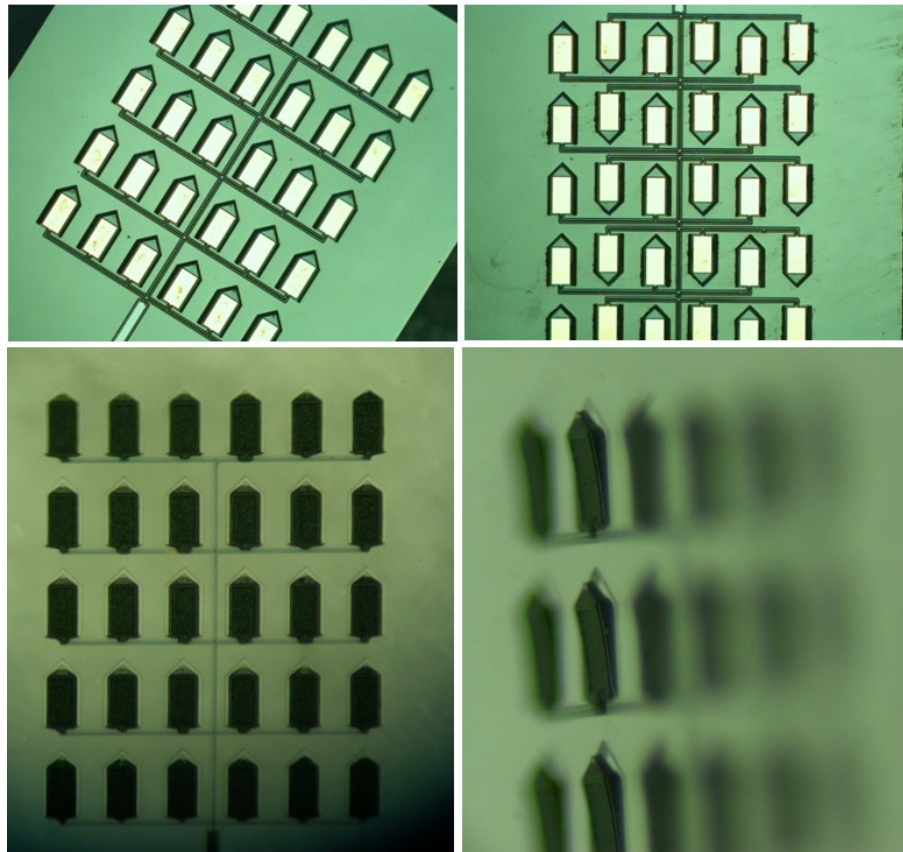


Figure 5-7. Proof of concept for the grid array applications as well as the electronic velcro idea. Array of 5x6 projections 100 μm wide, 200 μm long, PPy(DBS) \sim 20 μm , Parylene \sim 10 μm for the projections, and \sim 35 μm for the substrate.

5.4 Final thoughts

In summary, this thesis introduced several novel concepts that may be beneficial to the neural engineering and neural interfaces fields. Neural interfaces have distinct and critical challenges to overcome in each application. Where movable neural probes, electrode projections, and electrode sites may be advantageous, this work demonstrates a viable solution with minimal changes to their fabrication processes.

The use of conjugated polymer actuators was pursued because of their unique advantages over other currently available actuation modalities. Their complex inextricably linked electrical, chemical, and mechanical properties may make their adoption initially intimidating. However, this complexity is also their greatest advantage; whereby the same material can be customized for actuation, mechanical or chemical sensing, drug delivery, and signal propagation. Elegant solutions are only waiting to be discovered. With use of MEMS technology, high-throughput testbeds and tools can readily be made to simplify, automate, and accelerate their characterization and optimization.

5.5 References

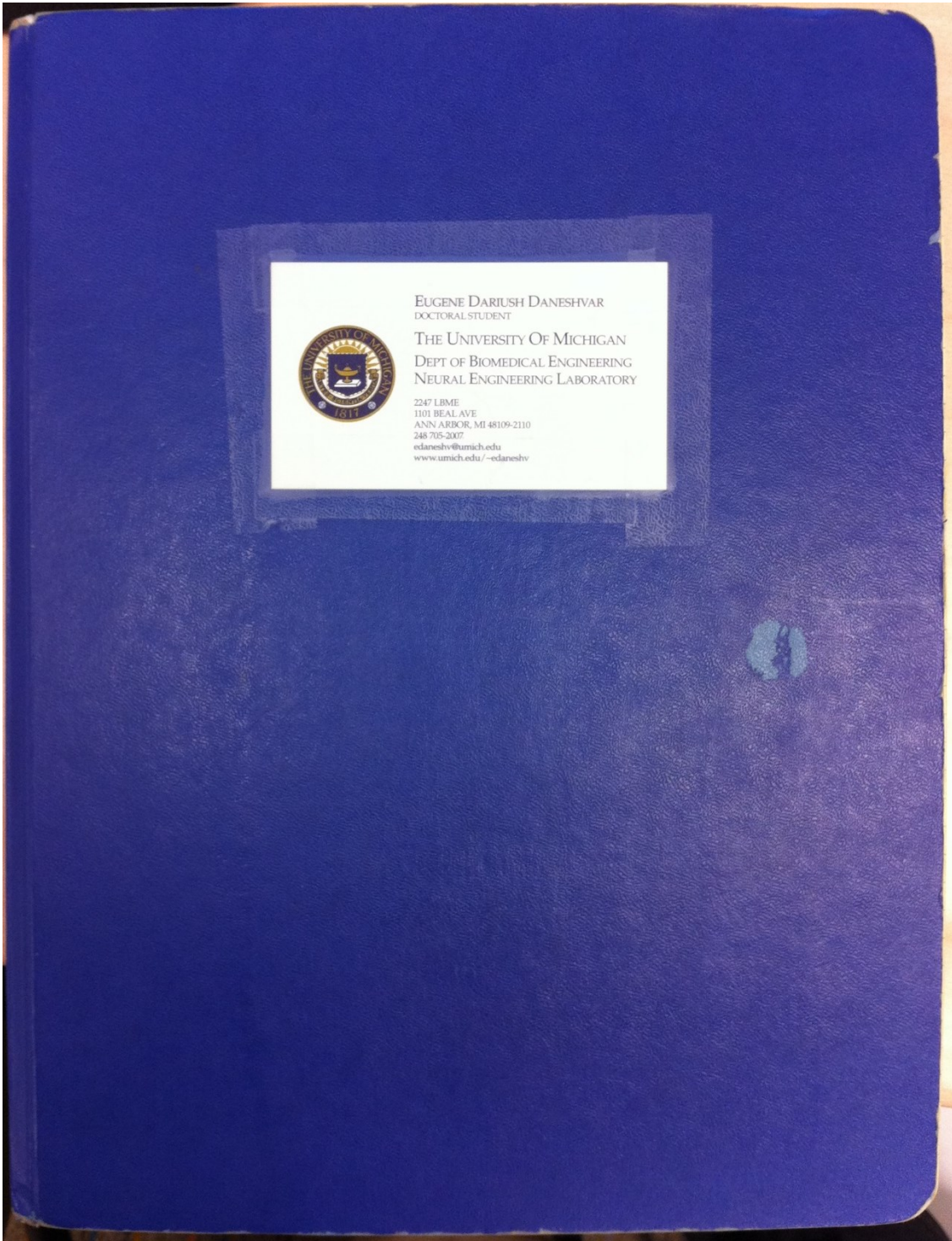
- [1] E. D. Daneshvar and E. Smela, "Characterization of conjugated polymer actuation under cerebral physiological conditions (Accepted)," *Adv. Healthcare Mater.*, 2014.
- [2] E. D. Daneshvar, E. Smela, and D. R. Kipke, "Mechanical characterization of conducting polymer actuated neural probes under physiological settings," *Proc. SPIE Smart Struct. Mater. (EAPAD)*, San Diego, vol. 7642, 1T.1-1T.10, edited by Y. Bar-Cohen (March 7-11, 2010).
- [3] E. D. Daneshvar, D. R. Kipke, and E. Smela, "Navigating conjugated polymer actuated neural probes in a brain phantom," *Proc. SPIE Smart Struct. Mater. (EAPAD)*, San Diego, vol. 8340, 09.1-09.12, edited by Y. Bar-Cohen (March 12-15, 2012).
- [4] M. R. Abidian, E. D. Daneshvar, B. M. Egeland, D. R. Kipke, P. S. Cederna, and M. G. Urbanchek, "Hybrid conducting polymer–hydrogel conduits for axonal growth and neural tissue engineering," *Adv. Healthcare Mater.*, 1, 762-767, 2012.
- [5] R. M. Haque and K. D. Wise, "An intraocular pressure sensor based on a glass reflow process," *Solid-State Sensors, Actuators, and Microsystems Workshop*, Hilton Head Island, South Carolina, 49-52, edited by Anonymous (June 6-10, 2010).

Appendix

A1. Hybrid Conducting Polymer–Hydrogel Conduits for Axonal Growth and Neural Tissue Engineering

Significant contributions were also made to another research project using conjugated polymers for peripheral nerve conduits. The concept of enhancing a hydrogel-based peripheral nerve interface by incorporating a varying layer of conjugated polymer along its length and connected by stents was introduced and tested. The stents were added to the conduit ends to provide mechanical rigidity and allow the surgeon to suture the device securely. In addition, the stent could be collapsed to accommodate unique sized tissues and provide additional mechanical support side from the sutures. Conduits were tested a three month chronic study using a rat model. Weekly walk tests were conducted to assess the progress of the functional recovery of their hind limbs. This work is described in a journal publication in *Advanced Healthcare Materials* 1, 762-767, 2012, titled "Hybrid conducting polymer–hydrogel conduits for axonal growth and neural tissue engineering," with authors M. R. Abidian, E. D. Daneshvar, B. M. Egeland, D. R. Kipke, P. S. Cederna, and M. G. Urbanchek.

A2. Lab notebook excerpts recording the movable probe and electrode concepts



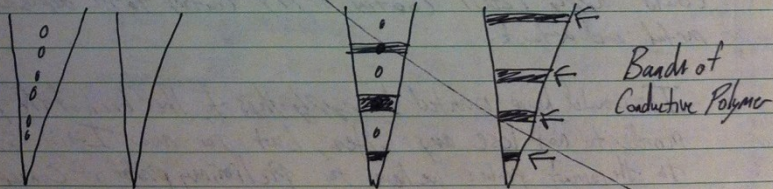
6/13/07

Novel Idea

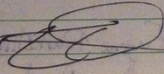
This novel idea of incorporating conductive polymers onto neural probes, both rigid-like silicon substrates and flexible polymer substrates, for movement guidance and manipulation has occurred to me. I have not seen any application such as this before. I have seen applications of conductive polymers being used to bend substrates such as in 'micro muscles' work. I wish to apply this technology to neural probes in order to manipulate the placement of the probes in-vivo.

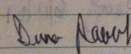
Once the surgeon has implanted the probe he/she does not have control of where the probe's final resting place is or its' proximity to neurons surrounding it. Also, in the quest for determining whether neurons 're-wire' themselves or surrounding neurons die etc., this idea would be very helpful in that once the units disappear after ~ 6 weeks, we could actuate the probes position and move it around to search for the next active set of neurons. Even if we cause damage by moving the probe, just determining if it is the neuronal necrosis around the probe or not is significant to finding out what causes loss of signal.

Preliminary Design:



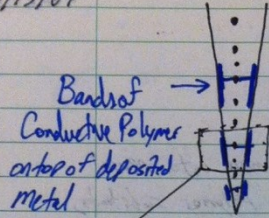
Regular Front & Back

Invented by: Eugene Daneshvar  6/13/07

Witnessed by: DUNA RAOF  6/13/07

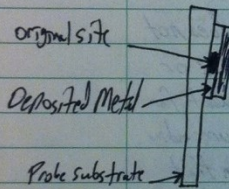
ED
6/13/07

6/13/07



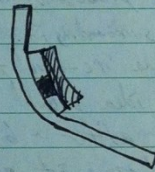
The basic design is to deposit a metal such as Au or other metals shown to work with conductive polymer actuation then coat them with the respective conductive polymer. The line shown through the electrode site is either a layer on top of the probe or a trace incorporated in the design of the probe.

The idea is that when that site is stimulated it would cause the conductive polymer to excite and bond the probe at that location. Having more than one of these bands would allow more degrees of freedom.



Side View
Regular

← Conductive Polymer coated on deposited Metal.



Side View
Actuated

← This may be exaggerated especially since we have to be careful NOT to overstress the Probe Substrate.

This is shown for one band across one site

I believe to achieve this effect we could use an ordinary probe (Current Probes from New Mexico) and develop a preliminary mask to selectively sputter metal on top. Then we could apply PEDOT coating or PPY coating to the deposited metal and actuate.

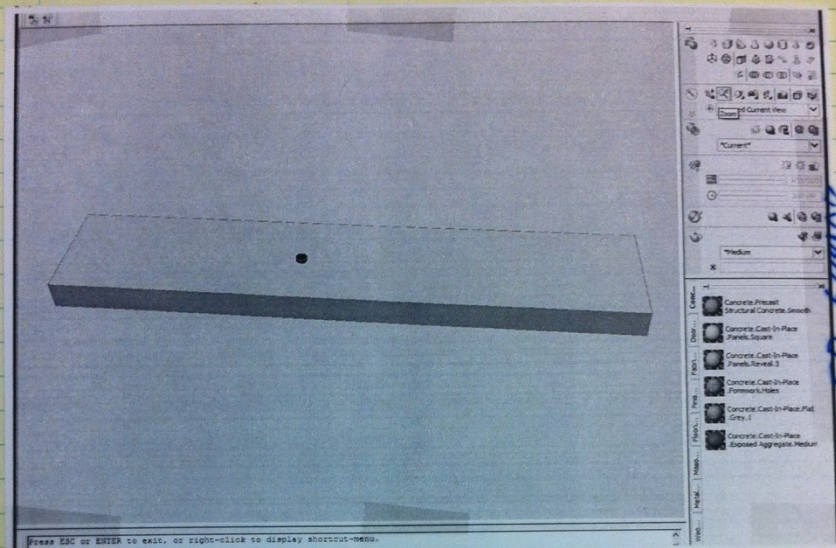
I would have wanted to apply this to the back of the probe in order to not lose any sites, but for now I will stick to the current probes we have for preliminary proof of concept.

ED
6/13/07

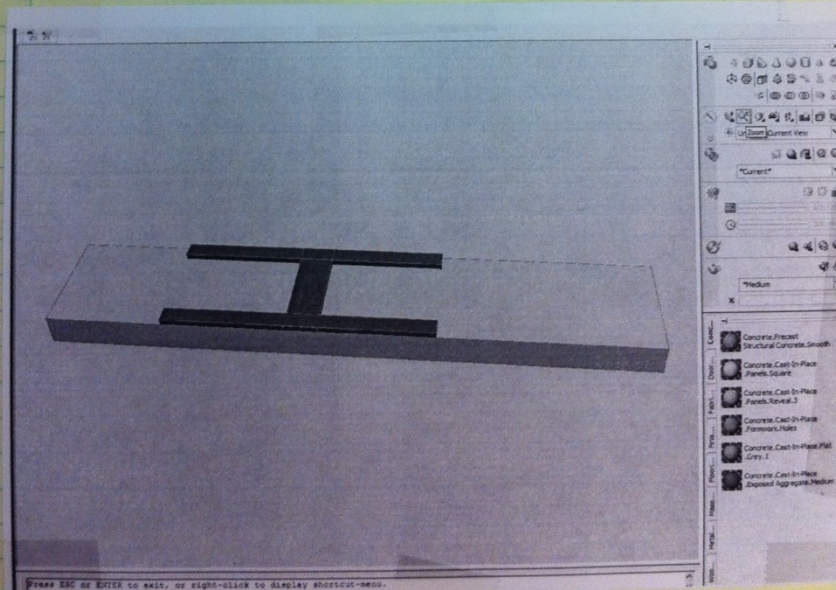
Invented by: Eugene Daneshvar 6/13/07
Witnessed by: Susan Ruff 6/13/07

6/14/07

This figure is meant to resemble a close up view of one site on a current probe.

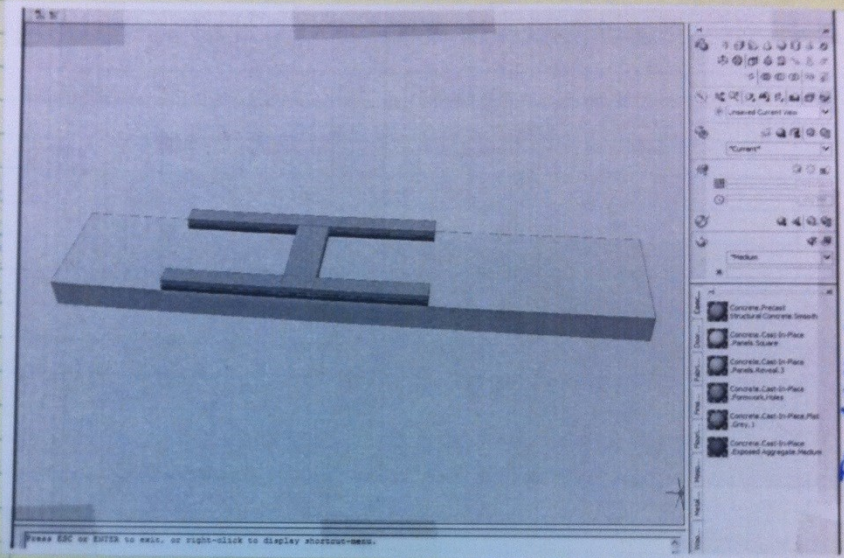


This figure below is showing proposed layout of sputtered metal covering electrode site.



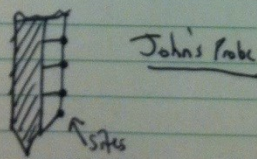
6/14/07

This figure shows Conductive Polymer grown on top of the metal.

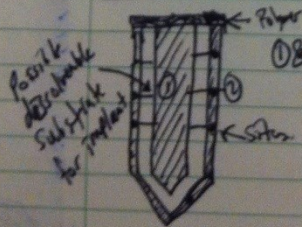


Another design:

With inspiration from John Seymour's Probe design which incorporates a wider shank with electrode sites away from the main shank:



I propose a similar type of probe that can actually split apart after insertion. The Probe must have separation already done before implant so that it can just bend away once implanted.



① & ② are separate and can split once implanted.

ED 6/14/07

DO NOT WRITE

Subject: P3: Pivot Probe Project?
From: "Eugene Dariush Daneshvar" <edaneshv@umich.edu>
Date: 6/21/2007 9:53 PM
To: <dkipke@umich.edu>

Dear Prof. Kipke,

Thank you for having the patience and giving me the opportunity to show results. I think that the idea I presented to you today will have tremendous applications to our field. I would like to develop this idea as a start toward my PhD work.

I foresee this technology to bend, guide, and extend probes in vivo to help determine what happens after chronic neuronal signal loss. We could also use it to design a new probe that sends out its recording sites away from the shank similar to John's idea. Clearly there are many more applications such as bypassing vasculature, targeting specific layers (horizontally), incorporation into your DBMA and Medtronic's stimulating electrode, etc.

At the moment I am conducting experiments with different conducting polymers to learn more about what we have to work with. I'll keep you updated.

Sincerely,

-Eugene

PS. All we need now is a catchy name to go with the idea.